TAILORING OLIGO AND POLYTHIOPHENES FOR INTERFACE OPTIMIZATION IN HYBRID SOLAR CELLS

PhD Thesis in Materials Engineering of Teresa Gatti

XXVI Cycle

Department of Chemistry, Materials and Chemical Engineering "Giulio Natta"

Supervisor: Prof. Chiara Bertarelli

Co-supervisor: Dr. Ing. Eleonora Valeria Canesi

Tutor: Prof. Chiara Castiglioni

PhD Coordinator: Prof. Chiara Castiglioni

1

Preface to this thesis

The PhD research activity described in this thesis has focused principally on the development of thiophene-based materials for third generation, hybrid organic-inorganic photovoltaic cells. For this reason, the title and Part One, including Chapters 1, 2, 3 and 4, are entirely related to the subject. The use of these organic scaffolds in solid state hybrid devices has been tested and some useful guidelines for the future development of more effective materials have been traced.

As a side project, roughly unrelated to the leading theme of the PhD, the photoluminescence properties of phenyl end-capped oligothiophenes were evaluated with regard to the solid-state organization. This study is reported in Part Two of the present manuscript (Chapter 5).

The work described in this thesis has been carried out at the Department of Chemistry, Materials and Chemical Engineering of Politecnico di Milano.

CONTENTS

PART ONE

PART TWO

PART ONE

CHAPTER 1

Polymer-Metal Oxide Hybrid Solar Cells

1.1 Introduction

The global energy demand is mainly fulfilled today by burning fossil fuels, leading to several problems and threats such as declining reserves, political instability and gaseous emission causing global environmental changes. The need for alternative energy sources is therefore continuously growing. Among these, the use of solar energy is one of the most promising options. The sun provides energy to our planet with an average rate of about 100 000 TW, which exceeds the world's present rate of energy consumption of approximately 14 TW by 7000 times. In other words, the energy involved in only 1 hour of sunlight falling on our planet equals the total amount of energy used by the whole world population annually. Within the present contest, research efforts are therefore devoted to the development of solar cells with better performances and/or lower costs of production.

Over the past decades, solar cells based on organic semiconductors or hybrid organic/inorganic architectures have become a promising alternative to their all-inorganic, silicon based, counterparts. The lower performances in converting sunlight into electricity are compensated by lower costs of production and the possibility of large areas implementation.

While the so-called photoelectrochemical cells sensitized by ruthenium dyes still exhibit the highest power conversion efficiencies among molecular devices, up to 13% on small area cells and 5-7% for large modules,[1] bulk heterojunction solar cells based on conjugated polymers and fullerene show the promise of flexibility and versatility at low costs,[2] benefiting from solution processing, patterning and roll-to roll manufacturing, with efficiencies over 9% for improved polymer-fullerene blends.[2] The heterojunction supplies the driving force for

8

charge separation that is necessary to dissociate the tightly bound, photo-generated excitons into separate charges, by means of the difference in ionization potential and electron affinity of the two materials. High photocurrent quantum efficiency requires a high probability of exciton generation close to the donor-acceptor interface, and this is achieved by means of a dispersed (i.e. bulk) heterojunction, where the two components are combined in such a way that the interface presents a very large area compared to the geometrical area of the device.[2] More recently, hybrid systems consisting of conjugated polymers and inorganic nanocrystals (NCs), have been investigated for photovoltaic applications.[3] To date, various inorganic NCs such as CdS, CdSe, CdTe, ZnO, TiO_2, PbS and PbSe have been used as electron acceptors.[4] Although thus far the best performance in polymer-inorganic hybrid solar cells has been achieved with II-VI NCs, with power conversion efficiencies up to 3%,[4b] this thesis will discuss only the use of metal oxide NCs like TiO_2 and ZnO. These materials are promising for photovoltaic applications because they are environmentally friendly, avoiding the use of toxic components such as Cd or Pb, and available at low costs. They can be synthesized using wet chemical methods, enabling full compatibility with the solution-processable fabrication of polymer solar cells. In addition, metal oxides enjoy a large experience from research into photocatalysis,[5] gas sensors[6] and dye-sensitized solar cells (DSSCs).[1]

Nanostructured TiO_2 has been studied as a photovoltaic material since the 1980s, when the first observations of efficient photoinduced charge injection from dyes into TiO_2 were reported,[7] establishing the basis for DSSCs.[1] Indeed, in this type of solar cells, after absorption of a photon, the excited electron within the sensitizer molecule is transferred to the

conduction band of TiO_2, and diffuses through the porous metal oxide network to the electric contact. The oxidized sensitizer is reduced to the original state by supply of electrons through a liquid electrolyte redox couple, the most commonly used being the iodide/triiodide redox couple, which also ensures the contact with the platinum counter electrode (Figure 1.1).[1]
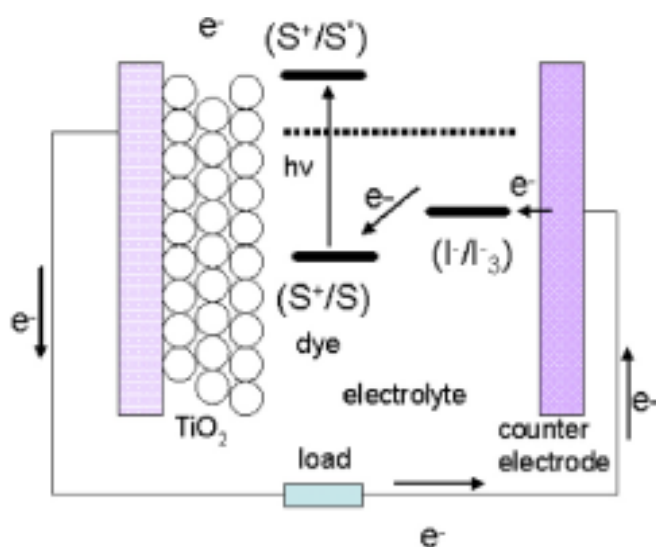
Figure 1.1. Operating principle of a dye sensitized solar cell.

The replacement of the electrolyte with a p-type semiconductor or with an organic hole-conductor material avoids problems related to the leakage of liquid electrolyte and corrosion due to the iodide/triiodide couple but causes a drastic decrease of the energy conversion efficiencies (2-5%).[1b]

Conjugated polymers commonly used for organic photovoltaics (OPV) are also suitable candidates in hybrid photovoltaics (HPV), in particular poly-3-hexylthiophene (P3HT) receiving higher attention among others (Figure 1.2).[3a]

10
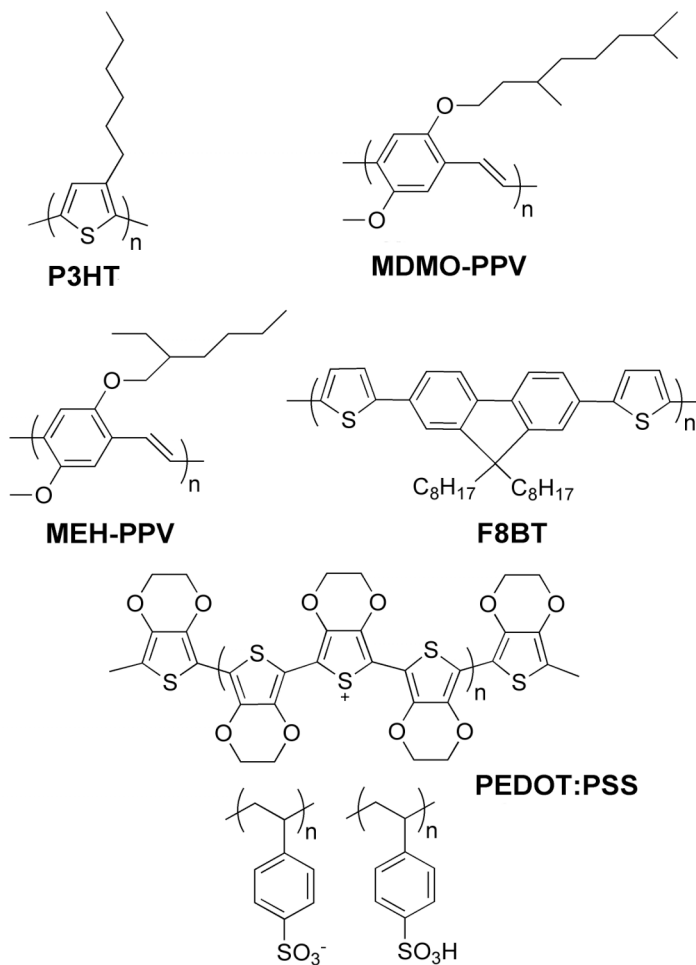
Figure 1.2. Chemical structure of conjugated polymers most commonly used in OPV and HPV. Poly-3-hexylthiophene (P3HT), poly[2-methoxy-5-(3′,7′-dimethyloctyloxy)-1,4-phenylenevinylene] (MDMO-PPV), poly[2-methoxy-5-(2-ethylhexyloxy)-1,4-phenylenevinylene] (MEH-PPV), poly-(9,9'-dioctylfluorene-co-bithiophene) (F8T2), poly-(3,4-ethylenedioxy-thiophene)-poly(stirenesulfonate) (PEDOT-PSS).

The sensitization of TiO_2 by conjugated polymers or molecular films rather than by chemically absorbed dye monolayers became of interest in the late 1990s following the first reports of photocurrent generation from conjugated polymer-based heterojunctions.[8] Several studies established that efficient photoinduced electron transfer from conjugated polymers in

11

to TiO_2 was possible.[9] Also in this case, when a photon is absorbed in the polymeric material, the exciton so created will dissociate into separate charges at the interface. If the composite system is enclosed between two electrodes with asymmetric affinities for electrons and holes, the separate charges can then be collected to generate a photocurrent (Figure 1.3).[9]
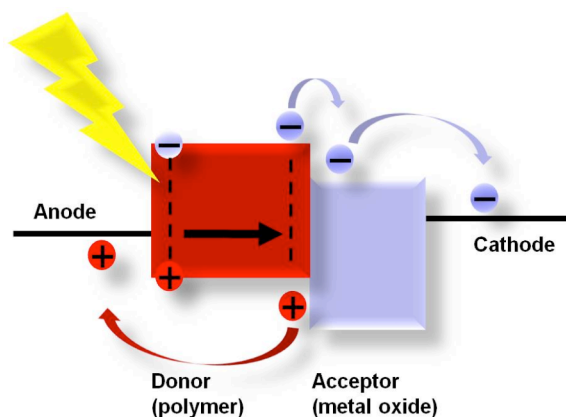
Figure 1.3. Scheme of the operating principles of a polymer-metal oxide hybrid solar cell, showing the dissociation of excitons at the hybrid heterojunction and the charge transportation process. The exciton migration towards the hybrid interface and the electron and hole transfer processes are indicated with arrows.

Relative to dye-sensitized solar cells, a solid nanostructured TiO_2–polymer solar cell offers the potential advantage of useful photo-currents at much smaller device thicknesses, because the entire pore volume is filled polymer, which acts both as sensitizer of the metal oxide and as hole transporter. Relative to all-organic polymer-fullerene and polymer-polymer structures then, the design offers rigidity and hence mechanical stability of the nanostructure. Furthermore, metal oxide nanoparticles are particularly suited for the role of electron acceptors, showing relatively high electron mobilities and good physical and chemical stabilities,[10] and optical properties which can favor light trapping within the active layer

12

of the device. In addition, the morphology of the inorganic NCs can be varied from those of nanoparticles (NPs),[11] nanorods (NRs)[4a,12] and tetrapods,[4b,13] depending on the various synthesis techniques, which provide different BHJ morphologies in polymer-inorganic hybrid solar cells, compared to polymer-fullerene devices.

There are different ways for preparing polymer-metal oxide hybrid solar cells (Figure 1.4).
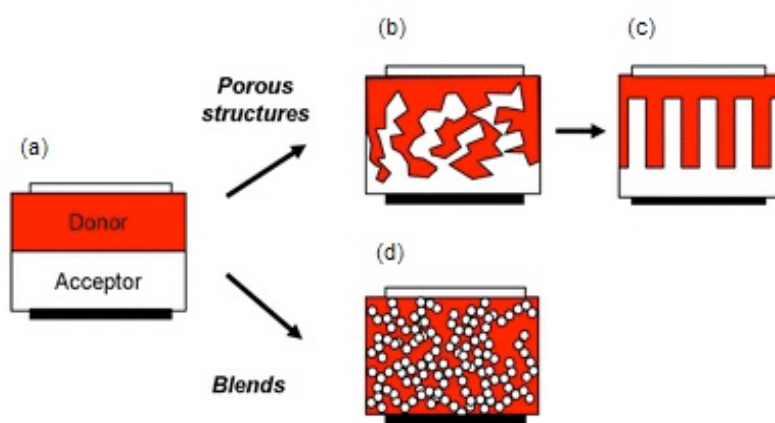
Figure 1.4. Type of polymer-metal oxide donor-acceptor heterojunctions. (a) A planar bilayer film, (b) a blend of polymer and metal oxide nanoparticles, (c) a porous acceptor phase filled with donor, (d) an "ideal" heterojunction containing vertically aligned domains.

One is to make use of simple planar bilayer structures where an organic layer is deposited on top of an inorganic semiconductor layer; another one is to blend dispersed metal oxide NCs with the polymer to form BHJs, similar to those in the most popular polymer-fullerene BHJ solar cells and another is to infiltrate the polymer into rigidly connected metal oxide nanostructures directly grown on substrates.

The first reports of hybrid polymer-TiO$_2$ photovoltaic devices[14] showed that photocurrent generation (albeit modest) could be achieved and that

13

bilayer, porous nanostructures and blend structures could all be exploited. These early studies soon established that structuring of the TiO$_2$–polymer interface leads to increased photocurrents relative to a bilayer structure with a planar interface,[15] so establishing the key role of the metal oxide-polymer interface morphology. Because photocurrent generation is a multi-step process in HPV, as in OPV, which involves charge separation, charge carriers recombination and transport, understanding the interplay between controlling the nanoscale morphologies of polymer-metal oxide NC hybrids and photocarrier dynamics is crucial for improving the device performance. Despite hybrid heterojunctions are characterized by an adequate matching of energy levels and, in particular for nanostructures, by an ideal configuration with large interface area and preformed percolative paths, solar cell devices show remarkably poor power conversion efficiencies, which remain generally below 1%. The reason for such low values is the poor interaction between inorganic nanocrystals and conjugated polymers, which makes more challenging the obtainment of an optimized donor-acceptor interface compared to conventional polymer-fullerene solar cells.

In the next paragraphs, the current status of hybrid polymer-metal oxide devices based on both blends and porous structures will be described. The major challenges will be identified and critically discussed.

Before anyway, a brief overview about the parameters used to characterize the efficiency of a solar cell will be given, which will allow a better understanding of the following contents. The current-voltage characteristics of a solar cell in the dark and under illumination are shown in Figure 1.5.

14
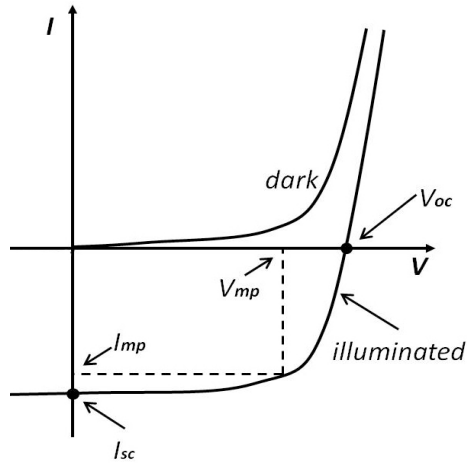
Figure 1.5. Current-voltage characteristics of a solar cell in the dark and under illumination.

In the dark there is almost no current flowing until the contacts start to inject heavily at forward bias for voltages larger than the open circuit voltage. Under light illumination, charges are photogenerated and the *I-V* curve shifts to the fourth quadrant and the device effectively generates power. The maximum power point (P_{max}) is the product of the maximum cell current (I_{mp}) and voltage (V_{mp}) where the power output of the cell is highest. The fill factor (*FF*) is a measure of how far the I-V characteristics of an actual PV cell differ from those of an ideal cell. The fill factor is defined as:

$$FF = \frac{I_{mp}V_{mp}}{I_{sc}V_{oc}}$$

where I_{sc} is the short-circuit current and V_{oc} the open-circuit voltage. As defined the fill factor is the ratio of the maximum power to the product of the short-circuit current and the open-circuit voltage. The ideal solar cell has therefore a fill factor equal to one. Another important parameter is the power conversion efficiency (η or PCE), defined as the ratio of the maximum power output to the power input on the cell:

15

$$\eta = \frac{P_{max}}{P_{in}} = \frac{I_{sc}V_{oc}FF}{P_{in}}$$

The incident light power density (P_{in}) is standardized at 1000 W m^{-2} for solar cells testing, with a spectral intensity distribution matching that of the sun on the earth's surface at an incident angle of 48.2°, which is called the AM 1.5 spectrum.

1.2 Polymer-metal oxide BHJ hybrid solar cells

1.2.1 Structure and limitations to device performance

In typical polymer-based BHJ solar cells, it is concluded that the device performance strongly depends on the optimized phase-separated donor-acceptor morphology of the BHJ, which ensures efficient dissociation of photogenerated excitons and continuous pathways for transporting charge carriers to electrodes. Substantial progress in the control of nanoscale BHJ morphologies in polymer-fullerene systems has been made by finding strategies to address the formation of a nanomorphology containing vertically phase-segregated donor-acceptor regions and continuous transport channels for both types of charge carriers toward top and bottom electrodes.[16] For polymer-metal oxide hybrid solar cells based on a BHJ structure, blending dispersed NCs (a few nanometers in diameter) within a polymer matrix results in a large number of donor-acceptor interface areas for charge separation. The precarious control on the BHJ morphology of two intermixed components for forming distinct electron- and hole-transport paths (the so-called bi-continuous phase) is anyway still a great challenge in improving the device performance. Typical blend device architecture is presented in Figure 1.6.

16
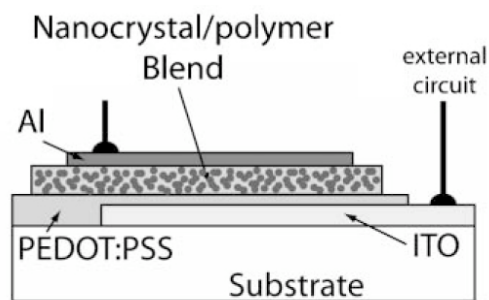
Figure 1.6. Typical structure of hybrid nanocrystal/polymer blend photovoltaic devices. Charges separated at the interface rely on differences in the work function of the electrodes for direction of the photocurrent.

Many key factors govern the morphologies and photocarrier dynamics of polymer-metal oxide NC BHJ solar cells. First, dispersing inorganic nanocrystals within organic conjugated polymers to avoid aggregation is a challenge in organic-inorganic hybrids. Another critical issue is that charge transport through the nanocrystalline phase is highly sensitive to the morphology and the connectivity of that phase, which strongly depend on the size, anisotropy and concentration of NCs, as well as to the presence of trap states within these ones. Interfacial engineering between the polymer and metal oxide NCs is another critical issue regarding device performance. Fine control of the phase segregation at the nanoscale requires the presence of capping agents such as trioctylphospine oxide (TOPO) or oleic acid (OA), which prevent particle agglomeration and assist in the dispersion of hydrophilic NCs in common organic solvents used to dissolve conjugated polymers, but these surfactants usually contain insulating long alkyl chains, which act as a barrier for exciton dissociation and charge transport.[17] Removal of insulating ligands on NC surfaces is usually required to achieve high device performance.[15] However, once the capped ligand on an NC surface is removed, the NCs tend to aggregate, and cannot be dispersed

17

uniformly within a conducting polymer, which largely suppresses the photovoltaic response by bad film-forming properties. Moreover, blend devices usually exhibit very low open-circuit voltages and fill factors compared to bilayer structures due to the presence of continuous pathways for either charge from top-to-bottom electrodes, causing charge leakage.

1.2.2 Effect of nanocrystals dispersion on device performance

Control of the blend morphology through processing, annealing, and solvent choice is important in affecting the phase intermixing, and hence the device performance.

Bouclé et al. employed thermal annealing at 120 °C under an inert atmosphere to improve the morphology of P3HT-TiO$_2$ nanorods BHJ solar cells.[18] Annealing typically improves the polymer crystallinity in P3HT-fullerene blend devices resulting mainly in higher hole-mobilities, whereas the main effect of the thermal treatment on the hybrid P3HT-TiO$_2$ NRs system seems to be related to a radical improvement of the local polymer/metal oxide interface, resulting in a strong increase of the charge separation yield. In contrast, controlling the polymer-metal oxide NC hybrid morphology through the choice of appropriate solvents seems more effective in improving the active layer operation. Kwong et al. found that employing a low vapor pressure solvent such as xylene in a P3HT-TiO$_2$ hybrid blend can effectively improve the mixing of the TiO$_2$ NPs and P3HT. The P3HT chains were more extended in the film spin-coated from xylene, and let to better mixing with TiO$_2$ NPs. This resulted in the obtainment of a morphology constituted by numerous domains and interfaces for efficient exciton separation. The power conversion efficiency was largely improved from 0.03% when using chloroform to

18

0.42% when using xylene.[19] Chuang *et al.* reported a method for controlling the dispersion of TiO$_2$ NCs within the P3HT matrix by using a mixed solvent method.[20] The P3HT-TiO$_2$ NCs hybrid was dispersed in a solvent mixture of chloroform, dichlorobenzene (DCB) and pyridine. CHCl$_3$ and DCB are good solvents for P3HT, whereas pyridine is a poor solvent. The presence of DCB prolongs the solvent-drying process and the presence of pyridine induces the P3HT polymer chains to form a fiber-like crystalline structure, which enhances π-π stacking, resulting in a distinct vibronic transition feature in the absorption spectrum. The presence of pyridine facilitate P3HT crystallization, while at the same time favoring the dispersion of the TiO$_2$ NCs in the hybrid solution, which instead tend to aggregate when only CHCl$_3$ is employed. By using this method, an improved PCE of approximately 1% could be achieved.

Another method of realizing a hybrid nanoscale inorganic NCs and polymer BHJ morphology is the use of *in situ* generation of an inorganic semiconductor inside the organic material. In this process, a well-soluble organometallic precursor is deposited from solution together with the semiconducting polymer. During and after this deposition, the precursor is converted into an inorganic network inside the polymer film by reacting with moisture from the surrounding atmosphere. Moet *et al.* deposited the photoactive layer by spin-coating a blend of diethylzinc and P3HT from a mixture of chlorobenzene, toluene and tetrahydrofuran onto an ITO electrode. During spin-coating, diethylzinc was exposed to humidity, causing hydrolysis and the formation of Zn(OH)$_2$. Only moderate thermal annealing at 100 °C was required for the condensation reaction to complete and to form an interpenetrating network of ZnO inside the polymer matrix. This provided a remarkable 1.4% efficient photovoltaic cell.[21]

1.2.3 Effect of nanocrystals size and shape on device performance

The size and shape of NCs is another critical factor in determining the optimal morphology of polymer-metal oxide BHJ solar cells. Li *et al.* demonstrated the optimal device performance for both P3HT-TiO$_2$ NPs and nanorods (NRs) hybrid thin films by using TiO$_2$ NCs with a characteristic size of approximately 5 nm for NPs and approximately 4 nm in diameter and roughly 20 nm in length for NRs as shown in Figure 1.7.[22]
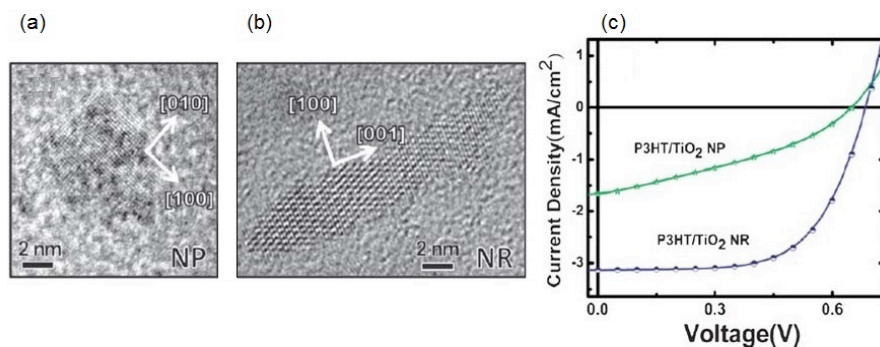
Figure 1.7. High resolution TEM images of (a) NPs and (b) NRs. (c) Current-voltage characteristics of P3HT-TiO$_2$ NPs and NRs hybrid BHJ solar cells.

Ligand exchange treatment by pyridine on both TiO$_2$ NPs and NRs was used to remove the original OA surfactant on the as-synthesized surface of the TiO$_2$ NPs and NRs. The resulting devices based on P3HT-TiO$_2$ NRs hybrid thin film exhibits better performance, with a J_{SC} of 3.10 mA cm^{-2}, a V_{OC} of 0.69 V, and a *FF* of 0.62, resulting in a PCE of 1.33%, compared to the P3HT-TiO$_2$ NPs hybrid device, which had a J_{SC} of 1.65 mA cm^{-2}, a V_{OC} of 0.60 V, and a *FF* of 0.42, yielding a PCE of 0.42%. This result indicates that the NCs shape can largely affect the deviceperformance, and the relatively high FF (0.62) of the P3HT-TiO$_2$ NRs hybrid device suggests that a favorable BHJ morphology may exist

20

for efficient charge carrier transport and collection.

1.2.4 Effect of interface modification on device performance

As mentioned before, because the surface of as-synthesized metal oxide NCs is usually capped with insulating surfactants which act as a barrier for charge transfer and charge transport, the modification of the interface between the polymer and the NCs is another strategy to improve device performance. Bouclé *et al.* replaced the surfactant molecule (TOPO) with amphiphilic ruthenium dye (Z907) on an inorganic NC surface in a P3HT-TiO$_2$ NRs hybrid solar cell (Figure 1.8).[17]
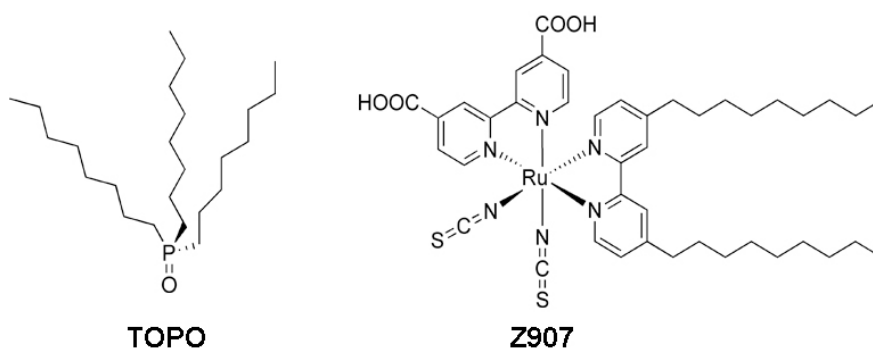
Figure 1.8. Chemical structures of trioctylphospine oxide (TOPO) and amphiphilic polypyridine ruthenium complex (Z907) *cis*-RuLL'(SCN)$_2$ (L = 4,4'-dicarboxylic acid-2,2'-bipyridine, L' = 4,4'-dinonyl-2,2'-bipyridine).

The charge separation efficiency at the heterojunction was found to be improved, and was associated with a three-fold increase in PCE. However, intrinsic charge trapping, poor inter-particle connectivity and geometric trapping of TiO$_2$ NCs may be the cause of limited photocurrent generation, resulting in a poor PCE of only 0.07% after ligand exchange. Lin *et al.* reported a ligand-exchange method that can be used in P3HT-TiO$_2$ NRs hybrid systems by removing the insulating

21

surface ligand (OA) on a TiO$_2$ NR surface through pyridine treatment.[23] Device performance enhanced significantly from 0.38% to 1.14%. Afterward, the same group demonstrated interface modification between P3HT and TiO$_2$ NRs by attaching effective interfacial molecules on the TiO$_2$ NR surface,[4a] which improved the compatibility between the polymer and TiO$_2$ NRs and also influenced the charge transfer efficiency at the hybrid interface, where the π-conjugated structures of those molecules interact with the thiophene moieties of P3HT.They replaced the original oleic acid with more effective interfacial modifiers such as anthracene-9-carboxylic acid (ACA), tetracarboxy phtalocyanine copper(II) (CuPc-dye) and *cis*-bis(4,4'-dicarboxy-2,2'-bipyridine) dithiocyanato ruthenium(II) (N3-dye), as schematically represented in Figure 1.9. Through this type of interface modification, the device performance of P3HT-TiO$_2$ NRs BHJ solar cells was substantially improved. All devices had FFs from 0.62 to 0.65, which is relatively high for polymer-inorganic hybrid solar cells. The solar cell that comprised of TiO$_2$ NRs modified with the N3-dye molecule demonstrated the best outcome, with a J_{SC} of 4.33 mA cm^{-2}, a V_{OC} of 0.78 V, and a *FF* of 0.65, yielding a PCE of 2.20%. It is worth nothing that the amount of dye adsorbed on the TiO$_2$ NRs was estimated to be approximately 10^{-11} to 10^{-12} mol cm^{-2}, which is considerably less than that commonly used in dye-sensitized solar cells (usually in the order of 10^{-7} mol cm^{-2}). The negligible optical density of the interface layers of these molecules in relation to that of P3HT indicates that these ligand molecules modify the interface rather than harvesting light, as it is evident from the corresponding external quantum efficiency (EQE) spectra that resemble the polymer absorption band. The molecules at the interfaces of P3HT-TiO$_2$ NRs have two major roles in improving the device performance:

22
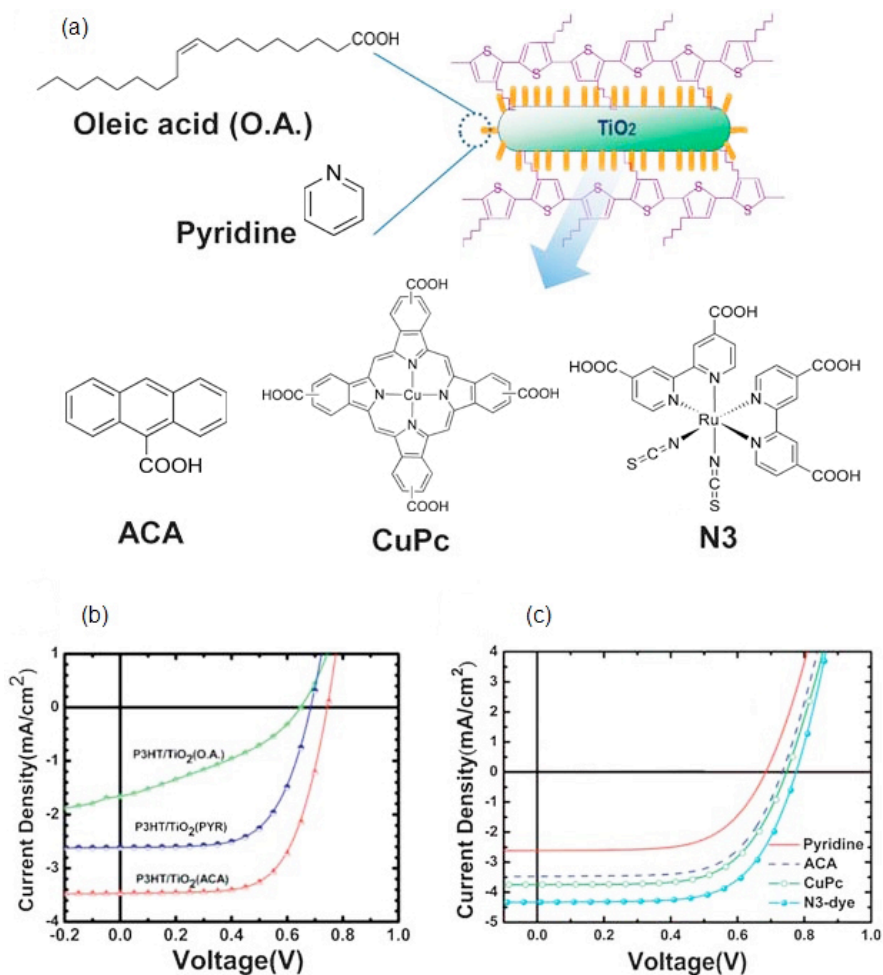
Figure 1.9. (a) Schematic representation of the ligand exchange process. Insulating oleic acid was removed by pyridine or replaced by interfacial molecules such as ACA, CuPc-dye or N3 dye. (b), (c) Current-voltage characteristics of the P3HT-TiO$_2$ NRs BHJ solar cell with various surface ligands.

increasing the compatibility between the polymer and TiO$_2$ NCs and preventing back-recombination of photo-generated charges. Furthermore, the reduced recombination rates may lead to increased electron and holes concentration at the interface, raising the difference between the quasi-Fermi levels of electrons and holes and accounting for the observed increase in V$_{OC}$. Therefore, through interface modifications on the NC

23

surface, the device performance can be significantly improved because of the enhanced charge separation, improved compatibility and large suppression of back-recombination. Huang *et al.* studied the effect of two amphiphilic interfacial modifiers (IMs), a low cost copper phtalocyanine dye containing ether side chains (CuPc-ether-dye) and a carboxylic acid- and bromine-terminated 3-hexyl thiophene oligomer (oligo-3HT-(Br)COOH, M_w~5K), to enhance the interfacial interaction between P3HT and TiO_2 NRs (Figure 1.10).[24]
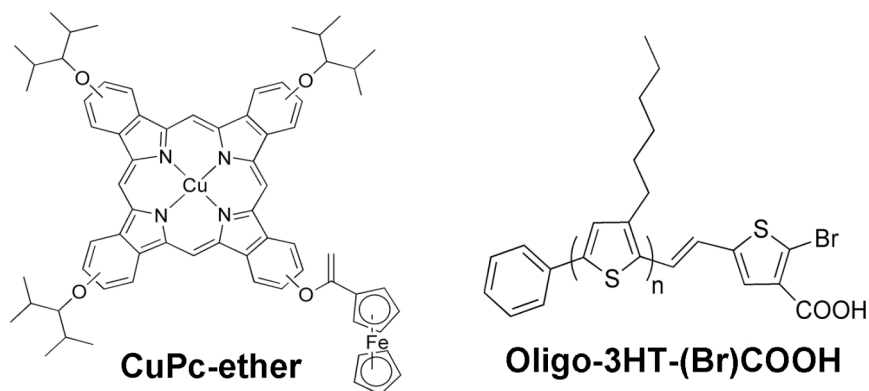
Figure 1.10. Chemical structure of the CuPc-ether dye and of the oligo-3HT-(Br)COOH.

A large improvement in the performance of fabricated solar cells was observed using these relatively large molecular modifiers when compared to unmodified and pyridine-modified TiO_2 NRs. The new modifiers were shown to make TiO_2 NRs more hydrophobic with the order: oligo-3HT-(Br)COOH > CuPc-ether dye > pyridine. The P3HT cristallinity in the hybrid blends is also increased following the same trend as the hydrophobicity, because the new modifiers function as plasticizers, increasing the flow characteristics of the film. Moreover, the

24

same trend was observed for the reduced charge recombination rate and increased lifetime of charge carriers in the devices by transient photo-voltage measurements. Thus the oligo-3HT-(Br)COOH modifier outperform the CuPc-ether dye and pyridine in enhancing the power conversion efficiency of the solar cell. More than a two-fold improvement in PCE was shown compared to pyridine (from 0.54% to 1.19%).[24]

Another strategy for improving the compatibility between a polymer and inorganic NCs is to modify the polymer by end-group functionalization. Oosterhout *et al*. reported a polymer-ZnO hybrid solar cell based on a hydrophilic polymer P3HT-E, poly[(3-hexylthiophene-2,5-diyl)]-*co*-(3-(2-acetoxyethyl)thiophene-2,5-diyl)], whose chemical structure in shown in Figure 1.11.[25]
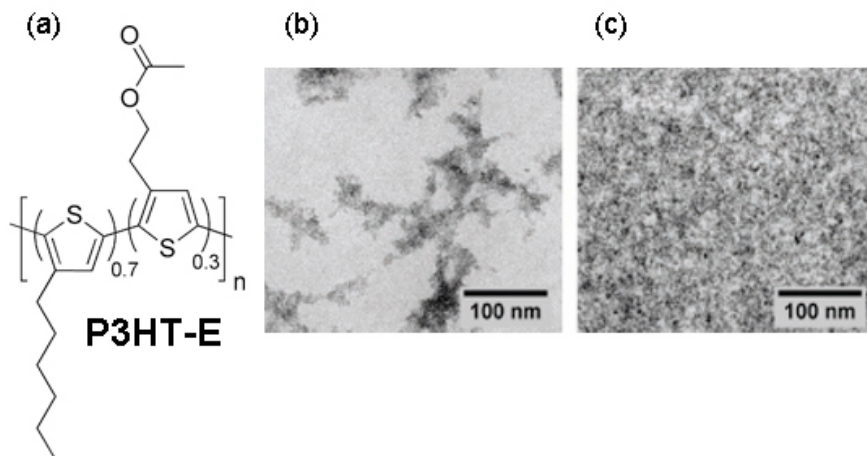
Figure 1.11. (a) Chemical structure of P3HT-E. (b) The TEM image of the nanomorphology in the P3HT-E-ZnO NCs hybrid film.

The ester-functionalized side chains make the polymer more hydrophilic and more compatible with the ZnO polar surface than P3HT. The ZnO NCs were directly synthesized in a P3HT-E matrix from a precursor

25

during the spin-coating process and the film surface was substantially smoother than that of the P3HT-ZnO hybrid because of better miscibility of P3HT-E and ZnO. The use of P3HT-E leads to a considerably finer phase separation (Figure 11), as well as an improved charge generation efficiency (from 32% to 90%). This method can be used to yield a significant improvement of the solar cell performance only in thin ZnO-P3HT-E active layer (approximately 50 nm). For thicker cells, the reduced hole-mobility in the functionalized polymer and the reduced electron percolation along ZnO pathways hinder charge collection at the opposite electrodes, limiting the PCE.

Redeker *et al.* reported on novel core-shell hybrid heterojunction nanostructures obtained by covalently grafting a commercially available P3HT derivative bearing carboxylic acids substituents in the ω-position of the lateral alkyl chains (P3HT-COOH) onto ZnO nanowires (Figure 1.12).[26]
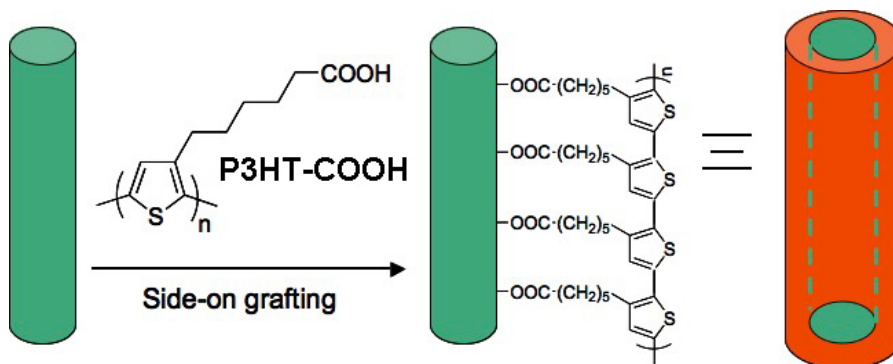
Figure 1.12. One-dimensional coaxial core-shell nanohybrids obtained by direct covalent attachment of P3HT-COOH onto ZnO nanowires.

They employed the solvatochromic behavior of P3HT-COOH as a tool for controlling the polymer conformation at the polymer-nanowire interface and found higher cristallinity in the organic material, because of

its geometrical confinement onto the nanowire surface. Photophysical studies on these P3HT-ZnO nanocomposites demonstrated a fast interfacial photoinduced charge transfer from the polymer to the ZnO nanowires. Furthermore, the intrinsic shape anisotropy of these 1D P3HT-ZnO nanohybrids allows them to spontaneously form lyotropic liquid crystalline phases. This ability might be exploited to obtain vertically aligned bulk heterojunctions, as required for high-efficiency photovoltaics, under appropriate vertical shear flow conditions, which can be achieved, for example, during the screen-printing process. Even if the authors provide a critical insight into their utilization to control donor-acceptor interfaces and as photovoltaic elements for the massive fabrication of high-efficiency devices, they didn't test yet the P3HT-ZnO nanocomposite as active layer in hybrid solar cells.

Lin *et al.* used a series of functionalized P3HT copolymers of poly(3-hexylthiophene-*b*-ethylene glycol) (P3HT-*b*-PEG) to improve the efficiency of P3HT-TiO$_2$ NRs BHJ solar cells.[27] The short PEG segments in P3HT-*b*-PEG serve as hydrogen bond acceptors. A strong preferential H-bonding interaction between TiO$_2$ NRs and the PEG chain circumvented the aggregation of TiO$_2$ nanorods, resulting in a homogeneous dispersion of NCs within the P3HT matrix to form an interpenetrating network (Figure 1.13). The hybrid device consisting of 10% PEG and N3-dye TiO$_2$ NRs exhibits an optimal PCE of 1.71 %, which is approximately 50% higher than that obtained by using only conventional P3HT homopolymer. Nevertheless, although PEG can facilitate the dispersion of NCs in polymers, the hybrid device using the P3HT-*b*-PEG copolymer shows a relatively low FF of approximately 0.4 because of a less efficient charge transport.
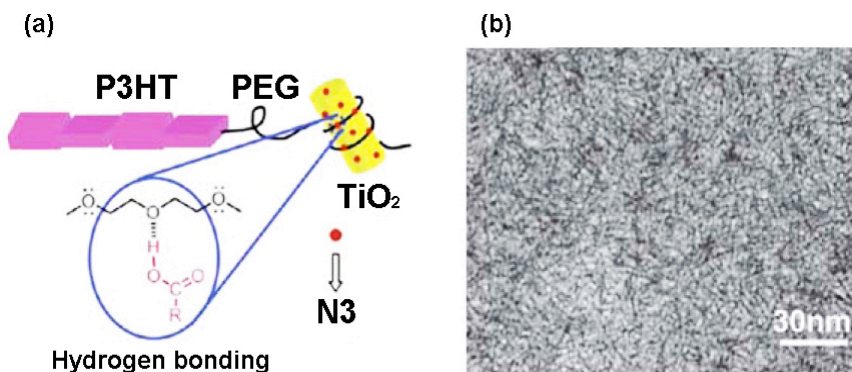
Figure 1.13. (a) Schematic illustration of the P3HT-*b*-PEG-TiO$_2$ NR hybrid and (b) its corresponding TEM morphology.

1.3 Nanostructured polymer-metal oxide hybrid solar cells

1.3.1 Structure and main issues related to device performance

Despite promising PCEs obtained in polymer-metal oxide BHJ solar cells, properly balancing photo-generation and charge transport remains a challenge in controlling the morphology of polymer-inorganic NCs blends. By contrast, nanostructured metal oxide-polymer hybrid solar cells, which consist of pre-constituted and well-connected transport paths in the active layer, offer a rigid morphology of inorganic NCs formed prior to polymer deposition.

A key factor in achieving high PCE as well as high EQE is the choice of the electrode materials. In porous polymer-metal oxide structures the metal oxide acceptor layer is normally deposited on top of a transparent conducting oxide-coated glass substrate and an evaporated metal is finally deposited on top of the active layer as a hole-collecting contact. This polarity is the opposite of most commonly reported organic solar cell structures where the conducting oxide (usually indium tin oxide, ITO) acts as the hole-collecting electrode. Since the work function of ITO (4.5-4.7 eV) is intermediate between typical HOMO and LUMO

28

values for organic photovoltaic materials, ITO can, in principle, collect either electrons or holes. If the ITO is not insulated from the donor material in the porous metal oxide-polymer structure, charge leakage occurs and the device current-voltage (*J-V*) characteristic suffers from a low fill factor. The opposite electrode should have a sufficiently high work function to collect holes from the donor material. A high work function electrode can be provided by a layer of a doped conducting polymer such as PEDOT-PSS under the metal top contact or a high work function metal such as platinum.[15] Poor matching of the anode work function and donor HOMO level leads to a sigmoidal *J-V* curve, characteristic of a low conductivity interface and, again, a low fill factor. The anode selectivity can be further improved using a donor material to insulate the contact from the metal oxide. Figure 1.14 shows the effects on device *J-V* characteristics of a porous polymer-TiO_2 structure due to a dense TiO_2 hole-blocking layer (HBL) between polymer and ITO, and to a spin-coated polymer electron-blocking layer (EBL) between metal oxide and top electrode, both preventing shunt pathways for charge carriers. A 0.58% PCE was achieved for the multilayer device structure incorporating both these buffer layers and suitable electrode materials.[12] The main factors limiting the device performance are:

✓ the incomplete infiltration of the polymeric material into the free space of the metal oxide nanostructure, which is influenced by several factors such as pore size, shape and depth and also polymer molecular weight;

✓ the number of interfaces, which is limited by the relatively large dimensions of metal oxide nanostructures compared to that in the polymer-metal oxide BHJs;

✓ an overly small effective volume of the polymer lying within an

29
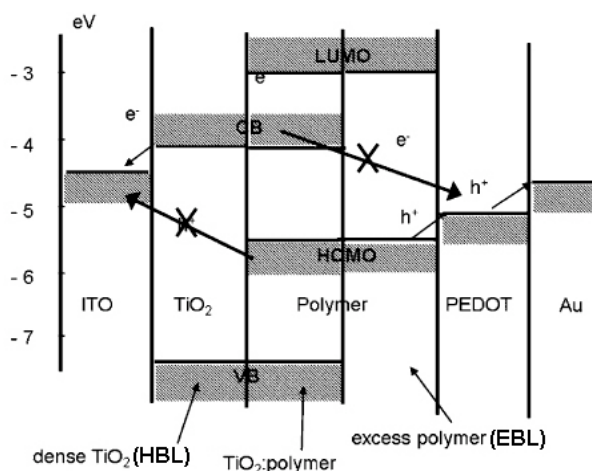
Figure 1.14. Electronic energy-level diagram for porous TiO_2 -polymer devices. The dense TiO_2 and the spin-coated excess polymer layer block hole-transfer from polymer to TiO_2 and electron-transfer to the top electrode respectively.

exciton diffusion length from the interface and

✓ the ineffective charge transport across the polymer phase due to non-crystalline, un-orientated polymer chains.

1.3.2 Polymer infiltration

The degree of infiltration of a polymer solution into a porous metal oxide film is influenced by several factors: the molecular weight of the polymer and its tendency to crystallize; the pore size, shape and depth, the thickness of the porous film, the solvent employed for polymer deposition, the drying conditions and the surface-interaction energy of the two materials (*i.e.* their relative wettability hydrophilicity). Infiltration can be monitored through depth-profiling experiments with techniques such as X-ray photoelectron spectroscopy (XPS), while UV-visible and photoluminescence (PL) spectroscopy can help in understanding the main conformations adopted by the polymer inside the

30

mesopores.

The subject is highly debated and characterized by controversial literature data. Bartholomew *et al.* studied the infiltration of regioregular P3HT drop-casted from chloroform solution into 2 μm thick nanoporous TiO$_2$ network.[28] Depth profiles of the polymer treated TiO$_2$ films were obtained by means of secondary-ion mass spectrometry (SIMS) and the percentage of polymer infiltration was determined by monitoring the ratio of carbon-ion signal coming from the top P3HT overlayer to the carbon signal from the same polymer within the TiO$_2$ network. A very low incorporation of polymer was found (0.5%), even for highly porous (= 65%) networks. The level increased to 2.8% when the titania substrates were pre-treated with trichlorophenylsilane, which made the inorganic surface more adapt to be properly wet by the hydrophobic P3HT.

A better degree of P3HT penetration into mesoporous titania was reported by Coakley *et al*. Indeed, the 33% of the total internal volume of a 180 nm thick TiO$_2$ mesoporous film was filled with polymer by spin-casting a solution of the organic material on top of the mesoporous substrate and subsequently heating the hybrid sample at 200 °C for 1 h.[29] Following the heat treatment, the excess of polymer that did not infiltrate the mesoporous film was removed by rinsing the sample with toluene. Longer heating times did not improve the degree of polymer infiltration. Both UV-vis and PL measurements indicate that the chains of the regioregular P3HT are coiled and unable to efficiently π-stack inside the pores of the titania.

Abrusci *et al.* studied the P3HT pore infiltration into a dye-sensitized mesostructured TiO$_2$ through a combination of XPS depth profiling and cross-sectional transmission electron microscopy and found that uniform

31

pore filling of P3HT can be achieved to depths of over 4 μm.[30] Though the pore filling is uniform, it is not complete and the filled fraction is estimated to be in a range between 6 and 24% depending upon the precise processing conditions. Despite these low values, the polymer appear to form a "wetting film" over the entire surface of the dye-sensitized mesoporous electrode and this wetting layer with, on average, only a few nm thickness is sufficiently capable of regenerating the dye and transporting the holes out of the device, illustrating that pore filling is not the critical issue for mesoporous hybrid solar cells. Charge collection efficiency of up to 98% was estimated from transient electronic measurements and, notably, the photocurrent was almost exclusively generated from light absorbed in the dye. The authors therefore concluded that major improvements in hybrid solar cells are likely to be achieved by **switching focus on improving the charge generation at the polymer-metal oxide interface through correct engineering, rather than by devolving all research efforts to improving pore filling and charge transport within the polymer phase**.

1.3.3. Strategies to enhance the effective polymer-metal oxide interfacial area

The first porous films studied were made by sintering of isotropic, colloidal TiO_2 nanoparticles into a connected thin film. The resulting irregular morphology is not ideal either for infiltration of organic material or for ease of charge transport through either component. Currently, TiO_2 porous photoanode commonly used for DSSCs are basically processed starting from commercially available nanocrystals, which are synthesized by hydrothermal methods, where particle growth

32

occurs in an autoclave under 70 atm, at 200-250 °C for 12 h.[31] The typical nanocrystal morphology, illustrated for particles grown under hydrothermal conditions in Figure 1.15, exhibits mainly facets with (101) orientation, the lowest surface energy for anatase. Subsequently, re-dispersion of the nanocrystals in ethanol, followed either by the addition of surfactants such as ethyl cellulose and/or poly(ethylene glycol) or by prolonged ultrasonication, leads to a metal oxide paste suitable for screen-printing or doctor-blading deposition. A short sintering step at 500 °C is required in order to induce the electrical interconnection of particles and remove the organic phase from the film. In this conventional process, surfactants are not critical components as they are mostly removed after this calcinations step and do not interfere in the final solar cell under normal operation. The situation is clearly very different when TiO_2 nanocrystals are blended with a p-type semiconductor, as was discussed previously for polymer-nanocrystals blends. Nanocrystalline electrodes can develop high surface areas up to 150 m^2 g^{-1}, compatible with particle mean diameters of 10-20 nm. A high porosity of the film is evidenced, with a pore volume to film volume ratio in the range of 0.5-0.7.

In a general opinion, vertically aligned metal oxide nanorods,[32] nanofibers,[33] nanotubes,[34] nanosheets[35] or nanotrees[36] arrays (Figure 1.16) with dimensions of the order of the exciton diffusion length of the polymer donor are believed to be the ideal case of nanostructured metal oxide-polymer hybrid solar cells (Figure 1.2d).

Nanometer-scale periodicity would minimize radiative decay of excitons and the vertical alignment of the materials ensures non-tortuous paths for charge transport. Hybrid nanostructured solar cells using P3HT and vertically aligned ZnO nanorods prepared using sol-gel methods were proposed by several groups.[32,37] These ZnO NRs-P3HT devices show
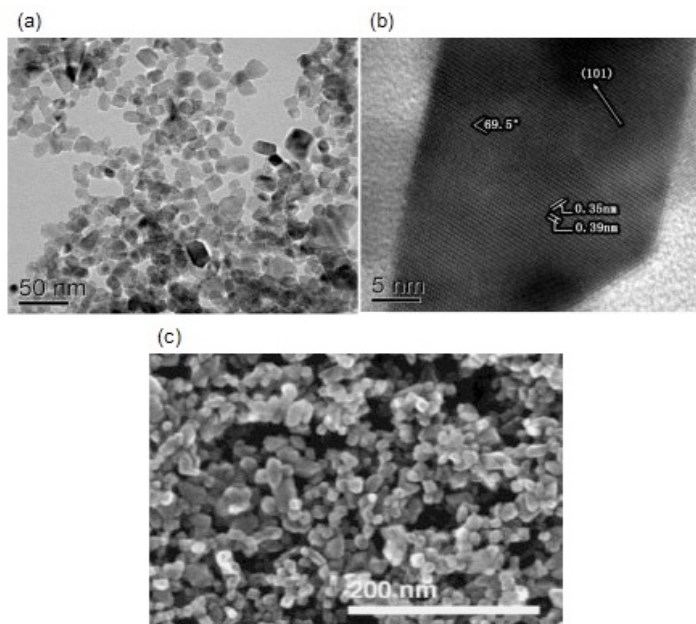
Figure 1.15. Typical morphology of anatase TiO_2 nanocrystals synthesized under hydrothermal conditions at 240 °C in nitric acid solution observed using TEM at (a) low and (b) high magnification, (c) Resulting morphology of a typical nanocrystalline porous TiO_2 electrode after sintering at 500 °C (SEM image).

substantially higher photocurrent generation than planar devices. Lee *et al.* reported a quantitative estimation of an approximately 2.7 enhancement factor in the short-circuit current of a hybrid device, which was obtained using a vertically aligned 180 nm ZnO NR array, and was in agreement with the increase of the surface area compared to a bilayer device.[38] Several possible reasons limit the device performance of this type of solar cells. The spacing between the nanorods (approximately 100 nm) is substantially larger than the typical exciton diffusion length in P3HT (approximately 10 nm), limiting the efficiency of exciton dissociation and therefore resulting in suboptimal charge separation. Baeten *et al.* employed thermal annealing of as-prepared devices for
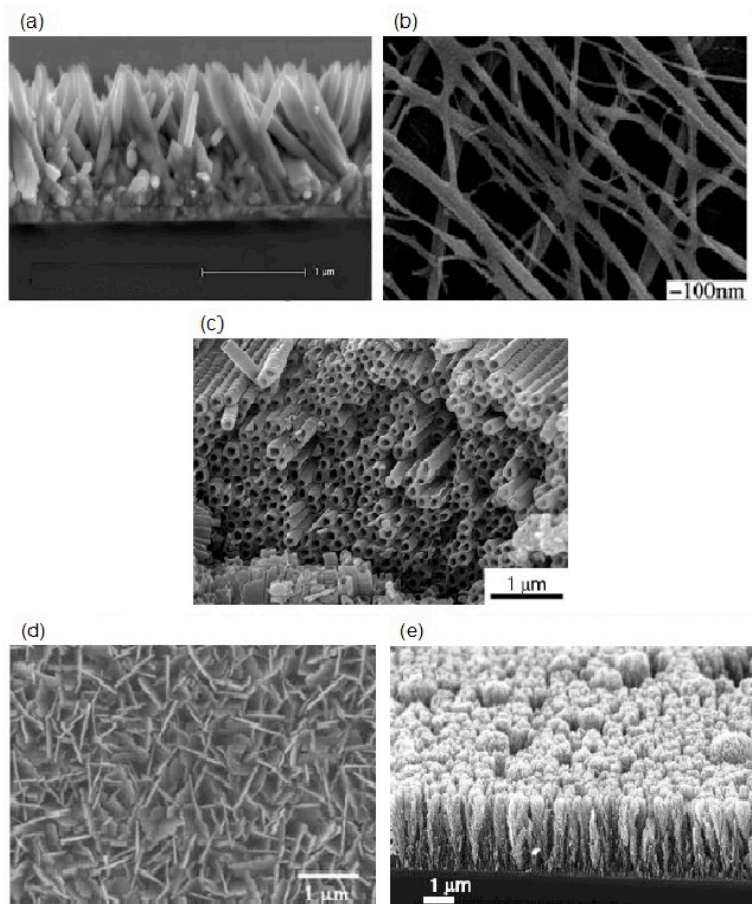
Figure 1.16. Various types of metal oxide nanostructures used as acceptors in nanostructured polymer-metal oxide hybrid solar cells. (a) ZnO nanorod array, (b) ZnO nanofibrous network, (c) TiO_2 nanotube array, (d) ZnO nanosheets, (e) TiO_2 nanotrees.

different time scales (1 min and 15 min) at the melting temperature of P3HT (225 °C).[39] By using X-ray photoelectron spectroscopy (XPS) depth profile analysis, they found a deep infiltration of the polymer into the ZnO nanorods array in the as-prepared state and significantly improved the device performance by post-annealing the hybrid system for a well defined time (1 min), as a consequence of improved P3HT crystallinity and full infiltration of the polymer into the nanorods array.

35

Annealing also provided the polymer more time to arrange between the nanorods, rendering the hybrid interface more intimate and thereby reducing geminate charges recombination. Combined with the control of leakage currents by means of appropriate blocking layers for electrons and holes, a V_{oc} of 0.543 V, a J_{sc} of 2.67 mA cm^{-2}, a FF of 53%, and a PCE of 0.76% were obtained, representing an optimal-performing P3HT-ZnO NRs hybrid solar cell. The HBL was provided by the seed layer, which was required for the synthesis of the ZnO NRs, whereas the remaining polymer capping layer on top of the NRs array constituted the EBL.

Other nanostructured metal oxide morphologies have also been proposed to fabricate polymer hybrid solar cells. Wu *et al.* reported a nanostructured hybrid photovoltaic device based on P3HT and an ordered electrospun ZnO nanofibrous network, in which the diameters of the ZnO nanofibers were controlled within 30-150 nm. The device exhibits an optimal PCE of 0.51%.[40] Tepavcevic *et al.* employed a TiO$_2$ nanotube array as a substrate for the in situ UV polymerization of thiophene monomers. By using this simple method, high pore filling factors were achieved and well-ordered and well-aligned polymer chains were synthesized, improving light absorbtion and charge carriers mobilities. Sung *et al.* demonstrated a ZnO nanostructure with the morphology of a nanosheet as an electron acceptor.[35] The ZnO nanosheet structure, which has similar characteristics to the ZnO NR array, such as vertical feature and a single-crystalline structure, was found to possess an appropriate amount of free space to facilitate P3HT infiltration, resulting in favorable interfacial properties leading to efficient charge separation and decreased charge recombination in the final hybrid solar cell. An efficiency of 0.88% was achieved. Compared with the ZnO NR array, the

36

ZnO nanosheet framework also exhibits a slightly larger absorption edge and fast electron transport properties because of the high surface-to-volume ratio. Passoni *et al.* recently studied dye sensitized solar cells based on tree-shaped hierarchical TiO$_2$ mesostructures obtained with the pulse laser deposition technique (PLD).[41] Spiro-OMeTAD was used as a solid state electrolyte and hole conductor to ensure regeneration of the oxidized dye (Figure 1.17).
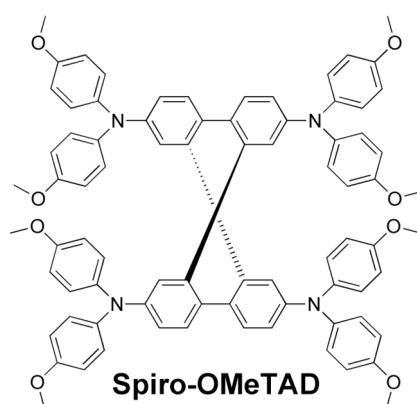
Figure 1.17. Chemical structure of the Spiro-OMeTAD hole conductor.

Optimized structural and morphological characteristics of the nanotrees array gave high specific surface area and broadband light scattering thanks to the microscopic feature size. A significant 66% increase in solar cell's efficiency was found with respect to a reference mesoporous photoanode. This result was achieved mainly thanks to an increase in photogenerated current directly resulting from improved light harvesting of the hierarchical photoanode. The proposed photoanode appears therefore to overcome the typical limitations of 1D TiO$_2$ nanostructures and emerges as a promising foundation for next-generation solid-state devices composed of dyes, polymers, or quantum dots as sensitizers.

Another strategy for improving nanostructured polymer-metal oxide

37

hybrid solar cells is to increase the effective areas of organic-inorganic interfaces. Lin *et al.* incorporated small TiO_2 NRs of approximately 5 nm in diameter and 20-30 nm in length in a vertically grown ZnO NRs array of approximately 50 nm in diameter and 180 nm in length.[42] A substantial improvement in the short-circuit current by a factor of seven was observed because of the enhanced charge separation efficiency.

1.3.4 Interface modification of polymer-metal oxide nanostructures

In addition to optimize the metal oxide nanostructure morphology, the surface modification of metal oxide nanocrystalline films is also an efficient strategy for improving the device performance. As discussed previously, interfacial modification plays an important role in improving the compatibility between the polymer and inorganic NCs. Although in the nanostructured metal oxide-polymer hybrid solar cell the morphology of the inorganic NCs is formed prior to the polymer deposition, interface modification still has significant effects. Ravirajan *et al.* demonstrated the incorporation of molecular interlayers for improving the performance of P3HT-ZnO NRs array heterojunctions.[32] Surface modification with a ruthenium dye (Z907) showed an improved power conversion efficiency of 0.2% by a factor of four compared to untreated P3HT-ZnO NRs array devices, because the recombination kinetics of the ZnO NRs array/Z907/P3HT device was found to be slowed by the interface modifier. In addition, molecular interface modifiers (IMs) can impart a dipole at the donor-acceptor interface and offset the interface energy, which may mediate the forward charge transfer or reduce the back recombination. Consequently, the energy offset at the TiO_2-polymer interface, and thus the V_{oc} of devices, can be tuned by using the interface modifiers with various dipoles. An upward shift of the TiO_2 conduction

38

band is expected to increase the maximum open-circuit voltage (V_{oc}) available from the structure. The optimum structure would therefore have a driving force for charge separation that is large enough to overcome the exciton binding energy in the donor, so that near unit charge-transfer efficiency is achieved. In P3HT-TiO$_2$ structures, for example, the energy difference between the LUMO of P3HT (~ -3.1 eV) and the TiO$_2$ conduction band edge ((~ -4.0 eV) is much larger than needed to drive exciton dissociation, and so large gains in V_{oc} could be made if the energy levels could be controlled. By systematically investigating the effect of interfacial dipoles, in the form of differently *p*-subtituted benzoic acids (Figure 1.18), on the performance of bilayer TiO$_2$-P3HT hybrid solar cells, Goh *et al.* concluded that V_{oc} correlates very well with the dipole magnitude.[43]

Indeed, dipoles pointing at TiO$_2$ decreased V_{oc} by as much as 0.2 V, whereas dipoles pointing away from TiO$_2$ only increased V_{oc} by at most 0.03-0.05 V. The small increment in V_{oc} with dipoles pointing away from titania is possibly due to the opposite dipole contribution given by the protonation effect of the carboxylic acid group.

Interestingly, the photocurrent, and hence the charge-transfer yield, in these devices showed an almost two-fold enhancement when using IMs with strong dipoles pointing toward TiO$_2$ suggesting that these particular monolayers might be able to mediate charge transfer from the polymer to the metal oxide. In conclusion, by utilizing the IMs, the PCE of the planar TiO$_2$-P3HT devices were raised from 0.34% to a maximum of 0.6%.

The use of small organic molecules with carboxylic groups that can be easily anchored to the oxide surface may help as well in increasing the compatibility between the polymer, having a hydrophobic nature, and the

39
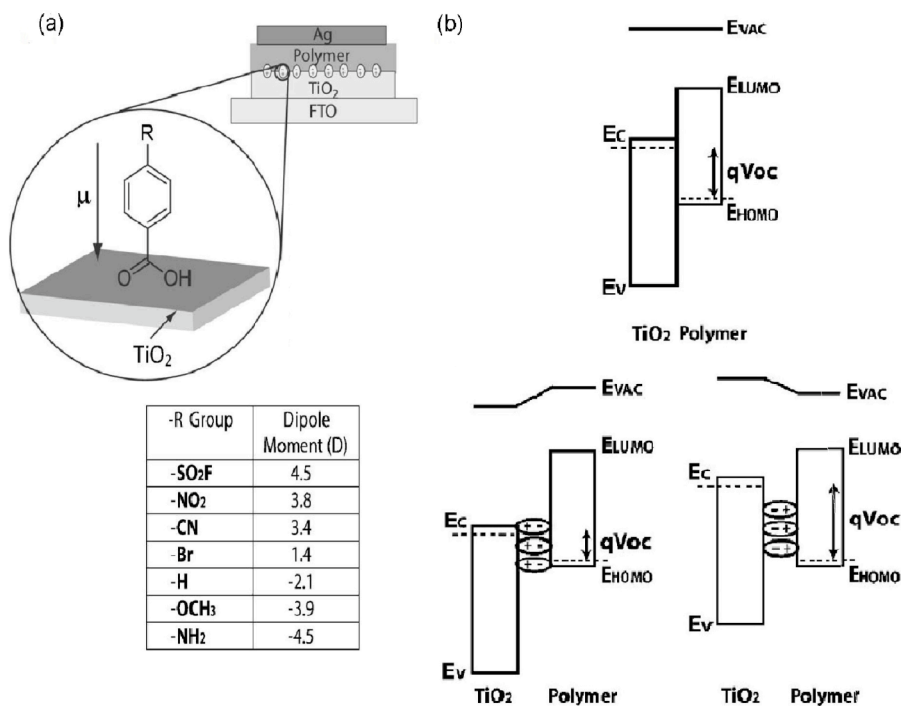
Figure 1.18. (a) Schematic of bilayer TiO$_2$-P3HT devices with dipolar modification of the titania surface. The table lists the substituent R- group on the *para* position of the benzoic acid accompanied by calculated dipole moments. (b) Effect of the interface modifiers on the energy offset and V_{oc} in the hybrid devices.

hydrophilic metal oxide. These modifications can assist charge separation, allowing an efficient transport of charge carriers between TiO$_2$ and the polymer. Using this approach, Freitas *et al.* investigated the use of carboxylated thiophene small molecules as interface modifiers in a nanoporous TiO$_2$-P3HT hybrid device (Figure 1.19).[44] They found that small differences in the chemical structure of these molecules, for example, the presence of the methylene group in 2-thiopheneacetic acid (TAA), can greatly increase the surface wettability, improving the TiO$_2$-P3HT contact. Unfortunately, they were not able to obtain devices with significant overall performances, the best results being obtained for the

μ = 8.39 D

HOOC...COOH

μ = 4.86 D

...COOH

S COOH

S

S ...COOH

TCA

TDA

TAA
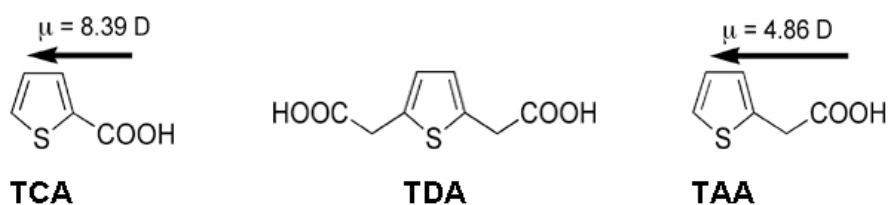
Figure 1.19. Chemical structures of 2-thiophenecarboxylic acid (TCA), 2-thiopheneacetic acid (TAA), 2,5-thiophenedicarboxylic acid (TDA) with indication of the corresponding dipole moment values.

TiO_2/TAA/P3HT modification, for which a modest J_{sc} of 0.26 mA cm^{-2} and V_{oc} of 0.21 V were obtained. Besides a lower photocurrent value of 0.13 mA cm^{-2} using the 2-thiophene-carboxylic acid (TCA) modification, a higher V_{oc} of 0.24 V was measured and this enhancement was attributed to the almost doubled magnitude of the dipole moment of TCA compared to TAA. In this example, as well as in the previous one, an increase in V_{oc} is consistent with dipoles directed away from the titania surface.

For crystalline polymers like P3HT the orientation of the polymer at the interface plays an important role in the charge generation process, since it influences the contact between the photoactive materials as well as local charge carrier mobilities. Canesi *et al.* showed that by inserting 4-mercaptopyridine (4-MP) molecules at the hybrid interface a face-on orientation of the P3HT chains on TiO_2 is achieved, which directly enhances the photocurrent contribution of the polymer (Figure 1.20).[45] When the 4-MP interlayer is added, the photocurrent is doubled, from 1.4 mA cm^{-2} to 3.26 mA cm^{-2}, together with an enhancement of the V_{oc} from 0.51 to 0.62 V, bringing the PCE to 0.95% from a value of about 0.4% in the TiO_2-P3HT device without interlayer. Further improvement is observed upon annealing, with an increase of the short-circuit photocurrent to 3.75 mA cm^{-2} and a rise of the efficiency to 1.13%, a

41
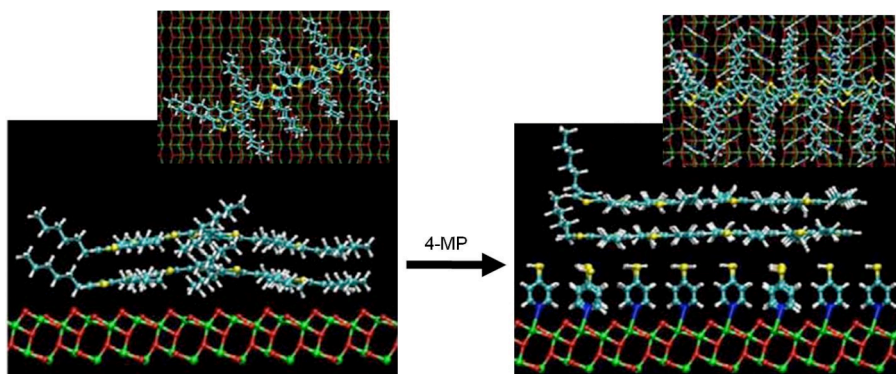
Figure 1.20. Atomistic simulation illustrating the ordering of P3HT chains on the TiO$_2$ surface after insertion of the 4-MP interfacial modifier.

remarkable value for this type of cell. Anyway, the quite low EQE measured for the nanoporous TiO$_2$/4-MP/P3HT device may indicate a still poor electronic coupling between the two active components at the interface and/or a trapping of the excitonic species which hampers their diffusion, thus anticipating that better engineering of the electronic wavefunction at the interface and the possibility to extend the level of order achieved at the interface to a longer range will further boost the device performance.

1.3.5 Solid-state DSSCs

In the aforementioned results about nanostructured metal oxide-IM-polymer hybrid solar cells, a negligible optical density of the interfacial modification layer compared to that of P3HT was observed. Therefore, the enhanced device performance mainly results from improved organic-inorganic interfaces, and not from an increased light harvesting of interfacial molecules. Nevertheless, dye molecules used for interface modification may also act as an additional photon absorber for further enhancing the light harvesting and photocurrent generation of charge carriers in nanostructured metal oxide-dye-polymer hybrid solar cells.

42

The new concept of nanostructured metal oxide-dye-polymer hybrid devices consists therefore of the mixed specific features of both polymer hybrid solar cells and solid state DSSCs. The conventional solid-state DSSC architecture combines metal oxide nanostructures and molecular dyes with an organic hole-transporting material such as spiro-OMeTAD, whereas the new device structure replaces the typical hole-transporting layer of spiro-OMeTAD (mobility of 10^{-5} to 10^{-4} cm^2 V^{-1} s^{-1}) with P3HT (mobility of 10^{-3} to 10^{-1} cm^2 V^{-1} s^{-1}), which exhibits a higher hole mobility and strong light absorption.[46] As mentioned before, in this type of nanostructured metal oxide-dye-polymer hybrid solar cell, both the polymer and the dye molecules may contribute to light harvesting to enhance the photocurrent. To increase the effective surface area for the adsorption of the dye molecules, a nanostructured metal oxide layer with a thickness of a few micrometers is used, which is a thickness greater than that of conventional nanostructured metal oxide-polymer hybrid solar cells (about 100-300 nm). The interfacial energetic band alignment is another important issue when adding dye molecules at the polymer-inorganic interfaces. If the lowest unoccupied molecular orbital (LUMO) in the dye molecule lies at a lower energy than the conjugated polymer, the electron transport is barrier-free from the LUMO level of the polymer to the conduction band (CB) of the inorganic nanostructure. Conversely, a dye possessing a lower highest occupied molecular orbital (HOMO) level compared to the conjugated polymer, let the polymer mainly function as the hole-transporter to regenerate the oxidized dye. The mechanisms of electron mediation and dye regeneration in a polymer-dye-metal oxide hybrid solar cell are represented schematically in Figure 1.21.
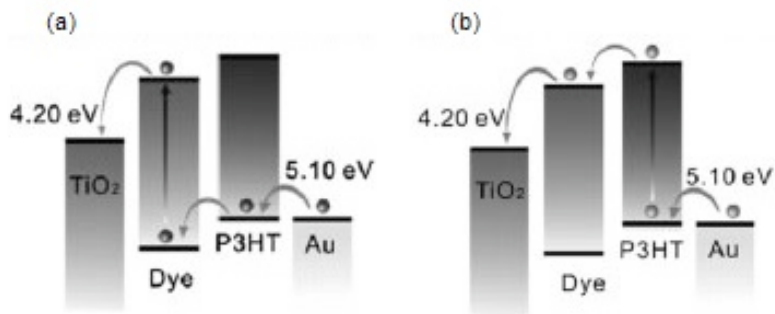
Figure 1.21. (a) Dye-regenerating and (b) electron-mediating mechanisms of the dye interface modifier in solid-state DSSCs.

An appropriate design in the dye molecular energy levels with respect to the polymer and metal oxide is thus crucial. Several groups have reported the use of different organic dyes to modify the surface of metal oxide nanostructures and enhance the light harvesting efficiency. Yu *et al.* designed a class of conjugated cyanoacrilic acids with different HOMO and LUMO levels to modify the interface between P3HT and nanoporous TiO_2.[47] By incorporating a strong electron-withdrawing –CN moiety adjacent to the –COOH anchoring group to produce a molecular dipole pointing away from the TiO_2 surface, both V_{oc} and J_{sc} can be increased simultaneously (Figure 1.22). Moreover, the LUMO of IMs can be fine-tuned by elongating the conjugation length or adopting a donor-acceptor structure, which systematically changes the EQEs of the devices. The LUMO levels of the IMs were found to decisively determine the dissociation efficiency of P3HT excitons. They showed an optimally performing device with a V_{oc} of 0.8 V, a J_{sc} of 6.79 mA cm^{-2} and an *FF* of 52.81%, yielding a PCE of 2.87% for the P3HT-WL-4-TiO_2 device structure. As an alternative to direct charge transfer, the photocurrent contribution of the polymer can also be activated via an energy transfer from the polymer to the sensitizer. Upon photon absorption in the

44
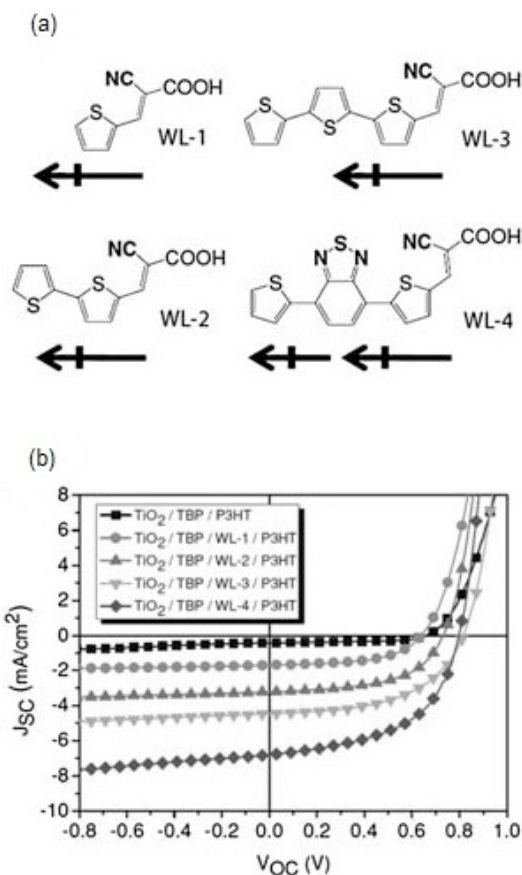
Figure 1.22. (a) Chemical structures of various conjugated cyanoacrylic acids and (b) corresponding current-voltage characteristics of P3HT-porous TiO_2 hybrid solar cells using the different cyanoacrylic acids as interface modifiers.

polymer the excitation energy can thus migrate to the dye, followed by electron injection into the metal oxide and hole transfer to the polymer. Such a mechanism has been proposed for a combination of P3HT with a porphyrin dye, which allows outstandingly high short circuit current densities beyond 12 mA cm^{-2}, four times more than with a transparent hole transporter.[48]

Similarly to all-organic bulk heterojunction devices, also in hybrid solar cells low band-gap organic dyes or polymers have been studied, for

45

efficiently harvesting visible to NIR solar radiation. Mor *et al.* reported a nanostructured inorganic-organic hybrid solar cell where electron-transporting TiO_2 nanotube arrays, sensitized with an unsymmetrical squaraine dye (SQ-1) that absorb in the red and NIR portion of the solar spectrum, are combined with hole-transporting and visible light-absorbing regioregular P3HT.[49] The absorption bands of the SQ-1 dye and P3HT complement each other, making the two materials appropriate for an extended spectrum solar cell, in which the dye molecules are anchored to the nanotube walls and the P3HT is within the nanotubes (Figure 1.23). Indeed, when both the polymer and the dye contribute to light harvesting, a large overlap in the absorption spectra of the two components should be avoided. Consequently, the TiO_2 nanotube array-P3HT hybrid solar cell modified with the organic SQ-1 dye layer exhibits a significant enhancement of the PCE, from 0.34% (no organic dye) to 3.8% and a V_{oc} of 0.6 V, a J_{sc} of 11 mA cm^{-2} and an FF of 0.58. The EQE spectrum was over 60% in the visible region and extended to the NIR region because of the photocurrent contribution from the SQ-1 dye molecules.

Grancini *et al.* recently demonstrated a hybrid polymer-metal oxide solar cell by incorporating a low band-gap polymer PCPDTBT to porous TiO_2 nanostructures.[50] By further co-functionalizing the TiO_2 surface with a self-assembled monolayer of a fullerene derivative containing a carboxylic acid terminated anchoring group (C_{60}-SAM),an indolene based organic dye-sensitizer (D131) and a lithium salt (Li-TFSI), a panchromatic spectral photo-response can be achieved in the visible to
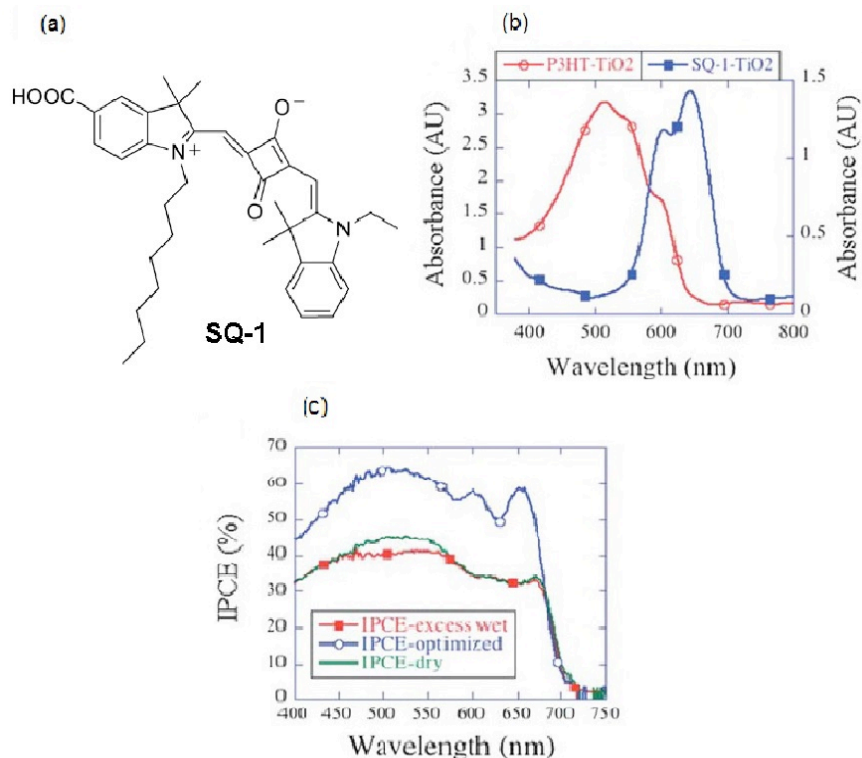
Figure 1.23. (a) Chemical structure of the SQ-1 dye. (b) Absorption spectra of the P3HT-TiO$_2$ and SQ-1-TiO$_2$ hybrid. (c) EQE spectra of the corresponding devices, where visible and NIR portions were contributed by P3HT and SQ-1 dye respectively.

NIR region, causing the EQE spectrum to extend to 900 nm, with the device delivering over 30% EQE from the light absorbed in the NIR region by the low band-gap polymer PCPDTBT (Figure 1.24). The authors concluded that electron transfer is the main limitation to device performance in polymer absorber based hybrid solar cells. The functionalization of the mesoporous oxide surface with a fullerene electron acceptor, which acts as intermediary species, electronically coupling the semiconducting polymer to the metal oxide, was a first step to overcome this limitation. Additionally, by tuning the surface potential

47
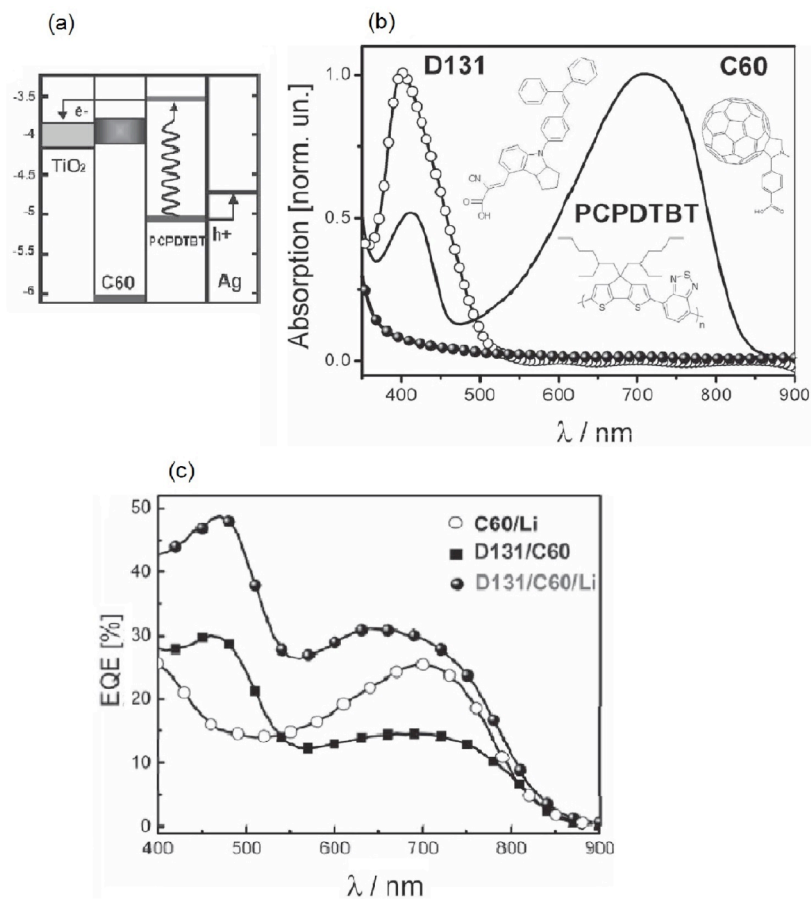
Figure 1.24. (a) Energy band alignment of C60-modified mesoporous TiO$_2$ and low band gap polymer PCPDTBT hybrid solar cell. The corresponding absorption spectra are shown in (b). (c) Panchromatic spectral photo-response with EQE spectra extended to 900 nm, which were contributed by the low band gap polymer PCPDTBT.

of the metal oxide with lithium salts, a further increase in photocurrent could be achieved.

As an alternative to the use of small-molecular dyes for the sensitization of mesoporous nanocrystalline TiO$_2$, Bhongale and Thelakkat employed the already reported P3HT-COOH polymer and subsequently spin-coated a layer of regioregular P3HT on the P3HT-COOH sensitized titania, followed by a layer of PEDOT:PSS before depositing the top metal

48

electrode.[51] By combining P3HT-COOH as sensitizer and regioregular P3HT as hole-transporting layer, light absorption in relatively thin solid state active layer was improved and a graded transport of holes towards the top electrode was guaranteed. On annealing at 150 °C for 10 min prior to gold electrode deposition, a PCE of 0.79% was obtained for the hybrid photovoltaic device.

Finally, it should be mentioned that, in a comparative study, Weickert *et al.* systematically investigated the influence of different TiO_2 surface modifiers on the performance of planar, bilayered TiO_2-P3HT devices, with the aim of inferring design rules and guidelines for interfaces in hybrid solar cells. Bare TiO_2 was compared to TiO_2 modified with the Ru(II) dye Z907, with phenyl-C_{61}-butyric acid (PCBA), a fullerene derivative bearing a carboxylic acid substituent to promote binding to the titania surface (Figure 1.25) and with the carboxylated polymer P3HT-COOH respectively.[52]
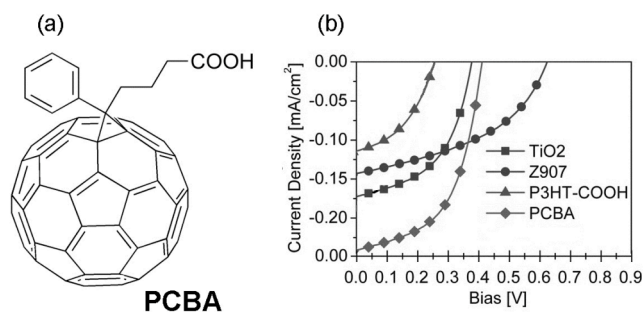
Figure 1.25. (a) Chemical structure of phenyl-C_{61}-butyric acid (PCBA). (b) *J-V* characteristics of planar P3HT-TiO_2 bilayered devices with different interface modifications.

Self-assembled monolayers were investigated for the three modifiers, in order to obtain a negligible light absorption from the modifiers, resulting in P3HT being the main absorber in the systems. Even though P3HT-

49

COOH, as reported previously, shows great promise in bulk-heterojunction hybrid solar cells, for the cell design employed here, the P3HT-COOH layer resulted detrimental. The carboxylated polymer causes deterioration in device performance, most likely because of non-homogeneous coating of the planar TiO_2 surface. P3HT-COOH appears in fact to arrange in coil structures, which act as charge traps slowing charge extraction and fastening charge recombination. Besides, the low order of P3HT-COOH might induce low order of the adjacent P3HT layers in turn. The highest efficiencies were realized with Z907 and PCBA. Whereas the former allows high V_{oc} but lower photocurrents, due to its alkyl chains, which slow down charge recombination but also hinder charge extraction, the latter cannot compete with Z907 on device V_{oc} but significantly slows down recombination compared to bare TiO_2. Moreover, the highest photocurrent was obtained with PCBA, because of fullerene outstanding properties as an electron acceptor, allowing cascade charge transfer from the polymer to the metal oxide.

Although these types of solar cells may not be categorized as conventional polymer-metal oxide hybrid solar cells, the role of the polymer appears crucial for achieving high-performance power conversion efficiencies and, given the huge amount of research devoted to the field, there is a great potential that optimized dye-polymer combination will be found, allowing efficiencies exceeding 10%.[53]

Overview of Chapters 2-4 of this thesis

As already mentioned thoroughly in the previous literature overview, one of the main limitations of hybrid photovoltaic architectures is constituted by the scarce affinity between the two main components, *i.e.* the conjugated polymer and the metal oxide semiconductor. The two

materials have indeed highly different natures, being the former hydrophobic and the latter hydrophilic. It is reasonable therefore to attempt the enhancement of their mutual compatibility in order to improve device performance. Within this contest, the research focus of the following three chapters of this thesis has been directed towards the introduction of suitable functionalities on the organic counterpart of the hybrid device aimed at addressing specific interactions with the inorganic matrix.

These modifications may regard the polymeric material itself or may be inserted in the form of thin layers of small molecular materials disposed at the interface between the polymer and the metal oxide (Figure 1.26).

Before starting with these investigations, it was judged worth to carry out a preliminary study about the effect of structural variations in the conjugated polymer chains on their ability to infiltrate into a nanoporous metal oxide scaffold, which will be the subject of Chapter 2.

Relying on these premises, the strategies adopted for the chemical functionalization of the most extensively employed conjugated material in OPV and HPV, *i.e.* poly(3-hexylthiophene), will be first described, together with the results obtained from applying the modified polymer as an active component in nanostructured TiO_2-polymer hybrid solar cells (Chapter 3). In second instance, the alternative use of functionalized oligothiophenes as interfacial modifiers in the same type of devices will be reported.
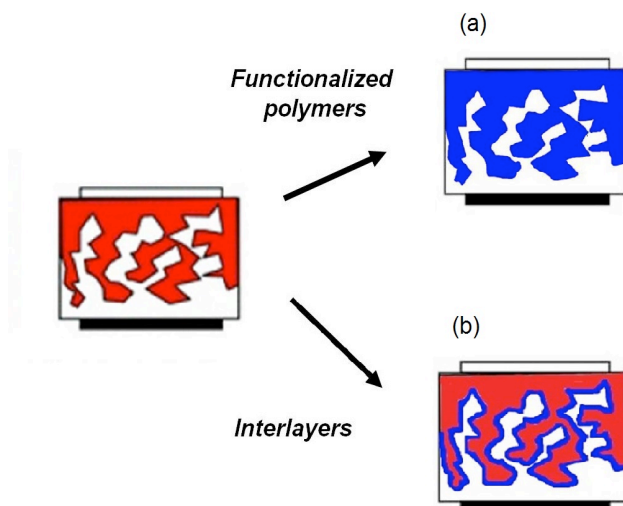
Figure 1.26. Strategies to increase the mutua compatibility between the two main components in nanostructured hybrid polymer/metal oxide solar cells. (a) Use of a functionalized polymer. (b) Use of a molecular interlayer.

References

[1] (a) O'Regan, B.; Grätzel, M. *Nature*, **1991**, *353*, 737. (b) Hagfeldt, A.; Boschloo, G.; Sun, L.; Kloo, L.; Pettersson, H. *Chem. Rev.*, **2010**, *110*, 6595–6663.

[2] Forrest, S.R. *Nature*, **2004**, *428*, 911.

[3] For recent review, see: (a) Bouclé, J.; Ravirajan P.; Nelson, J. *J. Mater. Chem.*, **2007**, *17*, 3141-3153. (b) Gao, F.; Ren, S.; Wang, J. *Energy Environ. Sci.*, **2013**, *6*, 2020-2040. (c) Fan, X.; Zhang, M.; Wang, X.; Yang, F.; Meng, X. *J. Mater. Chem. A*, **2013**, *1*, 8694-8709. (d) Li, S.S., Chen, C.W. *J. Mater. Chem. A*, **2013**, *1*, 10574-10591. (e) Bouclé, J.; Ackermann, J. *Polym. Int.*, **2012**, *61*, 355-373.

[4] (a) Lin, Y.Y.; Chu, T.H.; Li, S.S.; Chuang, C.H.; Chang, C.H.; Su, C.P.; Chang, C.P.; Chu, M.W.; Chen, C.W. *J. Am. Chem. Soc.,* **2009**, *131*, 3644-3649. (b) Dayal, S.; Kopidakis, N.; Olson, D.C., Ginley, D.S., Rumbles, G. *Nano Lett.*, **2009**, *10*, 239-242. (c) Kumar, S.; Nann, T. *J. Mater. Res.*, **2004**, *19*, 1990-1994. (d) Liu, C.Y.; Holman, Z.C.; Kortshagen, U.R. *Nano Lett.*, **2008**, *9*, 449-452. (e) Günes, S.; Fritz, K.P.; Neugebauer, H.; Sarifitci, N.S.; Kumar, S.; Scholes, G.D. *Sol. Energy Mater. Sol. Cells*, **2007**, *91*, 420-423. (f) Oosterhout, S.D.; Wienk, M.M.; van Bavel, S.S.; Thiedmann, R.;

Koster, L.J.A.; Gilot, J.; Loos, J.; Schmidt, V.; Janssen, R.A. *Nat. Mater.*, **2009**, *8*, 818-824.

[5] Osterloh, F.E. *Chem. Mater.* **2008**, *20*, 35-54.

[6] Rock, F.; Barsan, N.; Weimar, U. *Chem. Rev.*, **2008**, *108*, 705-725.

[7] Vlachopoulos, N.; Liska, P.; Augustynski, J.; Grätzel, M. *J. Am. Chem. Soc.*, **1988**, *110*, 1216.

[8] Sariciftci, N.S.; Braun, D.; Zhang, C.; Srdanov, V.I.; Heeger, A.J.; Stucky, G.; Wudl, F. *Appl. Phys. Lett.*, **1993**, *62*, 585.

[9] (a) Savenije, T.J.; Warman, J.M; Goossens, A. *Chem. Phys. Lett.*, **1998**, *287*, 148. (b) Van Hal, P.A.; Christiaans, M.P.T.; Wienk, M.M.; Kroon, J.M.; Janssen, R.A. *J.Phys.Chem. B*, **1999**, *103*, 4352. (c) Arango, A.C.; Carter, S.A.; Brock, P.J. *Appl. Phys. Lett.*, **1999**, *74*, 1698. (d) Anderson, N.A.; Hao, E.C.; Ai, X.; Hastings, G.; Lian, T.Q. *Chem. Phys. Lett.*, **2001**, *347*, 304.

[10] (a) Zhou, Y., Eck, M., Krüger, M. *Energy Environ. Sci.*, **2010**, *3*, 1851-1864. (b) Helgesen, M.; Sondergaard, R.; Krebs, F. C. *J. Mater. Chem.*, **2010**, *20*, 36-60. (c) Skompska, M. *Synth. Met.*, **2010**, *160*, 1-15.

[11] (a) Zhou, Y.; Eck, M.; Veit, C.; Zimmermann, B.; Rauscher, F.; Niyamakom, P.; Yilmaz, S.; Dumsch, I.; Allard, S.; Scherf, U. *Sol. Energy Mater. Sol. Cells*, **2011**, *95*, 1232-1237. (b) Beek, W.J.; Slooff, L.H.; Wienk, M.M.; Kroon, J.M.; Janssen, R.A. *Adv. Fun. Mater.*, **2005**, *15*, 1703-1707.

[12] Wu, Y.; Zhang, G. *Nano Lett.*, **2010**, *10*, 1628-1631.

[13] Sun, B.; Snaith, H.J.; Dhoot, A.S.; Westenhoff, S.; Greenham, N.C. *J. Appl. Phys.*, **2005**, *97*, 014914.

[14] (a) Arango, A.C.; Johnson, L.R.; Bliznyuk, V.N.; Schlesinger, Z.; Carter, S.A.; Horhold, H.H. *Adv. Mater.*, **2000**, *12*, 1689. (b) Salafsky, J.S. *Phys. Rev. B*, **1999**, *59*, 10885.

[15] Ravirajan, P.; Haque, S.A.; Durrant, J.R.; Poplavskyy, D.; Bradley, D.D.C.; Nelson, J. *J. Appl. Phys.*, **2005**, *15*, 609-618.

[16] (a) Ma, W.; Yang, C.; Gong, X.; Lee, K.; Heeger, A.J. *Adv. Funct. Mater.*, **2005**, *15*, 1617-1622. (b) Li, G.; Yao, Y.; Yang, H.; Shrotriya, V.; Yang, G.; Yang, Y. *Adv. Funct. Mater.*, **2007**, *17*, 1636-1644. (c) Lee, J.K.; Ma, W.L.; Brabec, C.J.; Yuen, J.; Moon, J.S.; Kim, J.Y.; Lee, K.; Bazan, G.C.; Heeger, A.J. *J. Am. Chem. Soc.*, **2008**, *130*, 3619-3623. (d) Lin, C.C.; Lin, Y.Y.; Li, S.S.; Yu, C.C.; Huang, C.L.; Lee, S.H.; Du, C.H.; Lee, J.J.; Chen, H.L.; Chen, C.W. *Energy Environ. Sci.*, **2011**, *4*, 2134-2139.

[17] Bouclé, J.; Chyla, S.; Shaffer, M.S.P.; Durrant, J.R.; Bradley, D.D.C.; Nelson, J. *Adv. Funct. Mater.*, **2008**, *18*, 622-633.

[18] Lin, Y.Y.; Chu, T.H.; Chen, C.W.; Su, W.F. *J. Appl. Phys.*, **2004**, *95*, 1473.

[19] Kwong, C.Y.; Djurisic, A.B.; Chui, P.C.; Chui, P.C.; Cheng, K.W.; Chan, W.K. *Chem. Phys. Lett.*, **2004**, *384*, 372-375.

[20] Chuang, C.H.; Lin, Y.Y.; Tseng, Y.H.; Chu, T.H.; Lin, C.C.; Su, W.F.; Chen, C.W. *J. Phys. Chem. C*, **2010**, *114*, 18717-18724.

[21] Moet, D.J.; Koster, L.J.A.; de Boer, B.; Blom, P.W. *Chem. Mater.*, **2007**, *19*, 5856-5861.

[22] Li, S.S.; Chang, C.P.; Lin, C.C.; Lin, Y.Y.; Chang, C.H.; Yang, J.R.; Chu, M.W.; Chen, C.W. *J. Am. Chem. Soc.*, **2011**, *133*, 11614-11620.

[23] Lin, Y.Y.; Chu, T.H.; Chen, C.W.; Su, W.F. *Appl. Phys. Lett.*, **2008**, *92*, 053312.

[24] Huang, Y.C.; Hsu, J.H.; Liao, Y.C.; Yen, W.C.; Li, S.S.; Lin, S.T.; Chen, C.W.; Su, W.F. *J. Mater. Chem.*, **2011**, *21*, 4450-4456.

[25] Oosterhout, S.D.; Koster, L.J.A.; van Bavel, S.S, Loos, J.; Stenzel, O.; Thiedmann, R.; Schmidt, V.; Campo, B.; Cleij, T.J.; Lutzen, L.; Vanderzande, D.; Wienk, M.M.; Janssen, R.A.J. *Adv. Energy Mater.*, **2011**, *1*, 90-96.

[26] Redeker, N.D.; Danesh, C.D.; Ding, Y.; Zhang, S. *Polymer*, **2013**, *54*, 7004-7008.

[27] Lin, Y.; Wei, Q.; Qian, G.; Yao, L.; Watkins, J.J. *Macromolecules*, **2009**, *42*, 2581-2586.

[28] Bartholomew, G.P.; Heeger, A.J. *Adv. Funct. Mater.*, **2005**, *15*, 677-682

[29] Coackley, K.M.; Liu, Y.; McGehee, M.D.; Frindell, K.L.; Stucky, G.D. *Adv. Funct. Mater.* **2003**, *13*, 301-306.

[30] Abrusci, A.; Ding, I.K.; Al-Hashimi, M; Segal-Peretz, T.; McGehee, M.D.; Heeney, M.; Frey, G.L.; Snaith, H.J. *Energy Environ. Sci.*, **2011**, *4*, 3051-3058.

[31] Barbé, C.J.; Arendse, F.; Comte, P.; Jirousek, M.; Lenzmann, F.; Shklover, V. *J. Am. Ceram. Soc.*, **1997**, *80*, 3157-3171.

[32] Ravirajan, P.; Peiró, A.M.; Nazeeruddin, M.K.; Graetzel, M.; Bradley, D.D.; Durrant, J.R.; Nelson, J. *J. Phys. Chem. B*, **2006**, *110*, 7635-7639.

[33] Tepavcevic, S.; Darling, S.B.; Dimitrijevic, N.M.; Rajh, T.; Sibener, S.J. *Small*, **2009**, *5*, 1776-1783.

[34] Olson, D.C.; Shaheen, S.E.; Collins, R.T.; Ginley, D.S. *J. Phys. Chem. C*, **2007**, *111*, 16670-16678.

[35] Sung, Y.H.; Liao, W.P.; Chen, D.W.; Wu, C.T.; Chang, G.J.; Wu, J.J. *Adv. Funct. Mater.*, **2012**, *22*, 3808-3814.

[36] Di Fonzo, F.; Casari, C.S.; Russo, V.; Brunella, M.F.; Li Bassi, A.; Bottani, C.E. *Nanotechnology*, **2009**, *20*, 015604.

[37] Olson, D.C.; Shaheen, S.E.; Collins, R.T.; Ginley, D.S. *J. Phys. Chem. C*, **2007**, *111*, 16670-16678.

[38] Lee, Y.J.; Lloyd, M.T.; Olson, D.C.; Grubbs, R.K.; Lu, P.; Davis, R.J.; Voigt, J.A.; Hsu, J.W. *J. Phys. Chem. C*, **2009**, *113*, 15778-15782.

[39] Baeten, L.; Conings, B.; Boyen, H.G.; D'Haen, J.; Hardy, A.; D'Olieslaeger, M.; Manca, J.V.; Van Bael, M.K. *Adv. Mater.*, **2011**, *23*, 2802-2805.

[40] Wu, S.; Tai, Q.; Yan, F. *J. Phys. Chem. C*, **2010**, *114*, 6197-6200.

[41] Passoni, L.; Ghods, F.; Docampo, P.; Abrusci, A.; Martí-Rujas, J.; Ghidelli, M.; Divitini, G.; Ducati, C.; Binda, M.; Guarnera, S.; Li Bassi, A.; Casari, C.S.; Snaith, H.J.; Petrozza, A.; Di Fonzo, F. *ACS nano*, **2013**, *7*, 10023-10031.

[42] Lin, Y.Y.; Chen, C.W.; Chu, TH.; Su, W.F.; Lin, C.C.; Ku, C.H.; Wu, J.J.; Chen, C.H. *J. Mater. Chem.*, **2007**, *17*, 4571.

[43] Goh, C.; Scully, S.R.; McGehee, M.D. *J. Appl. Phys.*, **2007**, *101*, 114503.

[44] Freitas, F.S.; Clifford, J.N.; Palomares, E.; Nogueira, A.F. *Phys. Chem. Chem. Phys.*, **2012**, *14*, 11990-11993.

[45] Canesi, E.V.; Binda, M.; Abate, A.; Guarnera, S.; Moretti, L.; D'Innocenzo, V.; Kumar, R.S.S.; Bertarelli, C.; Abrusci, A.; Snaith, H.J.; Calloni, A.; Brambilla, A.; Ciccacci, F.; Aghion, S.; Moia, F.; Ferragut, R.; Melis, C.; Malloci, G.; Mattoni, A.; Lanzani, G.; Petrozza, A. *Energy Environ. Sci.*, **2012**, *5*, 9068-9076.

[46] Poplavskyy, D.; Nelson, J. *J. Appl. Phys.*, **2003**, *93*, 341-346.

[47] Yu, J.; Shen, T.L.; Weng, W.H.; Huang, Y.C.; Huang, C.I.; Su, W.F.; Rwei, S.P.; Ho, K.C.; Wang, L. *Adv. Energy Mater.*, **2012**, *2*, 245-252.

[48] Moon, S.J.; Baranoff, E.; Zakeeruddin, S.M.; Yeh, C.Y.; Guang Diau, E.W.; Gratzel, M.; Sivula, K. *Chem. Commun.*, **2011**, *47*, 8244.

[49] Mor, G.K.; Kim, S.; Paulose, M.; Varghese, O.K.; Shankar, K.; Basham, J.; Grimes, C.A. *Nano Lett.*, **2009**, *9*, 4250-4257.

[50] Grancini, G.; Kumar, R.S.S; Abrusci, A.; Yip, H.L.; Li, C.Z.; Jen, A.K.Y.; Lanzani, G.; Snaith, H.J. *Adv. Funct. Mater.*, **2012**, *22*, 2160-2166.

[51] Bhongale, C.J.; Thelakkat, M. *Sol. Energy Mater. Sol. Cells*, **2010**, *94*, 817-822.

[52] Weickert, J.; Auras, F.; Bein, T.; Schmidt-Mende, L. *J. Phys. Chem. C*, **2011**, *115*, 15081-15088.

[53] Weickert, J.; Schmidt-Mende, L. *APL Mater.*, **2013**, *1*, 020901.

CHAPTER 2

Polyterthiophenes Infiltration into Hierarchical TiO$_2$ Mesostructures

2.1 Introduction

The inability to effectively infiltrate semiconducting polymers into porous networks of metal oxide nanoparticles together with an ineffective charge transport within the polymer phase due to non-crystalline, un-orientated polymer chains are among the main issues thought to be responsible for the suboptimal operation of hybrid solar cells. Since polymers suffer a loss of conformational entropy when they are confined in a channel whose radius is less than the radius of gyration,[1] filling the pores with a polymer has been thought to be a challenge. Here a systematic study is reported, which demonstrates that a conjugated polymer can effectively penetrate a mesoporous TiO_2 film for its entire depth (2 μm), generating a uniform thin film onto the entire internal surface of the metal oxide scaffold. As already discussed in Chapter 1, many other related studies are reported in recent literature,[2] being the subject a "hot" topic in solar cell research.

Whit respect to previous works, for the present investigation it was chosen to make use of active materials having some structural differences with respect to the commonly used poly-(3-hexylthiophene) and standard nanocrystalline titanium dioxide paste. These modifications are aimed at giving an original contribution to the theme of conjugated polymer infiltration into nanoporous inorganic semiconductor networks.

Poly(3,3''-dihexyl-2,2':5',2''-terthiophene) (**PHTT**), which is an intrinsically regiosymmetric structural analogue of P3HT, being obtained by oxidative polymerization of the symmetrical monomer 3,3''-dihexyl-2,2':5',2''-terthiophene, was used.[3] To highlight possible effect on infiltration, two other polymers have been considered, with different length of the alkyl-side chains and molecular weight, namely poly(3,3''-didodecyl-2,2':5',2''-terthiophenes) with, respectively, a molecular

58

weight almost equal to **PHTT** (**PDTT-1**) and a molecular weight more than doubled with respect to **PHTT** (**PDTT-2**) (Figure 2.1).[4]

R=C_6H_{13}, M_n=12000, M_w=24000 **PHTT**

R=$C_{12}H_{25}$, M_n=14000, M_w=25000 **PDTT-1**

R=$C_{12}H_{25}$, M_n=27000, M_w=58000 **PDTT-2**
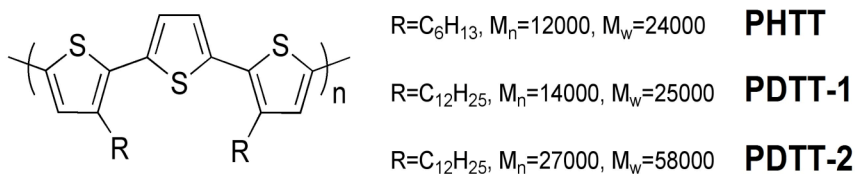
Figure 2.1. Chemical structure of the poly(3,3''-dialkyl-2,2':5',2''-terthiophene) polymers selected for the present study.

The poly(3,3''-dialkylterthiophenes) (PTTs) are perfectly regioregular polymers, with a more pronounced tendency to self-assemble at the solid state with respect to regioregular poly(3-alkylthiophenes) (PATs).[3a] The centrosymmetric repeating unit, with an unsubstituted central thiophene ring allows very regular spacing of the alkyl chains, resulting in a high degree of interdigitization within each polymer layer. A highly crystalline morphology is obtained, with good overlap of the π-conjugated system along the length of the backbone. This conformation has small cofacial distances (about 3.8 Å), giving rise to efficient charge carrier hopping. PTTs show also further advantages with respect to PTs: they are characterized by a lower lying HOMO orbital, which makes higher the oxidation potential and enhances their stability to the environment. Moreover, the electron affinity is also higher, suggesting better matching with the conduction band of TiO_2 (Figure 2.2).

59
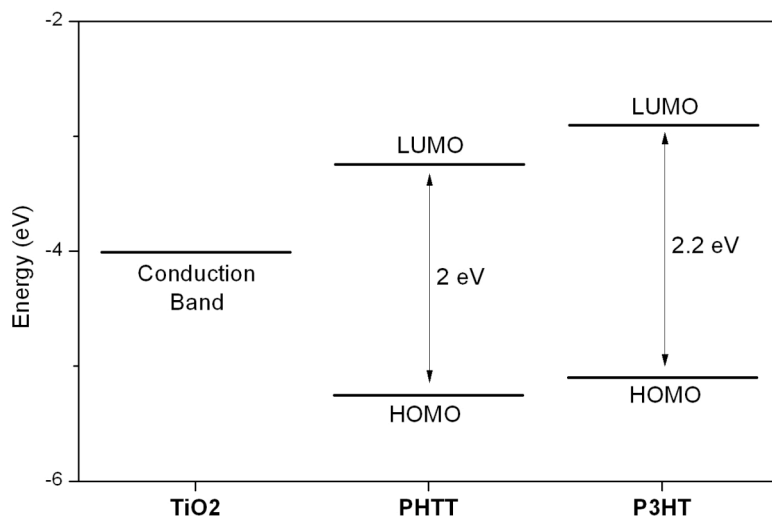
Figure 2.2. Energy levels diagram for nanocrystalline TiO_2, P3HT and **PHTT** polymers.

As for the inorganic semiconductor, the widely used mesoporous films made of nanocrystalline anatase TiO_2 particles were replaced by hierarchical assemblies of anatase particles, morphologically resembling a tree and giving rise to a forest-like architecture. The trees are directly grown on compact-TiO_2 coated, fluorine-doped tin oxide, by PLD in the laboratory of Prof. C.E. Bottani at the Energy Department of Politecnico di Milano (Dr. Ing. F. Di Fonzo).[5] By changing deposition conditions, *i.e.* the time and the oxygen pressure inside the chamber, different film densities and thicknesses can be obtained respectively (Figure 2.3); for the present study, 2 µm thick films, with a porosity of around 79% and a surface area of 86 m^2 g^{-1} were employed (O_2 pressure = 40 Pa). This nanomorphology has been demonstrated beneficial to enhance the electron diffusion length and to hamper electron recombination in DSSCs with solvent-free ionic liquid electrolyte[6] as well as to improve light harvesting in ssDSSCs.[7]
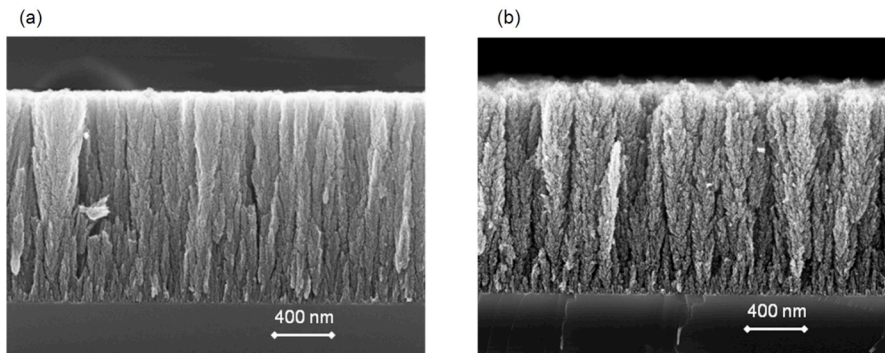
Figure 2.3. SEM images of the cross sections of PLD TiO_2 films deposited at (a) 20 Pa and (b) 40 Pa oxygen pressure.

2.2 Results and discussion

2.2.1 Polyterthiophenes infiltration into PLD TiO₂ mesoporous films

In analogy to the dye-sensitization process of inorganic photoanodes used for DSSCs, in which the metal oxide films are directly immersed in organic solutions of the dye,[8] the dipping technique was selected for the infiltration of PTTs into the PLD TiO_2 substrates. The metal oxide substrates were therefore immersed in a polymer solution for variable amounts of time. In this way, the contact time between the two materials can be made notably longer than with other deposition methods.[2a,9] Chloroform has been selected as the best solvent for the experiments, being capable of dissolving properly all the polymers here tested and having a relatively low polarity, which is a key requirement for preserving the nano-porous structure of the metal oxide scaffold, which has been shown to bunch when treated with polar solvents.[5] The metal oxide samples have been analyzed after polymer infiltration with scanning electron microscopy in order to evidence the resulting morphology at the nanoscale, again in the laboratory of Prof. C.E.

61

Bottani at Politecnico di Milano (Dr. Ing. F. Di Fonzo). It is evident from the SEM image reported in Figure 2.4a that the dipping technique allows a good deposition of the polymeric material inside the titania substrate without causing any damage to the nanostructure.
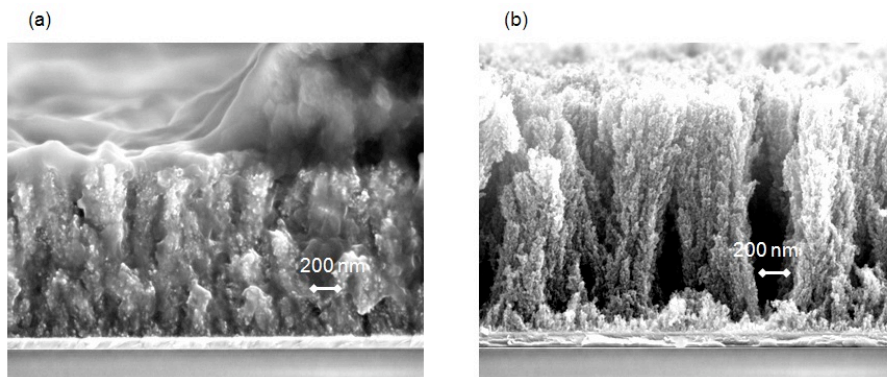
Figure 2.4. SEM images of nanostructured PLD TiO_2 (2 μm, 40 Pa) infiltrated with **PHTT** through the dipping technique (a) before and (b) after rinsing with chloroform.

From the images it also appears that the polymer is effectively able to penetrate deeply the mesoscale nanoporosity of the metal oxide, but also that a part remains on the surface, as a capping layer. Unfortunately, such an excess of polymer lies at a distance from the hybrid interface, which is higher than the exciton diffusion length and therefore does most likely not contribute to photocurrent generation in possible photovoltaic devices. Anyway it could still act as the hole-conducting layer, if the polymeric material results in a crystalline state, and as EBL. By washing the substrates with the same solvent used for dipping in the polymer solution, the capping layer is completely removed and the washed samples appear very similar to the TiO_2 film before polymer treatment, somehow as the removal of the organic material was total (Figure 2.4b). However the samples maintained a red color, as can be seen from the

62

picture reported in Figure 2.5, thus indicating that polythiophenes still remains infiltrated in the mesoporous structure.
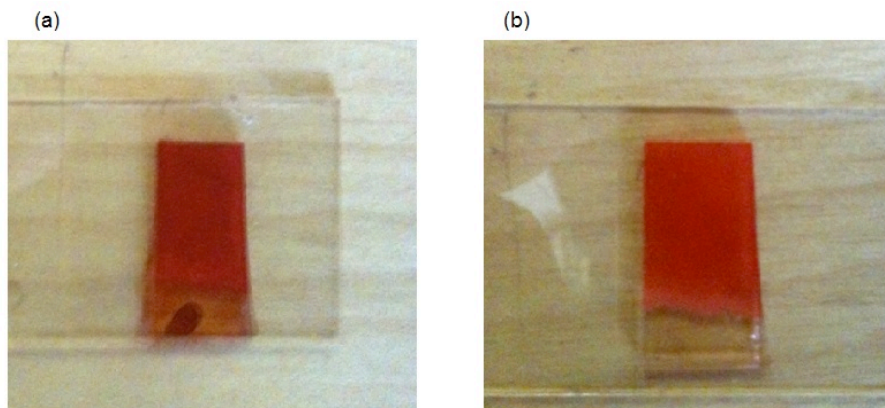
Figure 2.5. PLD TiO$_2$ samples infiltrated with **PHTT** through dipping (a) before and (b) after rinsing with chloroform.

It is then possible to assert that the thickness of the polyterthiophene layer obtained after the dipping-rinsing process and by which the titania nano-trees appear to be homogeneously surrounded, is lower than the sensitivity of the SEM and, therefore, on the order of magnitude of the exciton diffusion length. It appears anyway that such a thin layer is capable of absorbing a significant quantity of visible light (see the Experimental section 2.4 for details about the absorption measurements), thanks to the high surface area of the TiO$_2$ scaffold at which it tightly adheres, a condition of potential high efficiency in photovoltaic devices.

An increase in the quantity of photons absorbed by the active layer might be obtained by optimizing the deposition parameters, *i.e.* the immersion time and the concentration of the polymer solution. A systematic study has been performed with only one of the three analogous polymers selected for the present study, *i.e.* the **PHTT** derivative. The best

parameters determined for this model have been subsequently applied to the other two derivatives, in order to obtain a direct comparison. Using UV-vis absorption measurements, it is possible to evidence that higher amounts of polymer penetrate into the metal oxide scaffolds while increasing immersion times and polymer solution concentrations, indicating that both parameters have a significant influence on infiltration. As appears from Figure 2.6, low concentrations (1 mg ml^{-1}) and short immersion times (5 h) allow a maximum light absorption beyond 40% and, also after longer times (18 h), not overcoming 50%.
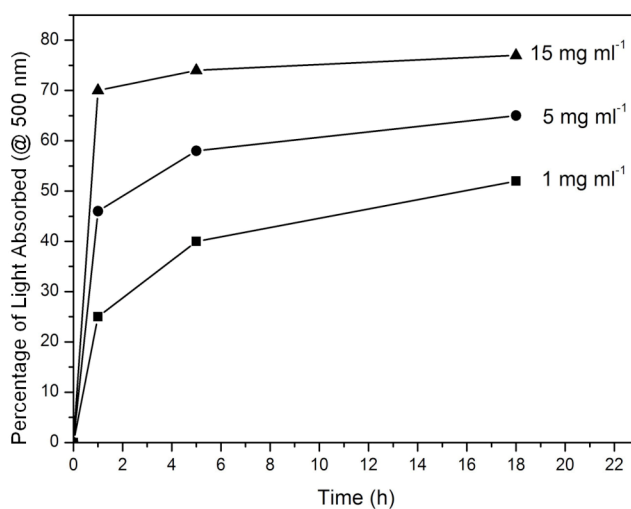
Figure 2.6. Percentage of light absorbed by **PHTT** embedded in a 2 μm PLD-TiO$_2$ film after dipping for various amounts of time in chloroform solutions having the indicated polymer concentrations and subsequent rinsing with chloroform.

Anyway faster rates of infiltration are gained by using more concentrated solutions: with a 5 mg ml^{-1} solution the percentage of light absorbed by the embedded polymer reaches 60% after only 1 h, whereas with a 15 mg ml^{-1} solution it increases until 75%. At all concentrations considered, light absorption is likely to reach saturation after 20 h of immersion. Of

64

course, for possible applications, it is necessary to find the right compromise between a good degree of light absorption and a short time for manufacturing the device active layer: for the present case therefore a 15 mg ml^{-1} concentration and 5 h immersion time were selected as the best conditions for further studies, that aimed at highlighting the effect of polymer structural variations on the infiltration.

Figure 2.7 illustrates that polymer infiltration into the nanostructured titania films is more effective for **PHTT** than for **PDTT**, indicating that the alkyl side-chains influence polymer adsorption on the metal oxide surface. The result is not surprising if the hydrophobic nature of the alkyl groups is considered in comparison with the hydrophilic nature of TiO$_2$ and further suggests that the interaction of the polymer with the inorganic substrate might take place by means of the thiophene moieties, being therefore compromised by the steric hindrance of the lateral substituents. Finally, it is also evident that a higher molecular weight causes further decrease in the amount of resulting polymer embedded into the metal oxide film. From the present data it is then possible to infer that polymers with shorter alkyl side-chains and lower molecular weights penetrate more easily the pores of the tree-like TiO$_2$ mesostructures. Nevertheless, an increase in molecular weight, which is generally required for better charge transport within polymer chains, does not cause a drastic decrease of the polymer infiltration and still allows a good degree of light absorption.

Percentage of Light Absorbed (@ 500 nm)

80
70
60
50
40
30
20
10
0

PHTT   PDTT-1   PDTT-2

Polymer
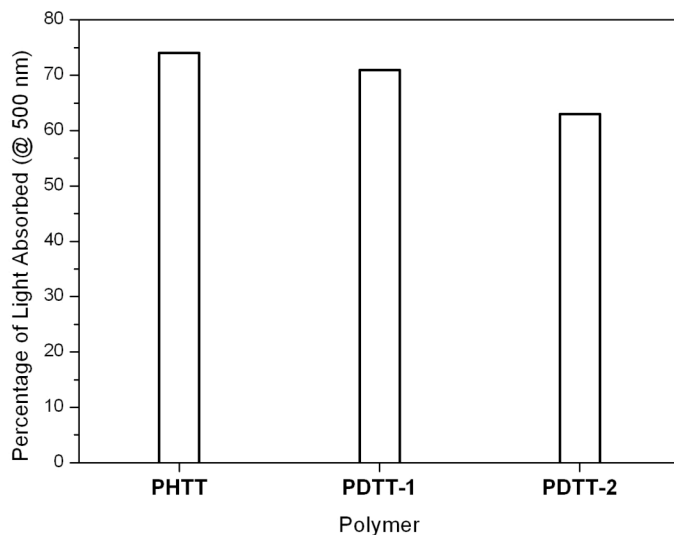
Figure 2.7. Percentage of light absorbed by the three different polyterthiophene derivatives selected for the present study embedded in 2 μm PLD-TiO$_2$ films after dipping for 5 h in 15 mg ml^{-1} chloroform solutions and subsequent rinsing with chloroform.

2.2.2 Characterization of the polyterthiophene infiltrated PLD TiO$_2$ mesoporous films

Non-destructive energy dispersive X-ray fluorescence microanalysis (EDXRF) performed with the SEM electron probe on the cross-section of a chloroform rinsed sample provided a first sign of effective polyterthiophene infiltration into the pores of the titania. Characteristic X-rays emitted by the atom constituents were probed laterally along the whole depth of the polymer-sensitized metal oxide films. Both titanium and sulfur are detected at almost constant concentrations from the "top" of the nano-trees down to the "roots" (Figure 2.8), the difference in the relative intensity of the signals being due to their different atomic weights and relative amounts in the film. Indium signal subsequently appears when probing the ITO glass substrate on which the TiO$_2$ films were grown.

66
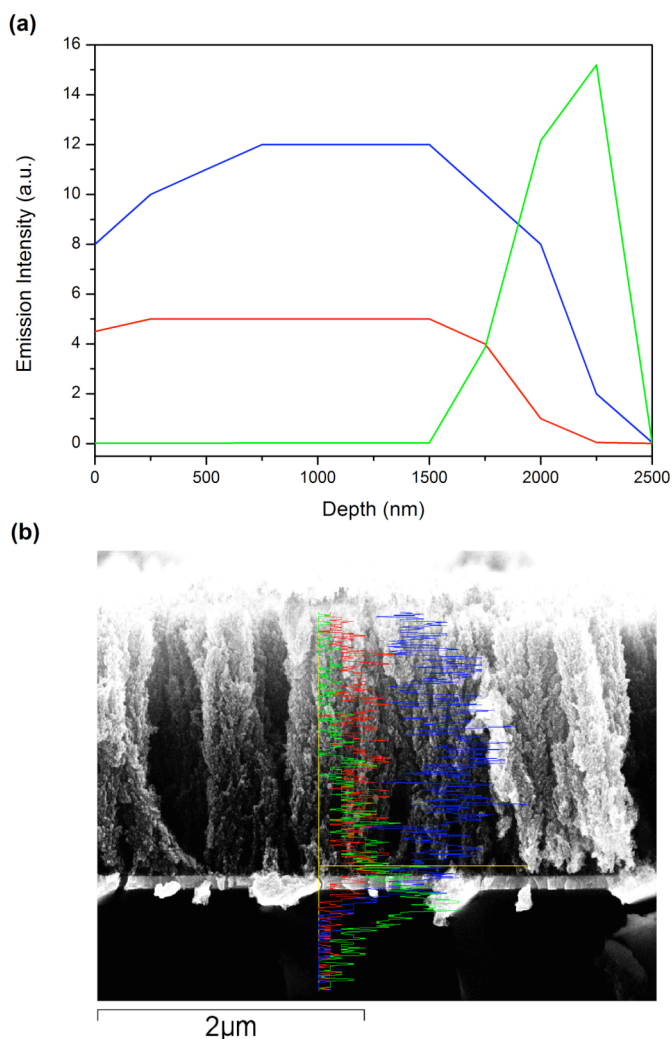
Figure 2.8. (a) EDXRF depth profiling traces for titanium Kα1 (blue line), sulfur Kα1 (red line) and indium Lα1 (green line) of a 2 μm PLD TiO$_2$ film after dipping-rinsing in a **PHTT** chloroform solution. (b) Sketch of the EDXRF depth profiling along the entire **PHTT** infiltrated PLD TiO$_2$ film.

Depth profiling was also performed for the first time on conjugated polymer-metal oxide hybrid film with the glow discharge optical emission technique (GDOES), which measures elemental concentrations in a sample while it is simultaneously sputtered away (therefore it is a

destructive method).[10] The measurement was carried out at the G. Natta department by Ing. M. F. Brunella. Figure 2.9 shows the results of the experiment for the titanium, sulfur and indium atoms.
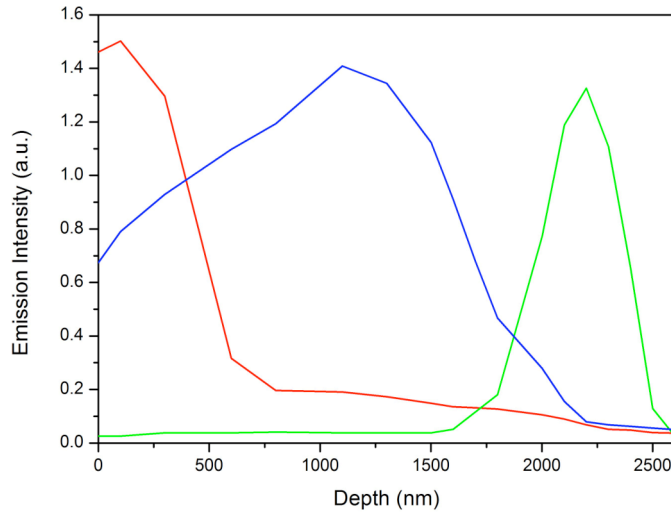
Figure 2.9. GDOES depth profiling traces for titanium (blue line), sulfur (red line) and indium (green line) of a 2 μm PLD TiO$_2$ film after dipping-rinsing in a **PHTT** chloroform solution.

A slightly different scenario arises in comparison with the previously discussed XRF microanalysis, resulting from the higher resolution of the GDOES technique. In fact, the sulfur signal appears quite intense in the first top layers of the sample and decreases significantly already at a depth of only 500 nm from the surface, to remain at low values until 2 μm, where it finally disappears completely. On the contrary the titanium signal steadily increases from the surface until 1.6 μm and then drastically decreases within 2 μm from the surface. At first sight it might be inferred that polymer infiltration is efficient for depths as far as only 500 nm. Anyway, by considering the particular tree-like structure of the metal oxide film, a different interpretation might arise, which better

68

explains the GD-OES data: the PLD film, in fact, present a minimum density of TiO$_2$ on the "top", where the polymer coating is instead prevalent, resulting in higher sulfur content with respect to titanium, whereas, after removal of these top layers, *i.e.* more deeply in the nanostructure, only a very thin polymer film remains in contact with a much more consistent amount of TiO$_2$, inverting the relative intensities of the two elemental signals (Figure 2.10).
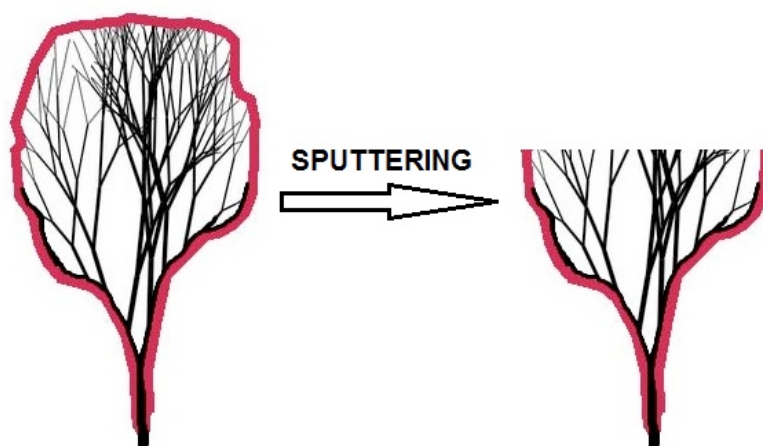
Figure 2.10. Schematic representation of the sputtering process involving the PHTT infiltrated PLD TiO$_2$ nanotrees. The sketch evidences the difference in polymer relative concentration on "top" of the nanotrees and deeply in the nanostructure.

Insight into the polymer chain conformation in the hybrid systems can be gleaned from the photoluminescence (PL) spectra of the embedded polymers after infiltration. PL can also be used to determine the degree of photoinduced charge transfer from the polymer to the metal oxide semiconductor. Figure 10 shows the PL spectra of **PHTT** embedded in mesoporous titania before and after rinsing the sample in chloroform and the PL spectrum of a **PHTT** film prepared by spin coating from a chloroform solution of the polymer on a glass substrate. The spectra

shown in Figure 2.11 were normalized by dividing the measured spectra by the relative absorptions at the excitation wavelength.
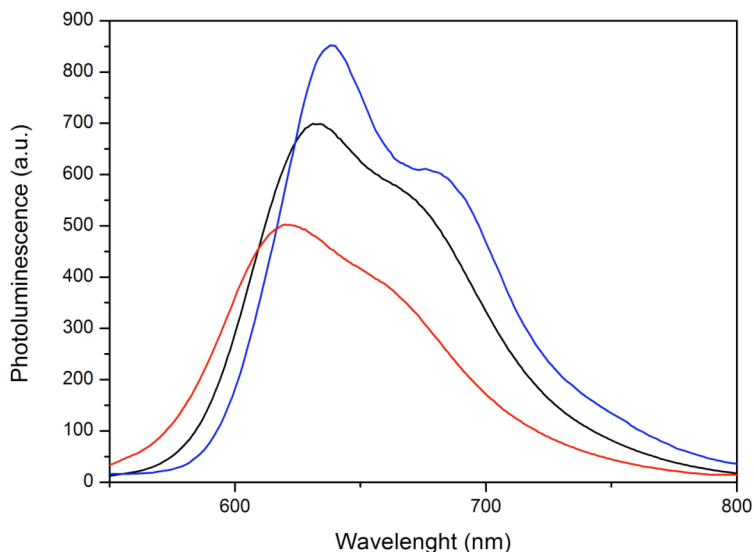
Figure 2.11. Photoluminescence spectra of **PHTT** infiltrated in a 2 μm PLD TiO2 film (5 h, 15 mg ml^{-1}) before (black line) and after (red line) rinsing with chloroform (λ_{exc} = 480 nm). For comparison the spectrum of a neat **PHTT** film is also reported (blue line).

The emission spectrum of the infiltrated **PHTT** results blue-shifted after chloroform washing, indicating a higher distorsion of the polymeric chains in the thin film surrounding the metal oxide with respect to the bulk polymer, *i.e.* the capping layer and the excess polymer inside the pores of the nanostructured TiO$_2$ film. One would expect a negligible amount of luminescence from such a thin polymer layer, since it is known that electron transfer usually occurs with very high efficiency if excitons are formed within 10-20 nm from the hybrid interface. Nonetheless, it is clear that some of the excitons are not able to migrate to the interface and donate an electron to the titania, even if they are formed in very close proximity. One possible reason for the incomplete quenching of the **PHTT** fluorescence can be found in the aforementioned

70

distortion of the polymer chains, which limits exciton diffusion to the interface, where the photoexcited electron can be then transferred to the inorganic acceptor.

From previous observations, the capping layer and the excess polymer filling the voids between the titania nanotrees appear not ideal for charge transport. Nonetheless, a proper annealing process could be helpful in inducing polymer crystallization and favor hole-transport across the capping layer toward the hole-collecting electrode.

The effective occurrence of an electron transfer process after light absorption at the polyterthiophene-nanostructured TiO_2 hybrid interface was investigated by means of ultrafast transient absorption (TA) spectroscopy, which evidences the presence of photo-excited charges in the conjugated polymer (Figure 2.12). The measurements were carried out at the Center for Nanoscience and Technology of the Italian Institute of Technology (CNST-IIT@Polimi) by Dr. S.S. Kumar and Dr. Ing. A. Petrozza. The positively charged species (polarons) present a characteristic absorption band in the TA spectrum, which appears at around 700 nm and whose formation and decay can be followed in time. Figure 2.13 shows the time-resolved TA spectrum for the PHTT infiltrated mesoporous TiO_2 film after 5 h dipping in a 15 mg ml^{-1} PHTT solution and subsequent rinsing in chloroform. The positive feature present in the spectrum at very short times (left side) is due to stimulated emission from the photoexcited polymer. The stimulated emission process is soon replaced by the occurrence of the photo-induced electron transfer from the polymer to the metal oxide, which is indicated by the negative feature appearing in the spectrum after 1.5 ps from light excitation. For comparison, the spectrum of a neat **PHTT** film obtained by spin-coating is also reported. The spectrum provides clear evidence
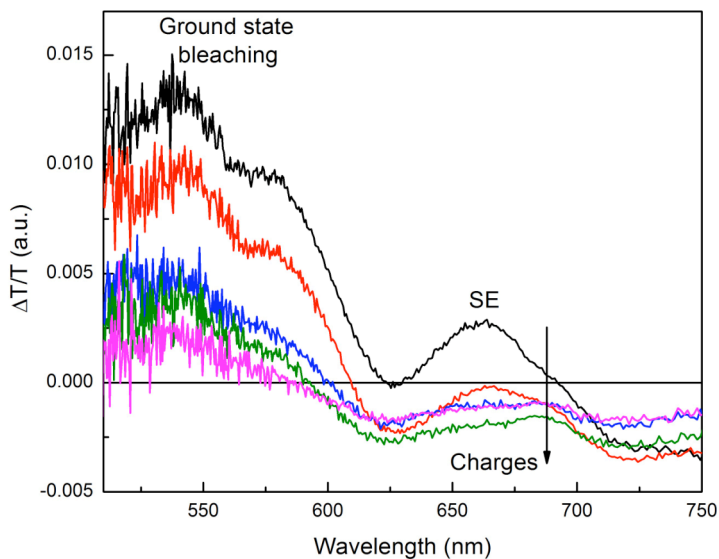
Figure 2.12. Transient absorption spectra of the **PHTT**-PLD TiO$_2$ hybrid junction obtained with the dipping-rinsing process (λ_{exc} = 530 nm, excitation power = 6 µJ cm^{-2}) at different times after photoexcitation: 0.3 ps (black line), 2 ps (red line), 8 ps (blue line), 50 ps (green line), 4 ns (magenta line).
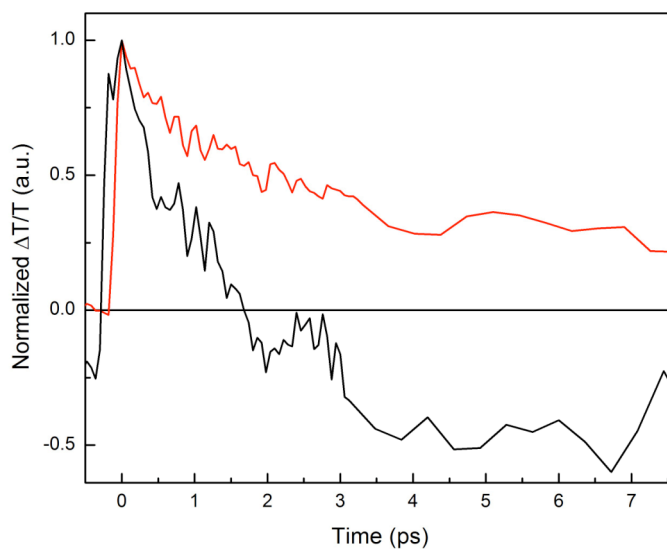
Figure 2.13. Time-resolved transient absorption spectra of the **PHTT**-PLD TiO$_2$ hybrid junction obtained after the dipping-rinsing process (black line) and of a spin-coated **PHTT** film (red line) (λ_{probe} = 680 nm).

72

that in the absence of the inorganic semiconductor, charges are not generated in the conjugated polymer after photo-excitation. By considering the TA spectrum at longer times (> 100 ps), it is evident a progressive decrease of the signal associated to the photo-generated charges at the **PHTT**-TiO$_2$ interface, indicating that, after a fast charge separation, charge recombination also takes place in the system (Figure 2.14).
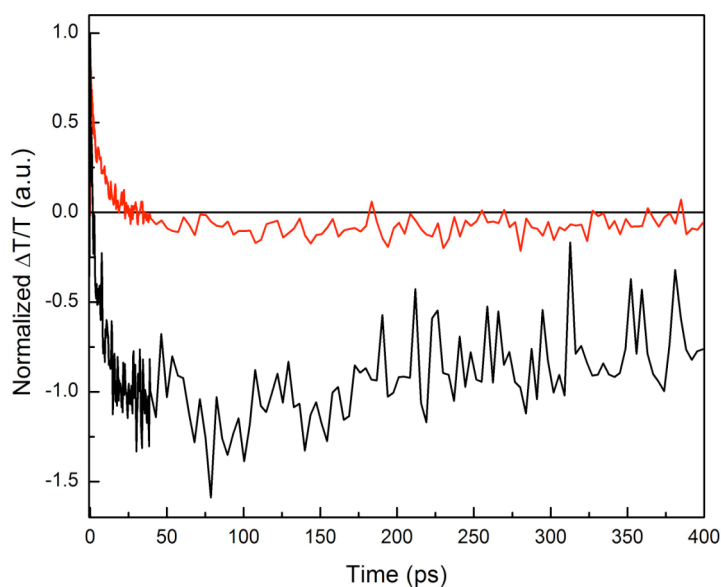
Figure 2.14. Time-resolved transient absorption spectra of the **PHTT**-PLD TiO$_2$ hybrid junction obtained after the dipping-rinsing process (black line) and of a spin-coated **PHTT** film (red line) (λ_{probe} = 680 nm).

2.3 Conclusions and outlook

In conclusion, it was demonstrated that poly(3,3''-dialkylterthiophenes) gives an effective infiltration into a hierarchical TiO$_2$ meso-architecture with an intimate contact between the two materials. Longer lateral alkyl chains and higher molecular weight conjugated chains have a negative

effect on polymer penetration into the empty spaces of the mesostructure and adsorption on its internal surface, as expected because of increased hydrophobicity and steric hindrance.

Ultra fast charge-transfer was observed from the conjugated polymer to the metal oxide, paving the way for the future development of hybrid solar cells. Anyway, a fast charge recombination was also detected. This process, expected from any system in a high-energy state, that has to return to its ground level, should be slower in photoactive layers, in order to allow efficient charge formation. A valuable strategy to speed up charge injection and reduce charge recombination might be the use of a donor polymer with better affinity for the polar surface of the inorganic semiconductor or the introduction of a molecular monolayer at the interface between the donor polymer and the acceptor metal oxide which increases their mutual compatibility. These possibilities will be explored in the next two chapters of this thesis. The low stability of the previously used PLD titania substrates under different polymer deposition conditions other than dipping (spin-coating, drop-casting), which might lead to a partial disruption of its characteristic nanomorphology, brought us to select a different type inorganic acceptor for the testing of novel organic materials. Specifically, the classical nanocrystalline TiO_2 paste, obtained through wet chemical methods, whose nanostructural stability makes it, at present, the benchmarck for polymer-nanostructured metal oxide hybrid photovoltaics and thus allow a easier and more reliable comparison between results and with the data from literature.

2.4 Experimental Section

Materials

PHTT, **PDTT-1** and **PDTT-2** were synthesized through the oxidative polymerization of the corresponding 3,3''-dialkyl-2,2':5',2''-terthiophene monomers following literature procedures.[2,3] The polymeric materials employed in the present work were the chloroform soluble fractions obtained after Soxhlet extraction. The higher molecular weight polymer **PDTT-2** was obtained by increasing the monomer dropping time into the oxidant suspension from 20 to 40 min and the reaction temperature from 40 °C to 45 °C. Molecular weights were determined by gel permeation chromatography (GPC) in THF at 35 °C using polystyrene standards with a Perkin-Helmer model 115.

PLD anatase TiO_2 samples were prepared as thoroughly described elsewhere.[4,6]

Methods

SEM images of the samples and XRF depth-profiling were acquired by a Zeiss SUPRA 40 field emission SEM equipped with a Oxford Instruments INCA X-ACT EDX microanalysis system.

GDOES depth-profiling was performed on a Spectruma GDA 550 HR GDOES instrument at an applied power of 40 W and argon pressure of 5 Torr. In order to ensure analysis under a clean source, a longer Ar flushing time of 60 s was employed. The sampling time was 0.001 s, the area of analysis was ~ 4 mm diameter and the spectral wavelengths employed for deterction of sulfur, titanium and indium were 180 nm, 399 nm and 451 nm respectively.

UV-visible absorption spectra were measured on a Jasco V570 spectrophotometer equipped with an integrating sphere to account for the diffusely transmitted light. The diffuse transmission measurements were

carried out by placing the samples with the scattering PLD photoanode slightly within the integrating sphere so as to collect completely the diffuse transmittance but, at the same time avoiding contribution from the reflectance. The diffuse reflection spectra were measured independently by placing the samples with the scattering PLD photoanode at the bottom of the integrating sphere in front of the incident light window, and were highly similar for all the samples analyzed. The final percentage absorption spectra were calculated using the formula A%=(1–T–R)*100, with A=absorption, T=transmission, R=reflection. Photoluminescence spectra were recorded with a Jasco FP 6600 spectrofluorometer.

For the ultrafast transient absorbtion (TA) measurements, the sample under study was resonantly photoexcited by a pump laser pulse and its subsequent dynamical evolution was detected by measuring the transmission (T) changes of a delayed probe pulse as a function of pump-robe delay given by the differential transmission $\Delta T/T[=(T_{pumpon}-T_{pumpoff})/T_{pumpoff}]$. The laser source was a regenerative amplified modelocked Ti:sapphire laser (Clark-MXR Model CPA-1), delivering pulses at 1 kHz repetition rate with 780 nm center wavelength, 150 fs duration. A fraction of this beam was used to pump a non-collinear optical parametric amplifier (NOPA) capable of delivering ultra-broadband pulses in the visible (500 – 750 nm). Another small fraction of the Ti: sapphire amplified output was independently focused into a 2-mm-thick sapphire plate to generate a stable single-filament white-light supercontinuum which serves as a probe pulse. A short-pass filter with 760 nm cutoff wavelength was used to filter out the residual 800 nm pump light thus limiting our probing window to the 450-760 nm region. The sample was excited at 530 nm and measured in a vacuum chamber.

76

References

[1] (a) Frank, B.; Gast, A.P.; Russell, T.P.; Brown, H.R.; Hawker, C.J. *Macromolecules*, **1996**, *29*, 6531-6534. (b) Ellison, C.J.; Torkelson, J.M. *Nature Mater.*, **2005**, *2*, 695-700.

[2] (a) Wu, J.; Gross, A..F.; Tolbert, S.H. *J. Phys. Chem. B*, **1999**, *103*, 2374-2384. (b) Bartholomew, G.P.; Heeger, A.J. *Adv. Funct. Mater.*, **2005**, *15*, 677-682. (c) Coackley, K.M.; Liu, Y.; McGehee, M.D.; Frindell, K.L.; Stucky, G.D. *Adv. Funct. Mater.* **2003**, *13*, 301-306. (d) Abrusci, A.; Ding, I.K.; Al-Hashimi, M; Segal-Peretz, T.; McGehee, M.D.; Heeney, M.; Frey, G.L.; Snaith, H.J. *Energy Environ. Sci.*, **2011**, *4*, 3051-3058.

[3] (a) Gallazzi, M.C.; Castellani, L.; Zerbi, G.; Sozzani, P. *Synth. Met.*, **1991**, *41*, 495. (b) Gallazzi, M.C.; Castellani, L.; Marin, R.A.; Zerbi, G. *J. Polym. Sci. Par t A: Polym. Chem.*, **1993**, *31*, 3339.

[4] Gallazzi, M.C.; Bertarelli, C.; Montoneri, E. *Synth. Met.*, **2002**, *128*, 91-95.

[5] Di Fonzo, F.; Casari, C.S.; Russo, V.; Brunella, M.F.; Li Bassi, A.; Bottani, C.E. *Nanotechnology*, **2009**, *20*, 015604.

[6] Sauvage, F.; Di Fonzo, F.; Li Bassi, A.; Casari, C.S.; Russo, V.; Divitini, G.; Ducati, C.; Bottani, C.E.; Comte, P.; Graetzel, M. *Nano Lett.*, **2010**, *10*, 2562-2567.

[7] Passoni, L.; Ghods, F.; Docampo, P.; Abrusci, A.; Martí-Rujas, J.; Ghidelli, M.; Divitini, G.; Ducati, C.; Binda, M.; Guarnera, S.; Li Bassi, A.; Casari, C.S.; Snaith, H.J.; Petrozza, A.; Di Fonzo, F. *ACS nano*, **2013**, *7*, 10023-10031.

[8] Hagfeldt, A.; Boschloo, G.; Sun, L.; Kloo, L.; Pettersson, H. *Chem. Rev.*, **2010**, *110*, 6595–6663.

[9] Nguyen, T.Q.; Wu, J.; Doan, V.; Schwart, B.J.; Tolbert, S. *Science*, **2000**, *288*, 652.

[10] For reviews see: (a) Baude, S.; Broeckaert, J.A.C.; Delfosse, D.; Jakubowski, N.; Fuechtjohann,, L.; Orellana-Velado, N.G.; Pereiro, R.; Sanz-Medel, A. *J. Anal. Atom. Spectr.*, **2000**, *15*, 1516-1525. (b) Winchester, M.R.; Payling, R. *Spectrochimica Acta Part B*, **2004**, *59*, 607-666.

CHAPTER 3

Functionalized Polythiophenes for Anchoring to Mesoporous TiO$_2$

3.1 Introduction

The efficiency of polymer-metal oxide hybrid solar cells depends critically on the intimacy of mixing between the two main constituents of the photo-active layer. Regioregular poly(3-hexylthiophene) (**P3HT**), as well as poly(3,3''-dihexyl-2,2':5',2''-terthiophene) (**PHTT**), are attractive candidates for hybrid solar cells in combination with nanocrystalline titanium dioxide, the former being at the moment the most widely used donor polymer material. Unfortunately, the hydrophobic nature of P3HT might represent a major obstacle for the obtainment of free photogenerated charges following light absorption, because of ineffective contact with the hydrophilic inorganic substrate. The introduction of tailored chemical functionalities on the polymer appears a promising prospect to yield novel donor polymers characterized by higher affinities for metal oxide surfaces. This strategy is already represented by several successful examples in the literature.[1]

Different functional groups have been employed to anchor sensitizer molecules to metal oxide semiconductor, including carboxylic acids,[2] cathecols,[3] sulfonates,[4] silanes[5] and phosphonic acids,[6] extending the possibilities for the future obtainment of novel polymer-based sensitizer with increased compatibility with inorganic semiconductors.

By considering the chemical structure of regioregular P3HT, three sites emerge for possible functionalization (Figure 3.1): the terminal position of the alkyl side chains and the polymer backbone, either at the 4-position of the thiophene rings along the main conjugated chain, or at the two chain end-positions[1b, 1g]. However, in polymers with sufficiently high molecular weight, which are usually preferred for their higher charge mobilities, the relative weight of terminal positions with respect
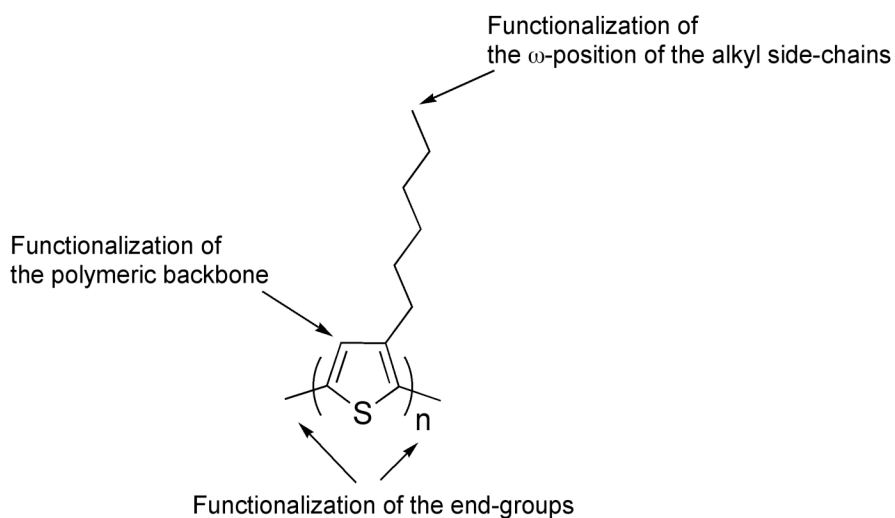
Figure 3.1. Possible sites for P3HT functionalization.

to the whole chain is low, thus limiting the effectiveness of the functionalization.

The introduction of chemical substituents in the aforementioned sites on the polymer chains is achieved by following different synthetic routes. Indeed, the preparation of ω-functionalized poly(3-alkylthiophenes) requires the previous obtainment of suitable monomers,[7] which are then subjected to polymerization via chemical oxidation,[8] electrochemical oxidation,[9] Grignard metathesis (GRIM)[10] or Pd(0)-catalyzed couplings.[11] Unfortunately this strategy is not applicable for all cases and may fail if, for example, functional groups take part of the reaction, prevent the polymerization process, affords low molecular weight polymers or promote cross-linking. Furthermore, even when the right reaction conditions are found, regioselectivity of the polymerization may still be an issue. Backbone functionalization is instead attainable through post-polymerization approaches, which allow the use of commercially

available PATs as starting materials.[1b,1g,12] In this case, the post-polymerization functionalization reaction should be characterized by high fidelity and high yields, and the experimental conditions should be relatively mild in order to avoid on one side the obtainment of only moderately derivatized polymers and, on the other, possible degradation.

In principle, the displacement of functional groups at the end of the alkyl side-chains should not directly influence the electronic properties of the polymer, differently from what happens when they are attached covalently to the backbone, thus possibly limiting π-conjugation.

In this thesis work, both the two last functionalization strategies were considered for P3HT in order to obtain donor materials with better affinities for nano-crystalline TiO_2 substrates. Particularly, synthetic efforts were addressed towards the preparation of ω-substituted P3HTs and backbone substituted P3HTs.

3.2 Results and discussion

3.2.1 Synthetic strategies towards functionalized poly(3-hexylthiophene)

Central building-blocks for ω-functionalized PATs consist of 3-(ω-bromoalkyl)thiophenes which can be converted, by appropriate substitution of the terminal bromine leaving group with various functionalities, to the corresponding desired monomers. Sulfur containing substituents, such as thiomethoxide or thiol groups are known to be suitable moieties for inducing selective interaction with the titania surface, and may thus be of interest in this study.[13] Indeed, metal oxide surface modification with alkanethiols monolayers reported by Lloyd *et al.* has resulted in an increase of the short circuit current in P3HT/ZnO

bilayer devices, because of better ordering in the P3HT chains.[14] On the other hand, the work of Zhang's group has evidenced by means of XPS analysis that the interaction of poly(3-alkylthiophenes) with nanocrystalline titanium dioxide takes place *via* the sulfur atoms of the thienyl moieties in the main conjugated chain.[15] The preparation of a poly(thiophene) derivative bearing pendant alkanethiol groups appears therefore as a good chance to determine which type of sulfur atom effectively leads the interaction with the metal oxide surface.

3-(6-bromohexyl)thiophene **3** was obtained through the route reported in Scheme 3.1, following the procedure described by Baurle *et al.*[16] 3-[ω-(*p*-Methoxyphenoxy)hexyl]thiophene **2** is accessible via the Grignard reagent derived from the corresponding [ω-(*p*-methoxyphenoxy)hexyl]bromide **1**, by nickel-catalyzed Grignard coupling with 3-bromothiophene. Ether cleavage with hydrobromic acid/acetic anhydride then leads to **3** in good yield.
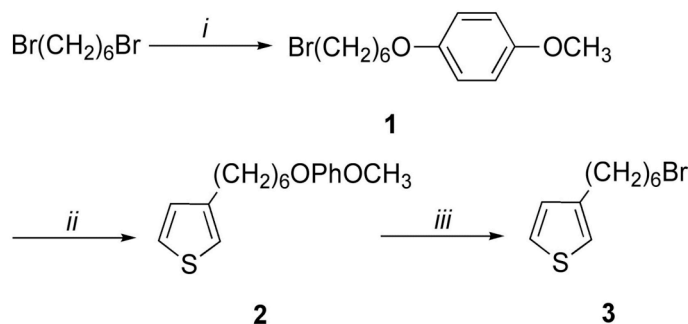
Scheme 3.1. Synthetic route to yield 3-(6-bromohexyl)thiophene **3**. *Reagents and conditions: i) p-*methoxyphenol, KOH, acetone/EtOH, Δ; *ii)* Mg, diethylether, 3-bromothiophene; *iii*) HBr/Ac$_2$O.

Starting from **3**, different strategies were evaluated for the synthesis of ω-functionalized P3HT derivatives, as depicted in Scheme 3.2.
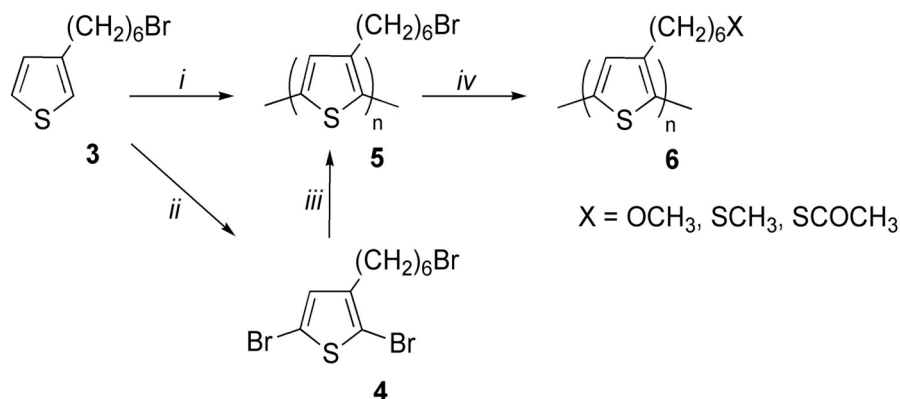
Scheme 3.2. Synthetic strategies towards ω-functionalized P3HTs **6**. *Reagents and conditions: i)* FeCl$_3$, CHCl$_3$; *ii)* NBS, DMF; *iii)* CH$_3$MgCl, Ni(dppp)Cl$_2$, THF, Δ; *iv)* NaX or KX

Unfortunately, all the efforts directed towards the obtainment of good-quality poly[3-(6-bromohexyl)thiophenes] have failed. The oxidative polymerization of **3** with anhydrous FeCl$_3$ described by Pomerantz *et al.*[17] as a successful route for the obtainment of highly soluble, regioregular poly[3-(6-bromohexyl)thiophene] **5**, gave in our hands only a very small percentage of soluble polymer, characterized by a high content of HH dyads, as evidenced by ^{1}H-NMR. The reaction therefore takes place with extremely low regioselectivity. Furthermore, the major product was a rubbish-like orange residue completely insoluble in many organic solvents and in water too, thus preventing material characterization *via* solution NMR and further chemical modification. The residue most likely contains cross-linked poly(3-hexylthiophene) chains, which prevent solubilization of the resulting polymer. The GRIM polymerization of **4** reported by McCollough and co-workers[18] furnished also a yellow-colored insoluble material. The residue may be constituted also in this case by a cross-linked polymer, resulting from the scarce selectivity of the Grignard metathesis reaction towards the three different

83

bromine substituents present in **4**. A suitable poly[3-(6-bromohexyl)thiophene precursor **5** was therefore not available for subsequent post-polymerization nucleophilic substitution.

A different synthetic approach was attempted, consisting in the substitution of the ω-bromine before the polymerization reaction. Specifically, we follow the procedure described by Lanzi *et al.* for the preparation of poly[3-(6-methylthiohexyl)polythiophene (Scheme 3.3).[19]
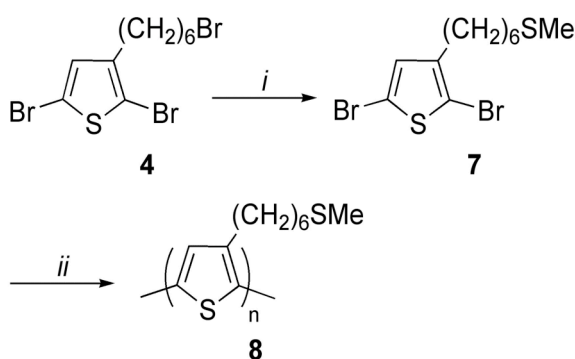
Scheme 3.3. Synthesis of poly[3-(6-methylthiohexyl)polythiophene **8**. *Reagents and conditions: i)* NaSCH$_3$, EtOH, Δ; *ii)* CH$_3$MgBr, Ni(dppp)Cl$_2$, THF, Δ.

Nucleophilic substitution involving the –Br atom at the end of the side chain in **4** with excess sodium thiomethoxide furnished 2,5-dibromo-3-[6-(methylsulfanyl)hexyl]thiophene **7** in almost quantitative yield. However, the GRIM polymerization reaction did not proceed to completion, leading just to a mixture of oligomeric products of difficult separation and characterization. The presence of the thiomethoxide group probably modifies the activity and selectivity of the Ni(dppp)Cl$_2$ catalyst, by directly acting on the Grignard cross-coupling mechanism.

Being not previously described in the literature, the oxidative polymerization of 3-[6-(methylsulfanyl)hexyl]thiophene **9** was also attempted (Scheme 3.4).
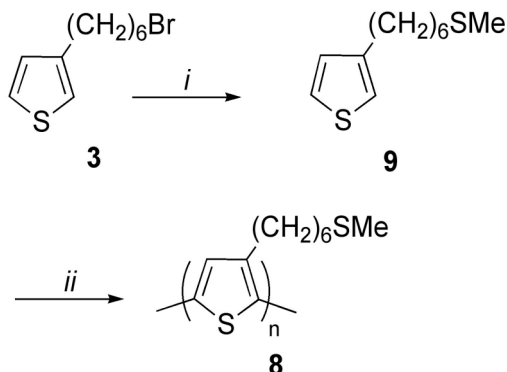
Scheme 3.4. Synthesis of poly[3-(6-methylthiohexyl)polythiophene **8**. *Reagents and conditions: i)* NaSCH$_3$, EtOH, Δ; *ii)* FeCl$_3$, CHCl$_3$.

Also this trial gave not satisfactory results, providing again a product totally insoluble in organic solvents. Since polymer doping has been supposed at the basis of insolubility, de-doping was attempted many times, but did not give any improvement in material solubility.

Given the difficulties found in the preparation of good-quality ω-functionalized P3HTs, this route was not further considered and attention was shifted to backbone functionalization of commercially available regioregular P3HT. A post-polymerization functionalization procedure was chosen, which requires two synthetic steps for the introduction of substituents in the 4-position of the thienyl rings along the polymer chain (Scheme 3.5).[15a,15b,20] Bromination of P3HT *via* electrophilic substitution is followed by Pd(0)-catalyzed Suzuky cross-couplings for linking the functionalized phenyl rings. Using this approach, it is possible to tune the ratio of functional moieties versus thiophene units by varying the amount of bromine introduced in the first step: in principle, any content could be realized experimentally. Furthermore, it is possible to introduce different types of chemical functionalities. A drawback of this methodology lies in

85
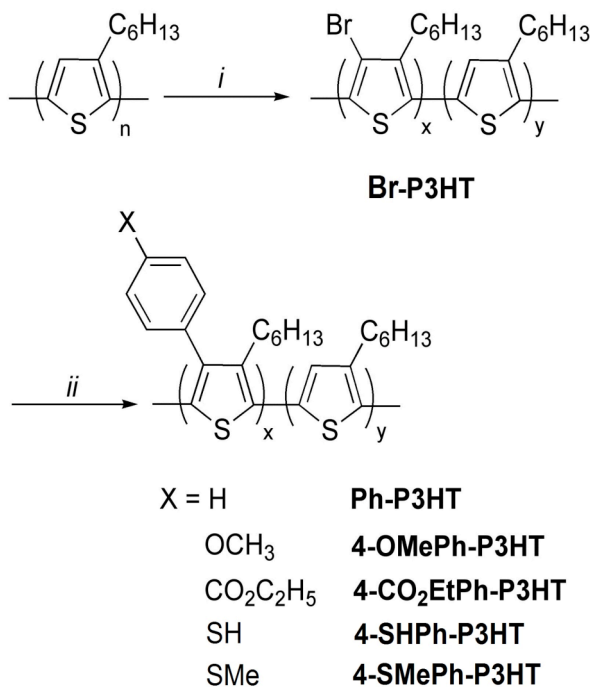
Scheme 3.5. Synthetic route to yield backbone functionalized P3HTs. *Reagents and conditions: i)* NBS, CHCl$_3$; *ii)* 4-XPhB(OH)$_2$, Pd(PPh$_3$)$_4$, K$_2$CO$_3$, Toluene/H$_2$O.

the inability to effectively control the relative position of substituents on the main conjugated backbone, which are therefore randomly distributed on the polymer chains. A bromine substitution ratio of ca. 15% was chosen for the first step (x = 0.15), aimed at subsequently obtaining an appropriate ratio of functionalities without a too strong influence on the conjugated structure of P3HT. The confirmation of the successful 15% bromine substitution of P3HT affording **Br-P3HT** was given by ^{1}H-NMR analysis, according to the integral ratio of H(g) to H(a) (Figure 3.2). Suzuki couplings of **Br-P3HT** with various phenylboronic acids were attempted according to what reported in Scheme 3.5. Some resulted successful, leading to a complete substitution of the bromine atoms in the 4-position of the thienyl rings with phenyl groups, as for the case of **Ph-P3HT**, **4-OMePh-P3HT** and **4-CO$_2$EtPh-P3HT** derivatives. Others

instead were either completely unsuccessful, leading to the recovery of only un-reacted Br-P3HT (**4SHPh-P3HT**) or gave a minimum amount of bromine substitution (**4-SMePh-P3HT**), not enough for considering the material a good candidate for the desired purposes. Also for these derivatives, as for the **Br-P3HT** precursor, ^{1}H-NMR analysis allowed to precisely estimate the degree of functionalization of the polymer chains. Indeed, the presence of selective signal in the spectra due to the covalently bound functional moieties allowed calculating the percentage of backbone substitution from integral ratios (Figure 3.2). Particularly, for the case of **4-OMePh-P3HT** and **4-CO₂EtPh-P3HT** integral ratios were calculated for the methyl protons in the methoxy groups (Hj) and for the methylene protons in the ethoxy groups (Hj) respectively to the broad peak at almost 0.9 ppm due to the terminal methyl protons on the alkyl side-chains (Ha) present in both spectra. Unfortunately, it is not possible to assign a precise value of substitution to the **Ph-P3HT** derivative, being the signal of the benzene protons lying below the hydrogen signal due to exchanged deuterated chloroform, which hinder exact integration. Finally, it is evident from the relative spectrum the very small substitution ratio achieved for **4-SMePh-P3HT**.
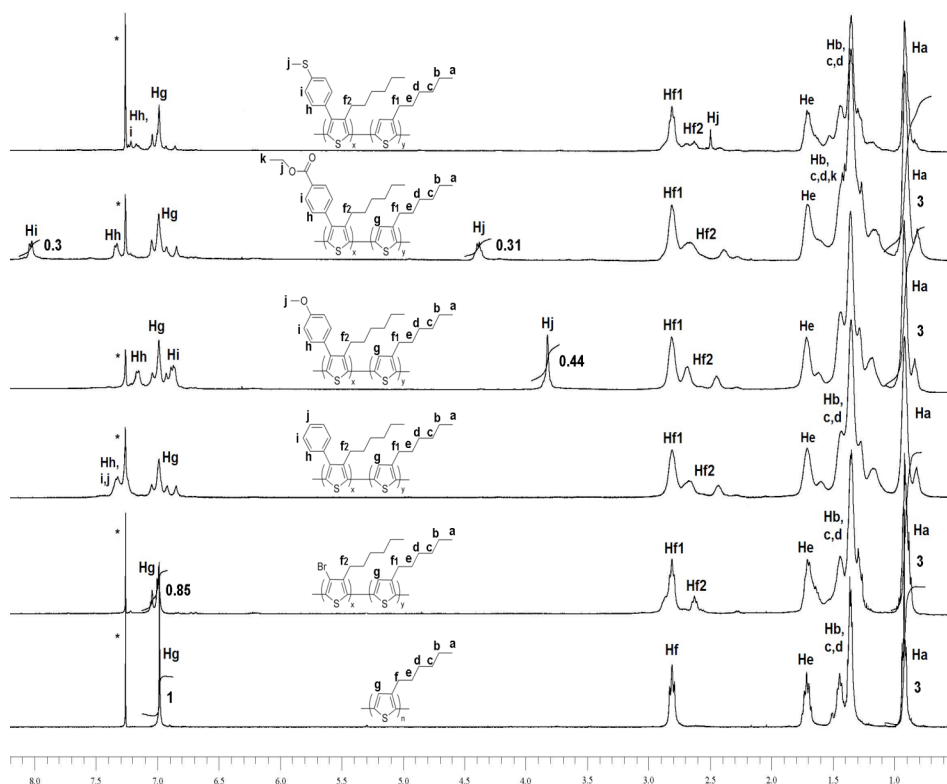
Figure 3.2. ^{1}H NMR spectra of **P3HT** (a), **Br-P3HT** (b), **Ph-P3HT** (c), **4-OMePh-P3HT** (d), **4-CO$_2$EtPh-P3HT** (e) and **4-SMePh-P3HT** (f). All polymers were completely dissolved in deuterated chloroform and spectra were recorded at room temperature. The solvent line of CHCl$_3$ is marked with an asterisk.

3.2.2 Characterization of the functionalized poly(3-hexylthiophenes)

The three post-polymerization functionalized P3HT derivatives **Ph-P3HT**, **4-OMePh-P3HT** and **4-CO$_2$EtPh-P3HT** were further characterized by UV-visible spectroscopy and their optical absorption spectra in chloroform solutions are reported in Figure 3.3, in comparison with the absorption spectrum of the un-functionalized **P3HT** precursor.
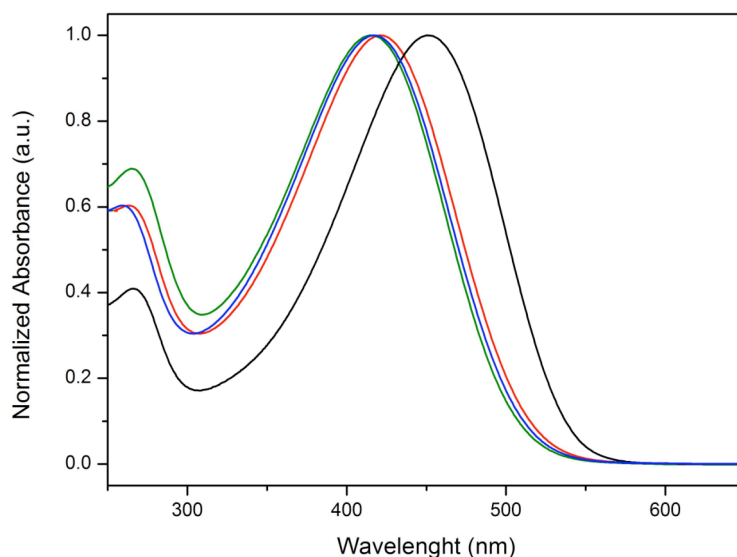
Figure 3.3. UV-visible absorption spectra in chloroform solutions of **P3HT** (black line), **Ph-P3HT** (red line), **4-OMePh-P3HT** (blue line) and **4-CO₂EtPh-P3HT** (green line).

The absorption maxima of the three functionalized polymers are significantly blue-shifted compared to **P3HT** (Table 3.1), due to the steric hindrance of the phenyl groups there attached. The small differences in absorption maxima among the three derivatives may be due to weak electronic effects of the *para*-substituents on the phenyl rings.

The absorption spectra of the three polymers in films obtained *via* spin-coating are also reported in Figure 3.4, together with the spectrum of a spin-coated **P3HT** film. A general bathochromic shift in the absorption maxima is observed with respect to solution spectra, as a consequence of better planarization of the polymer backbones at the solid state due to intermolecular packing (Table 3.1).
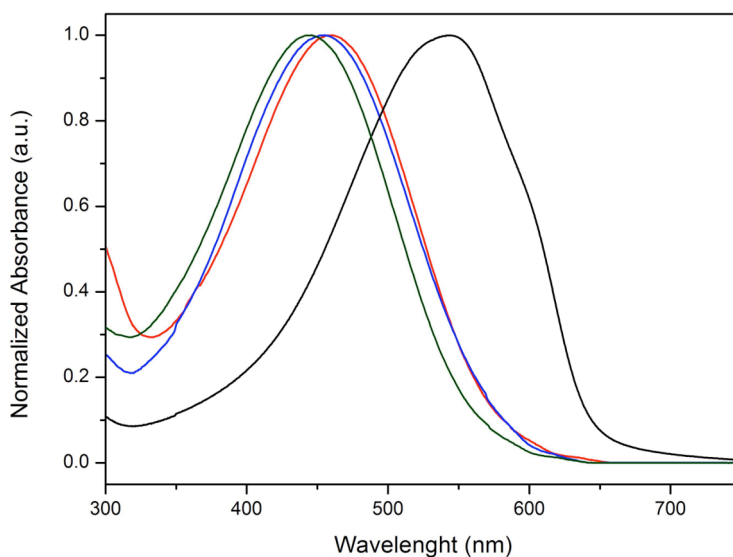
Figure 3.4. UV-visible absorption spectra as spin-coated films of **P3HT** (black line), **Ph-P3HT** (red line), **4-OMePh-P3HT** (blue line) and **4-CO₂EtPh-P3HT** (green line).

Table 3.1. Absorption maxima (nm) of the functionalized P3HT derivatives and un-functionalized P3HT precursor in chloroform solutions and in spin-coated films.

Polymer	**Ph-P3HT**	**4-OMePh-P3HT**	**4-CO₂EtPh-P3HT**	**P3HT**
Solution	422	416	414	451
Solid state	460	453	443	543

As expected, this effect is less evident for the functionalized polymers than for P3HT, again due to the steric effect of substituents. Consistently, band structuring is not evident in any of the three functionalized polymer films spectra, remarking a difficulty for these materials in providing well-defined packing features. On the contrary, the **P3HT** film spectrum presents a more structured absorption band. The extent of band structuring in **P3HT** is commonly attributed to the degree of polymer crystallinity, which is noticeable here in the **P3HT** film spectrum even without an annealing treatment, indicating the strong tendency of this

material to self-organize at the solide state, also when using a fast deposition technique such as spin-coating.

To gain further insight into the solid state organization of the post-polymerization functionalized **P3HT** derivatives, the thermal behavior of **4-CO₂EtPh-P3HT** as a model for the other two derivatives was studied by differential scanning calorimetry and compared to the behavior of un-functionalized **P3HT**. The thermograms for the two polymers are reported in Figure 3.5.
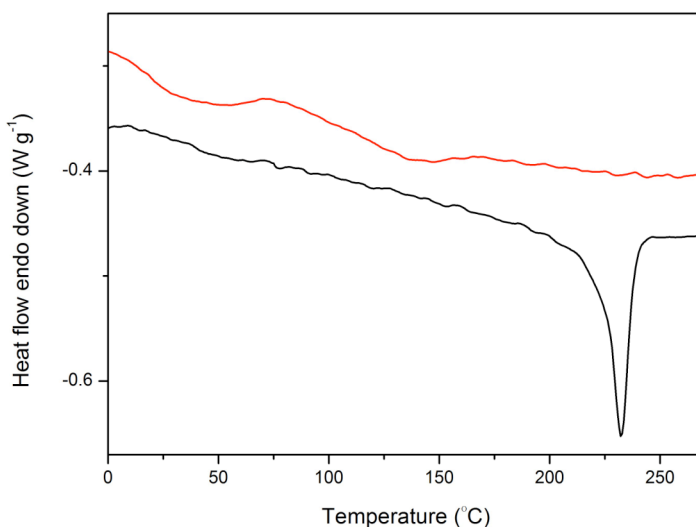
Figure 3.5. Differential scanning calorimetry heating curves for **P3HT** (black line) and **4-CO₂EtPh-P3HT** (red line) obtained after a previous heating scan followed by fast cooling. The heating rates were both 10 °C min⁻¹.

The scans were obtained after a previous heating scan from 0 to 260 °C followed by fast cooling, aimed at eliminating thermal history in the samples. The analysis clearly evidences the loss of crystallinity in the functionalized polymer with respect to the pristine **P3HT** precursor. The intense endothermic peak in the **P3HT** scan at 232 °C is completely absent in the **4-CO₂EtPh-P3HT** scan, which shows instead a glass

91

transition at around 50 °C. Substitution ratio of 15% furnishes therefore an amorphous material, as a consequence of the phenyl groups distributed along the main polymer chains, which prevents chains to organize in ordered structures.

3.2.3 Use of the functionalized poly(3-hexylthiophenes) as organic components in hybrid solar cells

The ability of the three functionalized polymers to interact with porous films of the standard nanocrystalline TiO_2 paste was verified, in order to select the derivative with better affinity for the metal oxide surface for its subsequent use in hybrid solar cells.

1 µm thick mesoporous nc-TiO_2 films deposited on a compact TiO_2 layers lying on FTO substrates were immersed for 18 h in 15 mg ml^{-1} chloroform solutions of **P3HT**, **Ph-P3HT**, **4-OMePh-P3HT** and **4-CO$_2$EtPh-P3HT**, analogously to what described in Chapter 2 for the **PTTs** infiltration into PLD TiO_2 scaffolds. Afterwards, the polymer-sensitized samples were rinsed thoroughly with CHCl$_3$, until washings were colorless. As a result of this procedure, completely un-colored nc-TiO_2 films were obtained for the cases of **P3HT**, **Ph-P3HT**, **4-OMePh-P3HT**, stating the complete removal of the polymeric materials from the inorganic substrates. The sample dipped in the **4-CO$_2$EtPh-P3HT** solution maintained instead a red color, indicating the presence of a polymer layer in contact with the inorganic nanoparticles dispersion. The behavior is justified by the presence of the ester functions in **4-CO$_2$EtPh-P3HT**, which make the polymer more hydrophilic and therefore more compatible with the polar metal oxide surface, similarly to what reported previously by Janssen and coworkers for an ester functionalized

P3HT derivative (P3HT-E) blended with ZnO nanoparticles (see Chapter 1, section 1.2.4).[21]

The performance of **4-CO$_2$EtPh-P3HT** in nc-TiO$_2$-polymer hybrid photovoltaic cells was verified. Solar cells were prepared and tested at CNST@Polimi by Dr. Ing. M. Binda. Two different strategies were followed: in the first one, the same protocol for state-of-the-art nc-TiO$_2$/P3HT hybrid solar cells has been followed in parallel for **P3HT** and for **4-CO$_2$EtPh-P3HT**. In this procedure, the conjugated polymer is deposited by spin coating onto the nanocrystalline titania film from a 30 mg ml^{-1} chlorobenzene solution. This deposition procedure is a fast way to obtain infiltration of the polymer into the voids of the metal oxide nanostructure, thus speeding up the process of solar cell manufacturing. Spin-coater rotation is activated 15'' after dispensing the solution onto the substrate in order to further promote polymer infiltration inside the mesoporous TiO$_2$ layer. A polymer layer is thus obtained, filling the internal voids of the metal oxide and a polymer capping layer is also expected from this processing, since no solvent rinsing was carried out after polymer deposition. Accordingly, **4-CO$_2$EtPh-P3HT** works both as sensitizer and EBL in this configuration. The metal electrode is then directly deposited on top of the EBL. The polymer plays both the roles of light absorber and hole-transporter in this configuration, the latter requiring a good level of crystallinity in the material in order to ensure efficient transport of charges toward the metal electrode. Given the lack of crystalline in **4-CO$_2$EtPh-P3HT**, as evidenced through thermal studies, hole-transport in this material is expected to take place with some difficulties, consequently leading to low performance in the hybrid device based on such photo-active polymer donor. Figure 3.6 reports The *J-V* characteristics for the hybrid devices having the indicated

93
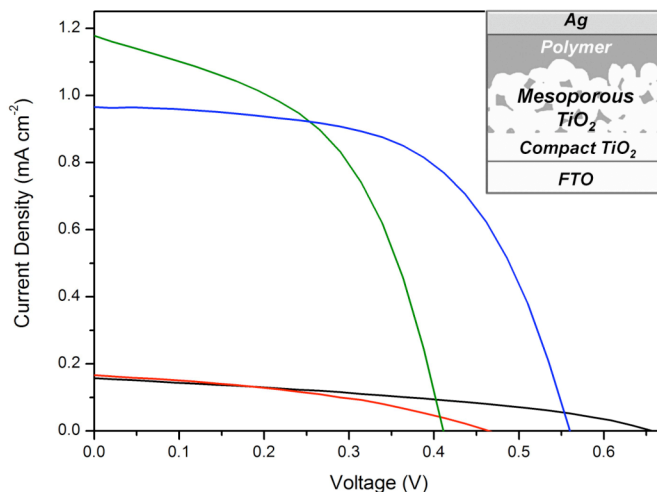
Figure 3.6. Current-voltage characteristics for mesoporous TiO_2-polymer hybrid photovoltaic cells measured under AM1.5 simulated sun light of 100 mW cm^{-2}, where **4-CO$_2$EtP3HT** was used as photo-active polymer before (black line) and after annealing at 150 °C for 30' (red line), compared to the same curves obtained with **P3HT** before (blue line) and after annealing (green line). The inset reports the schematic of the devices.

configuration, based on **4-CO$_2$EtPh-P3HT** and **P3HT** as the donor materials, measured under AM1.5 simulated sun light of 100 mW cm^{-2}. Whereas the open-circuit voltage results higher in the device based on **4-CO$_2$EtPh-P3HT** with respect to the device based on un-functionalized **P3HT**, the short-circuit current results almost ten times lower. The slightly higher voltage measured for the **4-CO$_2$EtPh-P3HT** containing devices may be explained with the effect of a lower lying HOMO energy level of **4-CO$_2$EtPh-P3HT** compared to **P3HT**, which results in an increased energy difference between such level and the titania conduction band. Unfortunately, no other experimental evidence supports this hypothesis. The low photo-current values are surely due to the complete loss of crystallinity in the ester functionalized polymer,

94

which prevent the efficient transport of positive charges throughout the polymer layer toward top metal electrode.

Once proven the inability of **4-CO$_2$EtPh-P3HT** to effectively transport holes, a novel solar cell configuration was devised, in which the ester-functionalized polymer was used as an interlayer between the nanocrystalline titania substrate and a upper **P3HT** layer. The role of hole-conductor is now played by **P3HT**, whereas the functionalized polymer acts as compatibilizer between the hydrophobic **P3HT** chains and the polar metal oxide surface. The solar cells characteristics are reported in Figure 3.7, together with the results already reported for the device with the sole **4-CO$_2$EtPh-P3HT** as photo-active material and hole-conductor.
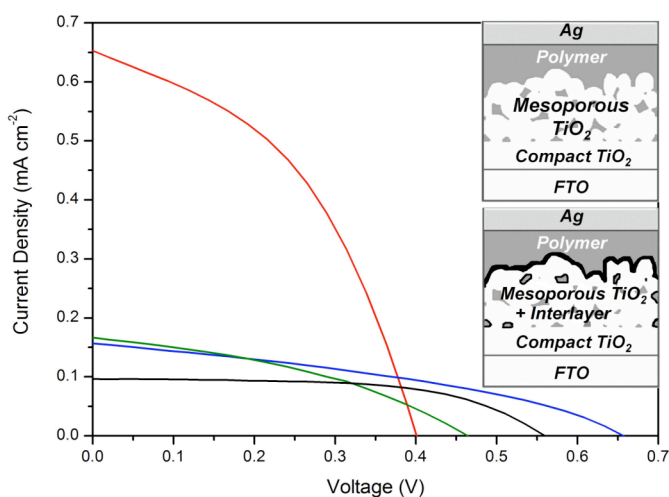
Figure 3.7. Current-voltage characteristics for mesoporous TiO$_2$-polymer hybrid photovoltaic cells measured under AM1.5 simulated sun light of 100 mW cm^{-2}, where **4-CO$_2$EtP3HT** was used interlayer between the nanocrystalline titania paste and a spin-coated **P3HT** layer before (black line) and after annealing at 150 °C for 30' (red line), compared to the same curves obtained with the use of only **4-CO$_2$EtP3HT** as photo-active polymer before (blue line) and after annealing (green line). The insets report the schematics of the devices in both configurations, namely with and without interlayer.

95

As can be envisaged from these curves, the open circuit voltage of the device having nc-TiO$_2$/**4-CO$_2$EtPh-P3HT**/**P3HT** active layer configuration resembles the one previously obtained for the nc-TiO$_2$/**P3HT** configuration and not the one for the nc-TiO$_2$/**4-CO$_2$EtPh-P3HT** configuration. This is reasonable if one thinks that in the present case the light absorbing and electron-donor material is **P3HT**, which consequently drives the cell voltage outcome with the position of its HOMO energy level in relation to the TiO$_2$ conduction band. The photo-current extracted from the device with the ester-functionalized polymer as interlayer increases dramatically after thermal treatment, most likely as a result of solid state reorganization of the **P3HT** layer in the bulk and probably also at the interface with **4-CO$_2$EtPh-P3HT**, but not enough to reach the value previously obtained with the nc-TiO$_2$/**P3HT** device without an interfacial modification (see Figure 3.6 and Table 3.2). The presence of the polymer interlayer is thus resulting detrimental for device performance. We suppose that **4-CO$_2$EtPh-P3HT** acts as a physical obstacle to charge-separation as a result of its disordered nature: the interlayer might arrange in random coiled structures on the hybrid interface, thus hindering the consequent good organization of the first **P3HT** layers in direct contact with it. Table 3.2 includes the characteristic parameters obtained for all the devices presented before.

Table 3.2. Characteristic solar cell parameters for polymer-nanostructured TiO$_2$ hybrid devices described in this work.

Active-layer configuration	V_{OC} (V)	J_{SC} (mA cm^{-2})	FF	η (%)
nc-TiO$_2$/**4-CO$_2$EtPh-P3HT**	0.65	0.16	0.37	0.05
nc-TiO$_2$/**4-CO$_2$EtPh-P3HT**+ annealing	0.46	0.18	0.39	0.04
nc-TiO$_2$/**P3HT**	0.56	0.97	0.58	0.33
nc-TiO$_2$/**P3HT**+annealing	0.41	1.18	0.51	0.37
nc-TiO$_2$/**4-CO$_2$EtPh-P3HT**/ **P3HT**	0.56	0.09	0.36	0.03
nc-TiO$_2$/**4-CO$_2$EtPh-P3HT**/ **P3HT**+annealing	0.4	0.65	0.43	0.15

As shown before, the random substitution of regioregular P3HT is likely resulting in highly coiled polymer chains, unable to arrange in crystalline domains, needed for good transport of positive charges across the material, when used as the polymer donor component in hybrid polymer/nc-TiO$_2$ solar cells but also transferring its disordered nature to the highly crystalline pristine P3HT precursor, when used as a thin layer between the latter and the nanocrystalline titania substrate. The use of an analogously functionalized polymer, characterized by better ordering in the chemical structure and consequently in the solid state organization, might therefore be a reasonable way to achieve on one side good interactions with the metal oxide surface and on the other to gain good hole transport capabilities or the ability to create a local order at the hybrid interface which favors charge injection and lessens charge recombination. This goals might be achieved by using the quasi-symmetric poly[(4-ethoxycarbonyl)3-phenyl-3',3''-dihexyl-2,2':5',2''-terthiophene] (**4-CO$_2$EtPh-PHTT**), whose chemical structure together with its synthetic route are reported in Scheme 3.6.

97
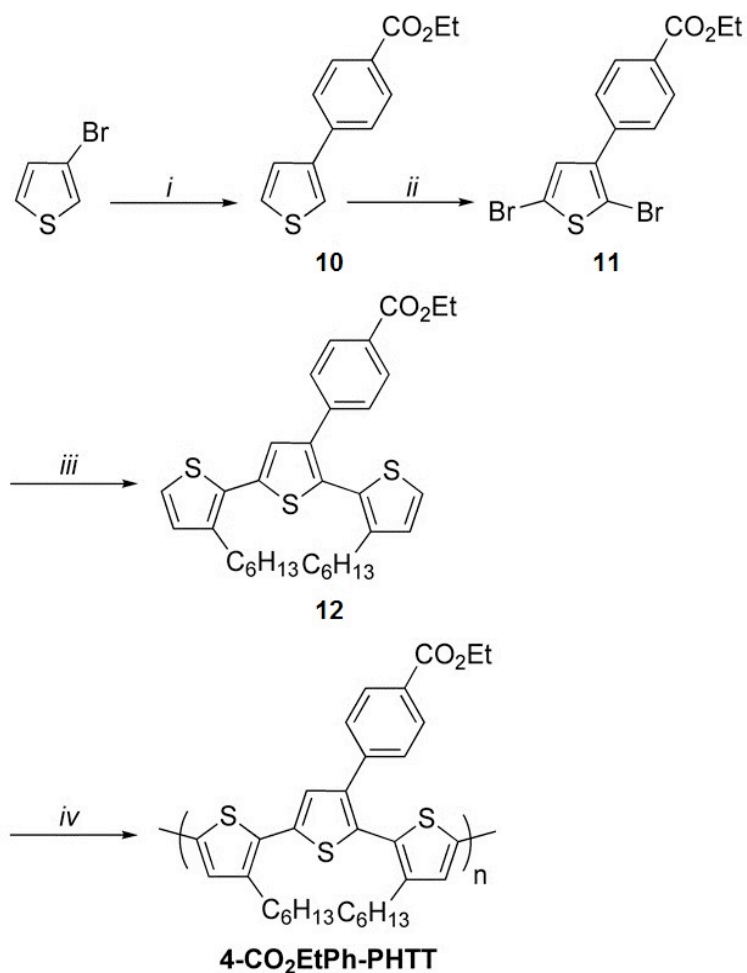
Scheme 3.6. Synthesis of **4-CO₂EtPh-PHTT**. *Reagents and conditions: i) 4-CO₂EtPhB(OH)₂, Pd(PPh₃)₄, K₂CO₃, DME/H₂O; ii) NBS, DMF; iii) 3-hexylthiophene-2-boronic acid pinacol ester, Pd(PPh₃)₄, K₂CO₃, DME/H₂O, Δ; iv) Cu(ClO₄)₂·6H₂O, CH₃CN.*

The synthetic approach employed for the preparation of the functionalized poly(terthiophene) derivative requires the previous obtainment of the (4-ethoxycarbonyl)3-phenyl-3',3''-dihexyl-2,2':5',2''-terthiophene monomer **12**, which is then oxidatively polymerized. The use of a quasi-simmetrical monomer such as **3** allows obtaining a

regioregular polymer for what concern the relative positions of the hexyl side-chains, as already discussed in Chapter 2, but not for what regards the internal substituted phenyl rings. Differently from **4-CO₂EtPh-P3HT**, the substituted phenyl rings are not located in α-position with respect to an alkyl tail, but more "isolated" on the central thienyl ring to which are covalently bound. This design might result in a diminished distorsion of the latter, with longer effective conjugation length. The effect is confirmed by the UV-visible absorption spectrum of **4-CO₂EtPh-PHTT**, which results 10 nm red-shifted with respect to the one of **4-CO₂EtPh-P3HT** (Figure 3.8), but still blue-shifted compared to pristine **P3HT**.

The new polymer might therefore be a good candidate for the aforementioned purposes, being likely characterized by a lower distorsion of the main conjugated chain and consequently a more pronounced ability to arrange in a better fashion at the solid state. Furthermore, by considering the chemical structure of the new polymer, it is evident that **4-CO₂EtPh-PHTT** is characterized by a higher content of ethyl ester moieties (~30%) if compared with **4-CO₂EtPh-P3HT** (15%). This might result in better affinity the metal oxide surface. Alternatively to the use of a polymeric material as interfacial modifier between nc-TiO₂ and P3HT, the use of molecular materials

having structures similar to monomer **3**, in which one side bears a substituent with good affinity for the inorganic substrate and the other thienyl rings, also further substituted with alkyl chains, ensuring compatibility with the polymer structure, might be envisaged. Indeed, a monolayer of these small molecules could result even more effective in creating a suitable order at the hybrid interface, beneficial for increased
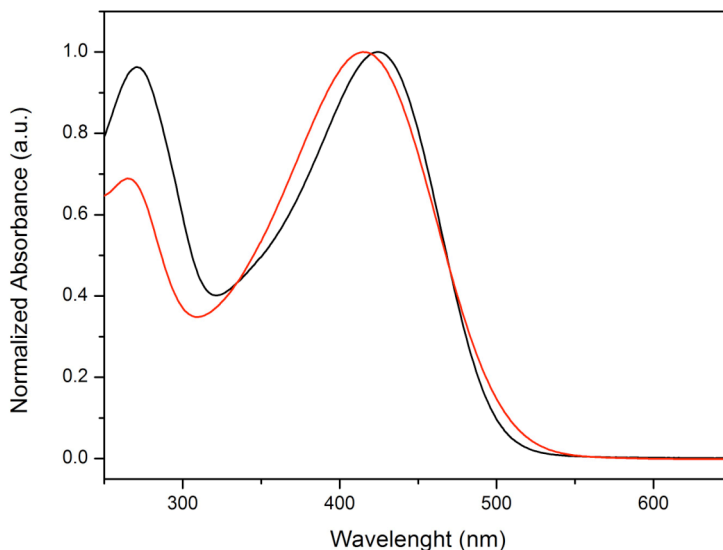
Figure 3.8. UV-visible absorption spectra of **4-CO₂EtPh-PHTT** (black line) and **4-CO₂EtPh-P3HT** (red line).

charge injection and reduced charge recombination, with respect to a thin polymer layer. This approach is discussed in Chapter 4.

3.3 Conclusions and outlook

In this chapter, we demonstrated the possibility to address specific interactions between a conjugated polymer and a nanocrystalline titanium dioxide matrix by decorating the former with ethyl ester functionalities. Moreover, the fundamental role of solid-state organization in determining the good transport of charges throughout a photo-active material is also stated. The amorphous character of the ester-functionalized polymer donor reported here for the first time has a more pronounced influence on the final performance of a hybrid solar cell (in which is used as the organic component) than its affinity for the inorganic acceptor surface. Also, when the material is used as a thin layer at the nc-TiO₂/P3HT interface with the aim of increasing the

compatibility between the two main components, its highly irregular conformation contributes negatively to the construction of a local order at the interface, suitable for good charge separation after light absorption.

Based on these considerations therefore, a new approach has been considered dealing with interlayers, which combines the affinity for the polar metal oxide surface with the ability to drive the ordering of the first P3HT layers lying on the hybrid interface. In the next chapter a novel series of oligothiophene interlayers is presented.

3.4 Experimental Section

Materials

Unless otherwise specified, all reagents, catalysts, spectroscopic grade, and reagent grade solvents were purchased from Sigma Aldrich and used without further purification. P3HT (MW=77500, PD=2 and RR=96.3) was purchased from Merck and used without further purification. 4-(Ethoxycarbonyl)phenylboronic acid was synthesized following a literature procedure.[22] ^{1}H and ^{13}C NMR spectra were obtained on a Bruker ARX 400. ESI-MS was performed on a Bruker Esquire 3000 plus.

The post-polymerization functionalized P3HT derivatives were synthesized according to the following procedures.

Poly(3-bromo-4-hexylthiophene) (**Br-P3HT**). NBS (10 mg, 0.63 mmol) was added as a solid to a flask containing P3HT (60 mg, 0.36 mmol, M_n = 27100, M_w = 60500, RR = 96.3%) in chloroform (30 mL). The solution was stirred at room temperature for 15 min and then heated at 50 ^{o}C for 2 h. After cooling, the reaction mixture was poured into a saturated NaHCO$_3$ solution (50 mL). The organic layer was washed with water six times and dried over Na$_2$SO$_4$. Precipitation into methanol gave a black

101

solid, which was subjected to Soxhlet extraction with methanol, hexane and chloroform. The chloroform fraction was concentrated and poured into methanol, to yield the brominated polymer as a red solid, which was filtered and dried in vacuum (53 mg). ^{1}H-NMR (400 MHz, CDCl$_3$, ppm): δ 7.00 (0.85 H, m, Th*H*), 2.81 (1.7 H, broad, ThC*H$_2$*), 2.63 (0.3H, broad, ThC*H$_2$*), 1.71 (2 H, broad, ThCH$_2$C*H$_2$*), 1.36 (6H, broad, -(C*H$_2$*)$_3$-), 0.92 (3H, broad, -C*H$_3$*).

Poly(3-hexyl-4-(phenyl)-thiophene) (**Ph-P3HT**). **Br-P3HT** (17 mg, 15% bromine substitution, 0.014 mmol Br) and phenylboronic acid (11 mg, 0.091 mmol) were mixed in argon degased toluene (20 mL) under an inert atmosphere while stirring. After **Br-P3HT** was dissolved completely, K$_2$CO$_3$ (13 mg, 0.098 mmol), water (10 ml) and 10% equiv molar of Pd(PPh$_3$)$_4$ (2 mg, 0.0014 mmol) were added. The mixture was then heated up to reflux temperature for 24 h. The reaction mixture was cooled to room temperature, then diluted with chloroform and washed with water three times to remove the excess boronic acid. The organic layer was dried with Na$_2$SO$_4$, concentrated and the polymeric material was precipitated from methanol. After purification with methanol and hexane using a Soxhlet extractor, the as-prepared functionalized polymer was extracted in chloroform and, after concentration, precipitated again from methanol and dried in vacuum (15 mg). ^{1}H-NMR (400 MHz, CDCl$_3$, ppm): δ 7.33 (~0.75H, m, Ph*H*), 6.99 (0.85 H, m, Th*H*), 2.81 (1.7H, broad, ThC*H$_2$*), 2.43 (0.3H, broad, ThC*H$_2$*), 1.71 (2H, broad, ThCH$_2$C*H$_2$*), 1.27 (6H, broad, (C*H$_2$*)$_3$), 0.92 (2.55H, broad, -C*H$_3$*), 0.82 (0.45H, broad, -C*H$_3$*).

Poly(3-hexyl-4-(4-methoxyphenyl)-thiophene) (**4-OMePh-P3HT**). This polymer was synthesized following the same procedure described for **Ph-P3HT**, starting from **Br-P3HT** (15 mg, 15% bromine substitution, 0.012

mmol Br) and 4-(methoxy)phenylboronic acid (12 mg, 0.08 mmol). Soxhlet extraction and precipitation from methanol gave 13 mg of **4-OMePh-P3HT**. ^{1}H-NMR (400 MHz, CDCl$_3$, ppm): δ 7.16 (0.3H, d, J = 7 Hz, Ph$H2,6$), 6.99 (0.85 H, m, ThH), 6.87 (0.3H, d, J = 7 Hz, Ph$H3,5$), 3.82 (0.45H, broad, OCH_3), 2.81 (1.7H, broad, ThCH_2), 2.45 (0.3H, broad, ThCH_2), 1.72 (2H, broad, ThCH$_2$CH_2), 1.36 (6H, broad, (CH_2)$_3$), 0.92 (2.55H, broad, -CH_3), 0.83 (0.45H, broad, -CH_3).

Poly(3-hexyl-4-(4-ethoxycarbonylphenyl)-thiophene) (**4-CO$_2$EtPh-P3HT**). This polymer was synthesized following the same procedure described for **Ph-P3HT**, starting from **Br-P3HT** (25 mg, 15% bromine substitution, 0.021 mmol Br) and 4-(ethoxycarbonyl)phenylboronic acid (25 mg, 0.13 mmol). Soxhlet extraction and precipitation from methanol gave 26 mg of **4-CO$_2$EtPh-P3HT**.^{1}H-NMR (400 MHz, CDCl$_3$, ppm): δ 8.03 (0.3H, d, J = 7 Hz, Ph$H3,5$), 7.34 (0.3H, d, J = 7 Hz, Ph$H2,6$), 6.99 (0.85 H, m, ThH), 4.40 (0.3H, broad, OCH_2), 2.81 (1.7H, broad, ThCH_2), 2.39 (0.3H, broad, ThCH_2), 1.71 (2H, broad, ThCH$_2$CH_2), 1.39 (6.45H, broad, (CH_2)$_3$ + OCH$_2$CH_3), 0.92 (2.55H, broad, -CH_3), 0.82 (0.45H, broad, -CH_3).

The synthesis and characterization of compounds **10**, **11**, **12** and polymer **4-CO$_2$EtPh-PHTT** are described in the following procedures.

3-(4-ethylbenzoate)-thiophene (**10**). A stirring solution of 3-bromothiophene (0.11 ml, 1.2 mmol) in argon degased DME (25 ml) was treated with K$_2$CO$_3$ (1.15 g, 8.3 mmol), degased H$_2$O (12.5 ml) and Pd(PPh$_3$)$_4$ (139 mg, 0.12 mmol). The mixture was stirred for 10 min under an argon atmosphere, whereupon (4-ethoxycarbonyl)phenylboronic acid (230 mg, 1.2 mmol) was added and reflux was started and continued for 8 hours. After cooling to room temperature, the reaction mixture was poured into water (20 ml) and

103

extracted with Et$_2$O (2 x 20 ml). The combined organics were dried (Na$_2$SO$_4$), filtered and concentrated to leave a brown solid residue, which was purified via column chromatography on silica gel eluting with 1:2 hexane:dichlorometane. Compound **1** was thus obtained as a white waxy solid in 37% yield (277 mg). ^{1}H-NMR (400 MHz, CDCl$_3$, ppm): δ 8.07 (2 H, d, J = 8.4 Hz, Ph*H*), 7.66 (2H, d, J = 8.4 Hz, Ph*H*), 7.56 (1H, dd, J = 2.57, 1.8 Hz, Th*H2*), 7.42 (2H, m, Th*H4+5*), 4.37 (2H, q, J = 7.2 Hz, OC*H$_2$*CH$_3$), 1.41 (3H, t, J = 7.2 Hz, OCH$_2$C*H$_3$*). MS (ESI): m/z [M+H$^+$] 233.4, calcd m/z [M+H$^+$] 233.31; [M+Na$^+$] 255.3, calcd m/z [M+Na$^+$] 255.29.

2,5-Dibromo-3-(4-ethylbenzoate)-thiophene (**11**). A solution of **1** (250 mg, 1.07 mmol) in dry DMF (10 ml), protected from light exposure with an aluminium foil, was treated with NBS (478 mg, 2.7 mmol) at room temperature. The reaction mixture was stirred for 6 h and then poured into water (30 ml). After extraction with Et$_2$O (2 x 20 ml), the organic layers were combined, dried (Na$_2$SO$_4$), filtered and concentrated. Purification through column chromatography (silica gel, 1:1 hexane/CH$_2$Cl$_2$) gave **2** as a light yellow solid in 88% yield (367 mg). ^{1}H-NMR (400 MHz, CDCl$_3$, ppm): δ 8.09 (2 H, d, J = 8.4 Hz, Ph*H3,5*), 7.56 (2H, d, J = 8.4 Hz, Ph*H2,6*), 7.04 (1H, s, Th*H4*), 4.40 (2H, q, -OC*H$_2$*), 1.41 (3H, t, -C*H$_3$*).

(4-Ethoxycarbonyl)3-phenyl-3',3''-dihexyl-2,2':5',2''-terthiophene (**12**). Compound **2** (365 mg, 0.93 mmol) was dissolved in argon degassed DME/H$_2$O mixture (40 ml/20 ml). K$_2$CO$_3$ (905 g, 6.55 mmol) was then added, together with Pd(PPh$_3$)$_4$ (107 mg, 0.09 mmol). The mixture was stirred at room temperature for 15 min, then treated with 3-hexylthiophene-2-boronic acid pinacol ester (684 mg, 2.3 mmol) and heated up to reflux temperature. Heating was carried under an argon

atmosphere for 8 h, whereupon the solution was allowed to reach room temperature. It was then transferred to a separator funnel, together with water (25 ml) and diethyl ether (40 ml) and, after vigorous shaking, phases were separated and the aqueous phase was extracted once more with Et$_2$O (20 ml). Organics were combined, dried (Na$_2$SO$_4$), filtered and concentrated, to leave a yellowish oily residue, which was subsequently charged on a silica gel column and eluted with 1:1 petroleum ether:CH$_2$Cl$_2$. The pure product was isolated as light yellow dense oil in 31% yield (163 mg). ^{1}H-NMR (400 MHz, CDCl$_3$, ppm): δ 7.95 (2 H, d, J = 8.4 Hz, Ph$H3,5$), 7.36 (2H, d, J = 8.4 Hz, Ph$H2,6$), 7.27 (1H, d, J = 5.3 Hz, Th$H5'$), 7.24 (1H, s, Th$H4$), 7.2 (1H, d, J = 5.3 Hz, Th$H5''$), 6.96 (1H, d, J = 5.3 Hz, Th$H4'$), 6.88 (1H, d, J = 5.3 Hz, Th$H4''$), 4.37 (2H, q, J = 7.2 Hz, -OCH_2), 2.82 (2H, t, J = 8 Hz, ThCH_2'), 2.29 (2H, t, J = 8 Hz, ThCH_2''), 1.79-1.65 (2H, m, ThCH$_2$CH_2), 1.38 (3H, t, J = 7.2 Hz, OCH$_2$CH_3), 1.31-1.11 (14H, m, -CH_2-), 0.88-0.8 (6H, m, -CH_3). ^{13}C-NMR (100.8 MHz, CDCl$_3$, ppm): δ 166.2, 142.2, 140.5, 140, 139.7, 136.8, 130.9, 130, 129.9, 129.6, 128.9, 128.1, 127.2, 126, 124, 60.7, 31.6, 31.5, 30.6, 29.9, 29.2, 29.1, 29, 28.7, 22.5, 22.4, 14.2, 13.9. MS (ESI): m/z [M+H$^+$] 565.3, calcd m/z for [M+H$^+$] 565.87; [M+Na$^+$] 587.2, calcd m/z for [M+Na$^+$] 587.85.

Poly[(4-ethoxycarbonyl)3-phenyl-3',3''-dihexyl-2,2':5',2''-terthiophene] (**4-CO$_2$EtPh-PHTT**). Cu(ClO$_4$)$_2$·6H$_2$O (189 mg, 0.51 mmol) was dissolved in acetonitrile (20 ml) and added dropwise over a period of 20 min to a solution of **3** (107 mg, 0.19 mmol) in acetonitrile (20 ml), kept at 55 ^{o}C under an argon atmosphere. The solution turned immediately dark and stirring was carried out for other 2 h at this temperature. A black powder formed, which, after cooling down to room temperature, was filtered and washed thoroughly with acetonitrile until washings were

colorless. The dark powder was then suspended in 30% w/w NH_3 solution (20 ml), further diluted with water (10 ml), and stirred vigorously for 2 h in order to induce a complete de-doping of the polymeric material. The suspension was transferred to a separator funnel and the de-doped polymer was extracted in chloroform (60 ml). The dark red organic phase was then neutralized with 0.1 M HCl (checked with pH incator), dried (Na_2SO_4), filtered and concentrated to almost 15 ml. MeOH (30 ml) was added to induce precipitation of the polymer and the suspension was left standing overnight in the dark to allow the complete deposition of the floating solid. The day after it was filtered directly in a Soxhlet thimble and subjected to Soxhlet extraction with methanol, diethyl ether and chloroform. The chloroform fraction was concentrated to almost 10 ml and methanol (30 ml) was added to precipitate the purified polymer. The resulting dark solid was collected on a glass filter, washed with methanol and dried in vacuo (83 mg, 78% yield). ^{1}H-NMR (400 MHz, $CDCl_3$, ppm): δ 8.01 (2 H, d, J = 8.2 Hz, Ph$H3,5$), 7.36 (2H, d, J = 8.2 Hz, Ph$H2,6$), 7.29 (1H, s, Th$H4$), 7.06-6.95 (2H, m, Th$H4,4''$), 4.38 (2H, q, J = 7.2 Hz, -OCH_2), 2.81 (2H, br s, ThCH_2'), 2.28 (2H, br s, ThCH_2''), 1.71 (2H, br s, ThCH$_2$CH_2), 1.42 (3H, t, J = 7.01 Hz, -OCH$_2$CH_3), 1.36-1.16 (14H, m, -CH_2-), 0.9 (3H, br s, -CH_3'), 0.85 (3H, br t, J = 3Hz, -CH_3'').

Methods

UV−visible absorption spectra were recorded on a Cary 5000 spectrophotometer (Varian).

DSC scans were obtained on a Mettler Toledo 823E apparatus working under N_2 flow (20 ml min^{-1}). Polymer samples were sealed into standard aluminium pans, equilibrated at 0 °C, heated to 280 °C at a rate of 20 °C min^{-1} and then cooled down again at the maximum rate to 0°C, in order

to eliminate thermal histories. Reheating was then carried out at 10 °C min^{-1} to observe polymers thermal behavior.

The photovoltaic cells were prepared as follow. Fluorine doped tin oxide (FTO) coated glass substrates (15 Ω/sq Pilkington) were etched with zinc powder and HCl (2.4 M) in water solutionto define the required pattern for the devices bottom electrode. Careful washing of the substrates following the etching step was performed with soap (Hellmanex 2% in water), bidistilled water, acetone and isopropanol. Oxygen plasma treatment was finally performed for 5' to remove last traces of organic residues. Substrates were then covered with compact TiO$_2$ layer of a thickness comprised between 150 and 200 nm. Deposition of the compact layer was carried on by spray pyrolysis at 500 ºC with oxygen as the carrier gas, starting from a 1:10 by volume titanium diisopropoxide bis(acetylacetonate):ethanol solution. The commercial Dyesol TiO$_2$ paste (DSL 18NR-T), previously diluted in ethanol and ultrasonicated until complete mixing, was doctor-bladed by hand onto the TiO$_2$ compact layer coated FTO substrates to get a mesoporous TiO$_2$ film of an average thickness of 1 μm. The substrates were then slowly heated to 550 ºC (ramped over 1 ½ hours) and baked at this temperature for 30' in air. After cooling, substrates were soaked in TiCl$_4$ solution (15 mM in water) and oven-baked for 1 hour at 70ºC. After oven-baking, substrates were rinsed with bidistilled water, dried in air and baked again at 550 ºC for 45'. In the case of samples with **4-CO$_2$EtPh-P3HT** and P3HT as polymer donor components, substrate were re-heated at 200 ºC and then cooled down to 70 ºC right before spin coating the polymers, in order for the mesoporous TiO$_2$ layer to expel residual water. The donor polymers were spin-coated onto the substrates at 1000 rpm for 60'' from a 30 mg/ml chlorobenzene solution. Spin coater rotation was activated 15

107

seconds after dispensing the solution onto the substrate in order to promote effective polymer infiltration inside the mesoporous TiO_2 layer. In the case of the device provided with **4-CO$_2$EtPh-P3HT** interlayer, after cooling down to 70 ºC, the substrate was immersed in a 15 mg ml^{-1} solution of **4-CO$_2$EtPh-P3HT** in chloroform for several hours (~20 h). Immersion was followed by thorough rinsing with pure chloroform, until washings were colorless. P3HT was then spin-coated in the same way as described previously. Finally, 80 nm thick silver electrodes were thermally evaporated under high vacuum (10-6 mbar) onto the samples through a suitable shadow mask defining a device active area of ~2 x 4.5 mm2. Where scheduled, thermal annealing of samples at 130 ºC for 30' in inert N2 atmosphere was performed following metal electrode evaporation. Current density/Voltage (J-V) characteristics were measured by a Keithley model 2400 digital source-meter exposing the cell to class AAA Newport Air Mass 1.5 Global (AM 1.5 G) full spectrum solar simulator. The power of incoming radiation was set at 100 mW cm^{-2} using a NREL calibrated silicon solar cell.

References

[1] (a) Kim, Y.G.; Walker, J.; Samuelson, L.A.; Kumar, J. *Nano Lett.*, **2003**, *3*, 323-325. (b) Lohwasser, R.H.; Bandara, J.; Thelakkat, M. *J. Mater. Chem.*, **2009**, *19*, 4126-4130. (c) Fang, Z.; Eshbaugh, A. A.; Schanze, K. S. *J. Am. Chem. Soc.*, **2011**, *133*, 3063–3069. (d) Liu, J.; Kadnikova, E. N.; Liu, Y.; McGehee, M. D.; Fréchet, J. M. J. *J. Am. Chem. Soc.,* **2004**, *126*, 9486–9487. (e) Liu, Y.; Scully, S. R.; McGehee, M. D.; Liu, J.; Luscombe, C. K.; Fréchet, J. M. J.; Shaheen, S. E.; Ginley, D. S. *J. Phys. Chem. B*, **2006**, *110*, 3257–3261. (f) Mwaura, J. K.; Zhao, X.; Jiang, H.; Schanze, K. S.; Reynolds, J. R. *Chem. Mater.* **2006**, *18*, 6109–6111. (g) Krüger, R.A.; Gordon, T.J.; Baumgartner, T.; Sutherland, T.C. *Appl. Mat. Interfaces*, **2011**, *3*, 2031-2041. (h) Oosterhout, S.D.; Koster, L.J.A.; van Bavel, S.S, Loos, J.; Stenzel, O.; Thiedmann, R.;

Schmidt, V.; Campo, B.; Cleij, T.J.; Lutzen, L.; Vanderzande, D.; Wienk, M.M.; Janssen, R.A.J. *Adv. Energy Mater.*, **2011**, *1*, 90-96.

[2] Hagfeldt, A.; Boschloo, G.; Sun, L.; Kloo, L.; Pettersson, H. *Chem. Rev.*, **2010**, *110*, 6595-6663.

[3] An, B.-K.; Hu, W.; Burn, P. L.; Meredith, P. *J. Phys. Chem. C*, **2010**, *114*, 17964–17974.

[4] Wang, Z.-S.; Li, F.-Y.; Huang, C.-H. *Chem. Commun.*, **2000**, 2063–2064.

[5] Brennan, B. J.; Keirstead, A. E.; Liddell, P. A.; Vail, S. A.; Moore, T. A.; Moore, A. L.; Gust, D. *Nanotechnology*, **2009**, *20*, 505203.

[6] Park, H.; Bae, E.; Lee, J.-J.; Park, J.; Choi, W. *J. Phys. Chem. B*, **2006**, *110*, 8740–8749.

[7] Schenk, R.; Gregorius, H.; Meerholz, K.; Heinze, J.; Müllen, K. *J. Am. Chem. Soc.*, **1991**, *113*, 2634-2637.

[8] Miyasaka, M.; Yamazaki, T.; Tsuchida, E.; Nishide, H. *Macromolecules*, **2000**, *33*, 8211–8217.

[9] Cravino, A.; Zerza, G.; Maggini, M.; Bucella, S.; Svensson, M.; Andersson, M. R.; Neugebauer, H.; Sariciftci, N. S. *Chem. Commun.*, **2000**, 2487–2488.

[10] (a) De Girolamo, J.; Reiss, P.; Pron, A. *J. Phys. Chem. C*, **2007**, *111*, 14681–14688. (b) Xue, C. H.; Luo, F. T.; Liu, H. Y. *Macromolecules*, **2007**, *40*, 6863–6870.

[11] Xie, C. P.; Lahti, P. M. *J. Polym. Sci., Polym. Chem.*, **1999**, *37*, 779–788.

[12] (a) Li, Y.N.; Vamvounis, G.; Holdcroft, S. *Macromolecules*, **2001**, *34*, 141-143. (b) Li, Y.N.; Vamvounis, G.; Holdcroft, S. *Macromolecules*, **2002**, *35*, 6900-6906. (c) Liu, J.; McCullough, R.D. *Macromolecules*, **2002**, *35*, 9882-9889.

[13] Monson, T.; Lloyd, M.; Olson, D.; Lee, Y.; Hsu, J. *Adv. Mater.*, **2008**, *20*, 4755.

[14] Lloyd, M.T.; Prasankumar, R.P.; Sinclair, M.B.; Mayer, A.C.; Olson, D.C.; Hsu, J.W.P. *J. Mater. Chem.*, **2009**, *19*, 4609-4614.

[15] (a) Han, Z.; Zhang, J.; Yang, X.; Zhu, H.; Cao, W. *Sol. Energy Mater. Cells*, **2010**, *94*, 755-760. (b) Han, Z.; Zhang, J.; Yang, X.; Zhu, H.; Cao, W. *Org. Elec.*, **2010**, *11*, 1449-1460.

[16] Baurle, P.; Würthner, F.; Heid, S. *Angew. Chem., Int. Ed. Engl.*, **1990**, *29*, 419-421.

[17] Pomerantz, M.; Liu, L.M.; Zhang, X.S. *ARKIVOC*, **2003**, *12*, 119-137.

[18] Zhai, L.; Pilston, R.L.; Zaiger, K.L.; Stokes, K.K.; McCullough, R.D. *Macromolecules*, **2003**, *36*, 61-64.

[19] Lanzi, M.; Paganin, L. *React. Funct. Polym.*, **2010**, *70*, 346-360.

[20] Li, M.; Xu, P.; Yang, J.; Yang, S. *J. Mater. Chem.*, **2010**, *20*, 3953-3960.

[21] Oosterhout, S.D.; Koster, L.J.A.; van Bavel, S.S, Loos, J.; Stenzel, O.; Thiedmann, R.; Schmidt, V.; Campo, B.; Cleij, T.J.; Lutzen, L.; Vanderzande, D.; Wienk, M.M.; Janssen, R.A.J. *Adv. Energy Mater.*, **2011**, *1*, 90-96.

[22] Augeri, D. J.; Baumeister, S. A.; Bruncko, M.; Dickman, D. A.; Ding, H.; Dinges, J.; Fesik, S. W.; Hajduk, P. J.; Kunzer, A. R.; McClellan, W. *U.S. Pat. Appl. Publ.*, **2002**, US 20020086887.

CHAPTER 4

Role of Molecular Configuration on the Performance of Novel Functionalized Oligothiophenes as Interlayers in Hybrid Solar Cells

4.1 Introduction

In the framework of hybrid solar cells, one of the most appealing properties of interfacial modifiers is the possibility to create a distribution of electric dipoles,[1] capable of affecting the alignment between the energy levels of the organic functional material and the oxide. In hybrid solar cells, this would result in reduction of the energy barrier for charge injection and/or reduction of the charge recombination rate at the interface (see Chapter 1, section 1.3.4).

Pyridine derivatives are often used as interface modifiers. The use of 4-*tert*-butylpyridine (*t*-BPy) was first introduced in DSSCs.[2] They were devised to "protect" portions of the TiO_2 surface, left uncovered by the larger dye molecules. However, it was recognized that the t-BPy molecules are also able to induce band bending at the oxide surface.[3]

As a variation to previous attempts, Canesi *et al.* reported a noteworthy increase in the performance of a hybrid device based on a porous TiO_2 matrix, obtained by functionalizing the oxide surface with commercially available, optically inert 4-mercaptopyridine (4-MPy) molecules (Figure 4.1).[4]
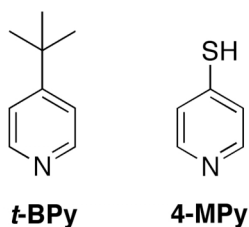
Figure 4.1. Chemical structure of 4-*tert*-butylpyridine (*t*-BPy) and 4-mercaptopyridine (4-MPy) molecules.

The improvement in the efficiency of that solar cell was mainly attributed to morphological reasons, *i.e.*, to an increase of the coverage of

112

the oxide pore walls by the P3HT chains and to an enhancement in the ordering of the first polymer chains lying on the hybrid interface upon 4-MPy adsorption on the metal oxide surface. Atomistic simulation furnished a possible scenario for the interfacial situation, in which the 4-MPy molecules are bound to the TiO_2 surface via the nitrogen atoms and the free thiol groups, directed towards the P3HT side, provide a smooth potential landscape for its diffusion, thus increasing the ordered adhesion of the polymer to the interface.

Based on this finding, the need for an extension of the local order achieved at the hybrid interface to further adjacent polymer layers arises as a fundamental requirement for future improvements in nc-TiO_2/P3HT hybrid devices performances.

In this contest, a series of novel interlayer structures, based on the 4-MPy structure, was devised and is presented here for the first time, together with the results obtained from their effective use on nc-TiO_2/P3HT hybrid solar cells. The 4-pyridil moiety is maintained in these derivatives, with the aim of ensuring the interlayer binding to the metal oxide surface, whereas the free thiol groups are replaced with thienyl moieties, also bearing alkyl side-chains, aimed at inducing supramolecular ordering of the conjugated polymer onto the hybrid interface (Figure 4.2).
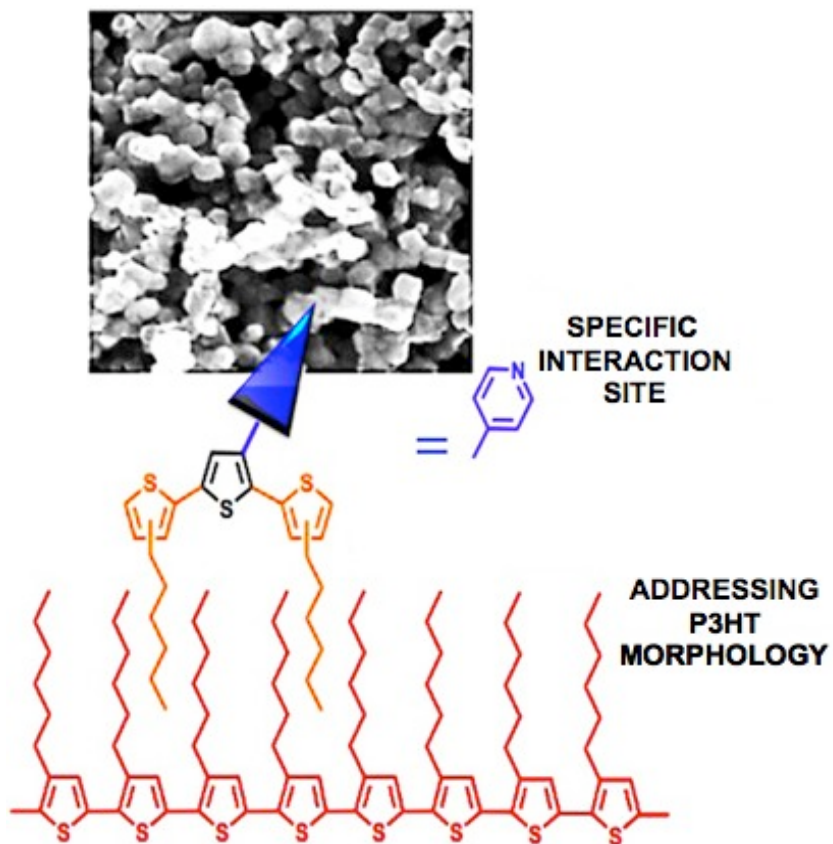
Figure 4.2. Schematic representation of the double role played by the novel 4-pyridil functionalized oligothiophene interlayers presented in this work at the interface between the P3HT layer and the mesoporous TiO_2 matrix.

4.2 Results and discussion

4.2.1 Synthesis of the functionalized oligothiophene interlayers

The synthesis of the 4-pyridil functionalized oligothiophene derivatives, to be tested as interlayers in hybrid nc-TiO_2/P3HT solar cells, is reported in Scheme 4.1.

114
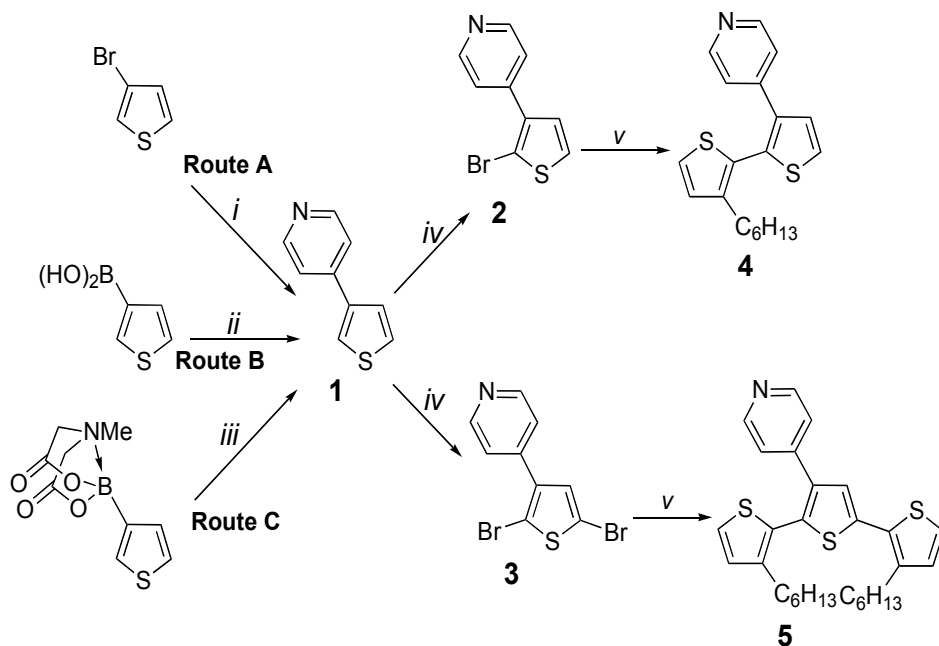
Scheme 4.1. Synthetic routes to yield 4-pyridil functionalized thiophene **1**, bithiophene **4** and terthiophene **5**. *Reagents and conditions: i)* 4-pyridilboronic acid, Pd(PPh$_3$)$_4$, K$_2$CO$_3$, DME/H$_2$O, Δ; *ii)* 4-iodopyridine, Pd(PPh$_3$)$_4$, K$_2$CO$_3$, DME/H$_2$O, Δ; *iii)* 4-iodopyridine, Pd(OAc)$_2$, S-Phos, K$_3$PO$_4$, dioxane/H$_2$O, Δ; *iv)* NBS, AcOH; *v)* 3-hexylthiophene-2-boronic acid pinacol ester, Pd(PPh$_3$)$_4$, K$_2$CO$_3$, DME/H$_2$O, Δ.

The compounds were obtained through subsequent Suzuky type cross-couplings of suitable halide and boronic acid aromatic substrates. The preparation of **1** was attempted by following three different procedures, in order to determine the best conditions for the obtainment of the 4-pyridil functionalized thiophene scaffold. Aside from classical Suzuky couplings, employing boronic acids, the use of a MIDA boronate reagent was also attempted. These building blocks were reported quite recently as valuable alternatives to classical boronic acids.[5] They are employed in combination with potassium phosphate as a base in dioxane/water mixtures at 80 °C, thus promoting the slow but continuous release of free-boronic acids and preventing their decomposition before cross-

115

coupling. Unfortunately, in the present case a significant increase in reaction yield was not observed with the use of 3-thiophene boronic acid MIDA ester and 4-iodopyridine (**Route C**) in substitution of 3-thiophene boronic acid (**Route B**), but resulted instead in a slight decrease, from 73% to 61%. The small difference in the two yields might change anyway by testing some modifications in the procedure employing the boronic acid MIDA ester, either in the reactants or in the temperature/solvent/time parameters, which could lead to its significant improvements. It is worth noting that both **Route B** and **C** proceeded better than **Route A**, which employed 3-bromothiophene and 4-pyridil boronic acids as the starting materials.

Starting from **1**, longer oligothiophenes were synthesized, through selective bromination steps followed by Suzuky couplings with a 3-hexylthiophene-2-boronic ester derivative: in particular, 2,2'-bithiophene **4**, in which the 4-pyridil and hexyl chain substituents are disposed in HH configuration, being attached respectively to the 3- and 3'-positions of the two adjacent thienyl rings and 2,2':5',2''-terthiophene **5** were obtained.

Compound **7**, a regioisomer of **4** in which the 4-pyridil moiety was displaced to the 4-position of the thienyl ring, thus resulting in HT configuration with respect to the hexyl chain, was obtained as reported in Scheme 4.2. The total selectivity of the Pd(0) catalyst for the bromine substituent in the 2-position of 2,4-dibromothiophene afforded **6** as the main product. The subsequent cross-coupling step could therefore be addressed to the remaining bromine atom in the 4-position, leading to the obtainment of **7** as the only product.
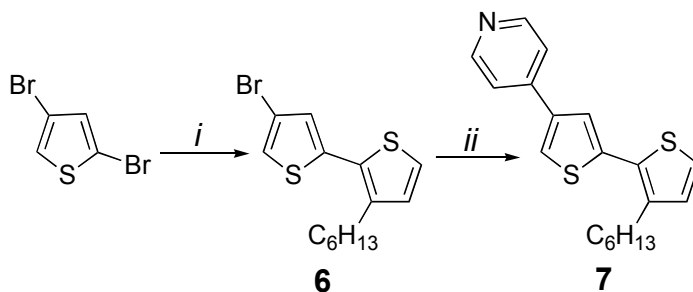
Scheme 4.2. Synthesis of 4-pyridil functionalized bithiophene **7**. *Reagents and conditions: i)* 3-hexylthiophene-2-boronic acid pinacol ester, Pd(PPh₃)₄, K₂CO₃, DME/H₂O, Δ; *ii)* 4-pyridilboronic acid, Pd(PPh₃)₄, K₂CO₃, DME/H₂O, Δ.

The synthesis of compound **8**, a regioisomer of compound **1** characterized by a different position of the nitrogen atom in the pyridil ring, and of the bi- and terthiophene derivatives **11** and **12**, is reported in Scheme 4.3. Three different procedures were used also in this case for the obtainment of the thiopyridine precursor **8**, with slightly different outcomes in comparison with those obtained for the preparation of **1**. The MIDA boronate route furnished the best yield in **8**, confirming the good results obtained in previous literature for the use of these building blocks in substitution of classical boronic acids.

Furthermore, compound **13**, another regioisomer of compound **1** in which the 4-pyridyl moiety is displaced in the 2-position of the thienyl ring, has been synthesized (Scheme 4.4). Also in this case three different synthetic routes have been tested and **Route C** has given the best result.

It is well known, mainly from studies of photocatalysis, that the anatase TiO₂ surface presents two different sites for potential interaction with adsorbed species,[9] namely Lewis acid sites, constituted by Ti(IV) moieties missing of one ligand from the octahedral coordination sphere, and Broensted basic sites, *i.e.*, free hydroxyl (-OH) groups extending out of the surface. For this reason, the synthesis of carboxylic acid
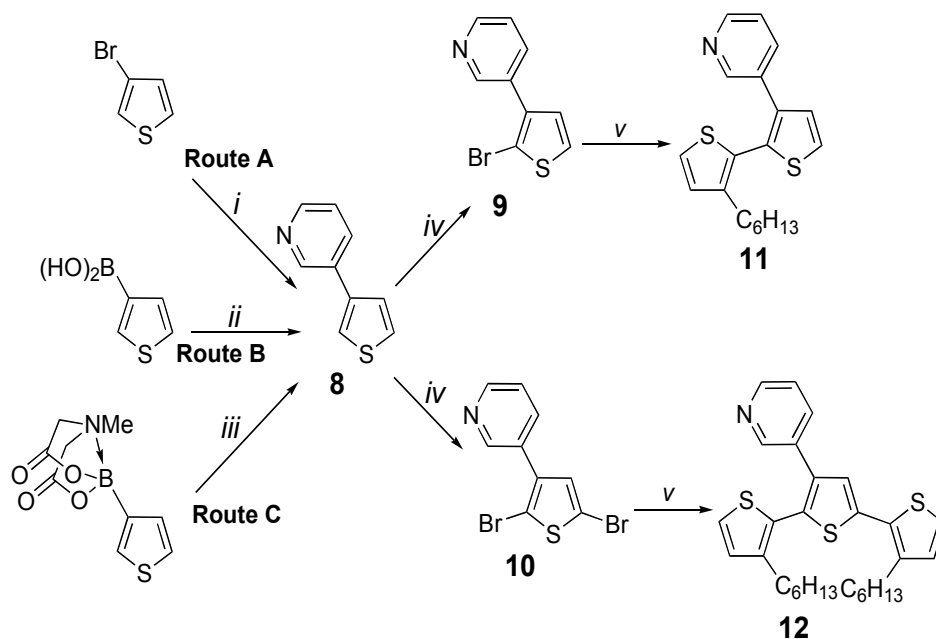
Scheme 4.3. Synthesis of 3-pyridil functionalized thiophene **8**, bithiophene **11** and terthiophene **12**. *Reagents and conditions: i)* 3-pyridilboronic acid, Pd(PPh₃)₄, K₂CO₃, DME/H₂O, Δ; *ii)* 3- or 4-iodopyridine, Pd(PPh₃)₄, K₂CO₃, DME/H₂O, Δ; *iii)* 3-iodopyridine, Pd(OAc)₂, S-Phos, K₃PO₄, dioxane/H₂O, Δ; *iv)* NBS, AcOH; *v)* 3-hexylthiophene-2-boronic acid pinacol ester, Pd(PPh₃)₄, K₂CO₃, DME/H₂O, Δ.

functionalized thiophene, bithiophene and terthiophene derivatives has been envisaged, in order to test the difference of this last type of substitution with respect to the basic one, represented by the aforementioned pyridyl derivatives. It is worth to underline here again that the carboxylic acid moiety is the most commonly encountered type of chemical fuctionalization employed for dye-photosenstizers in DSSCs.

118
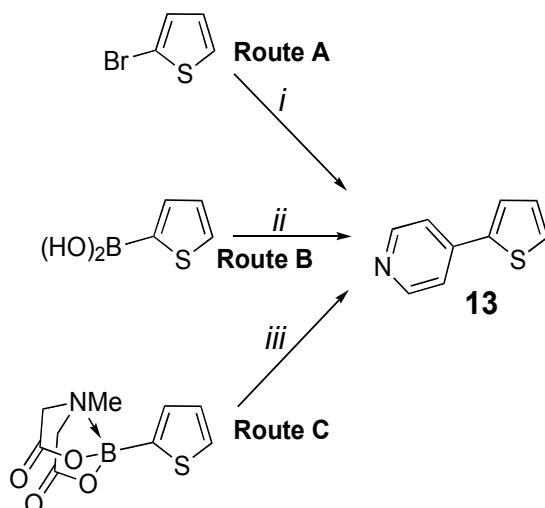
Scheme 4.4. Synthesis of 4-pyridil functionalized thiophene **13**. *Reagents and conditions: i)* 3-pyridilboronic acid, Pd(PPh$_3$)$_4$, K$_2$CO$_3$, DME/H$_2$O, Δ; *ii)* 3- or 4-iodopyridine, Pd(PPh$_3$)$_4$, K$_2$CO$_3$, DME/H$_2$O, Δ; *iii)* 3-iodopyridine, Pd(OAc)$_2$, S-Phos, K$_3$PO$_4$, dioxane/H$_2$O, Δ.

Scheme 4.5 reports the details about the synthesis of the carboxylated oligothiophenes **14**, **20** and **21**. Whereas thiophene derivative **14** was obtained directly in one step, access to bithiophene and terthiophene derivatives **20** and **21** has required the previous protection of the carboxylic acid moiety in the form of ethyl ester in order to perform the bromination and subsequent Suzuky coupling step, followed by final hydrolysis of the ester group into a free carboxylic acid. The synthesis of the ethyl ester functionalized precursor **15** has been carried out *via* the usual three procedures already reported for the preparation of compounds **1**, **8** and **13**. The MIDA boronate route furnished again the best result, affording **15** in very good yield.
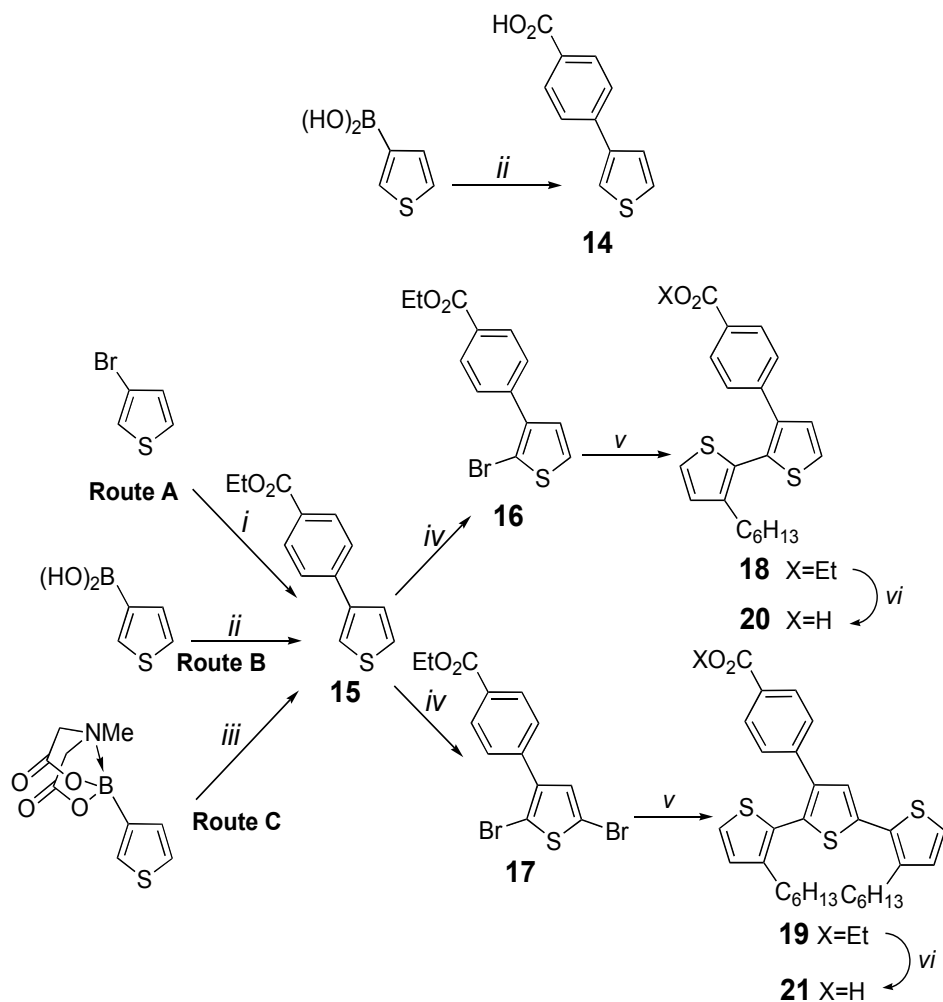
Scheme 4.5. Synthetic routes to yield 4-carboxyphenyl functionalized thiophene **14**, bithiophene **20** and terthiophene **21**. *Reagents and conditions: i)* 4-ethoxycarbonylphenylboronic acid, Pd(PPh$_3$)$_4$, K$_2$CO$_3$, DME/H$_2$O, Δ; *ii)* 4-bromobenzoic acid or 4-bromobenzoic acid ethyl ester, Pd(PPh$_3$)$_4$, K$_2$CO$_3$, DME/H$_2$O, Δ; *iii)* 4-bromobenzoic acid ethyl ester, Pd(OAc)$_2$, S-Phos, K$_3$PO$_4$, dioxane/H$_2$O, Δ; *iv)* NBS, DMF; *v)* 3-hexylthiophene-2-boronic acid pinacol ester, Pd(PPh$_3$)$_4$, K$_2$CO$_3$, DME/H$_2$O, Δ; *vi)* KOH, THF/ H$_2$O, Δ.

120

Table 4.1 summarizes the yields obtained for the synthesis of functionalized thiophene derivatives **1**, **8**, **13** and **15** using the three different synthetic routes.

Table 4.1. Reaction yields for the synthesis functionalized thiophene derivatives using the three different routes **A**, **B** and **C**.

Compound	Route A (yield%)	Route B (yield%)	Route C (yield%)
1	36	73	61
8	44	63	70
13	64	55	68
15	37	72	87

4.2.2 Characterization of the functionalized oligothiophene interlayers

The oligothiophenes derivatives were initially characterized by UV-visible absorption spectroscopy. Comparative absorption spectra are shown separated for groups of derivatives bearing the three different functionalities, namely the 4-pyridyl, 3-pyridyl and 4-carboxyphenyl functionalities.

The UV-visible absorption spectra in chloroform solutions of the 4-pyridil functionalized thiophene, bithiophene and terthiophene derivatives **1**, **4**, **5**, **7** and **13** are reported in Figure 4.3, together with the spectrum of the un-functionalized symmetrical species 3,3''-dihexyl-2,2':5',2''-terthiophene (see Chapter 2 for chemical structure). All the derivatives present absorption maxima in the UV-region, therefore ensuring optical transparence in the region where the polymer absorb, when used as interlayers in hybrid solar cells. A significant blue-shift is observed in the spectrum of functionalized terthiophene **5** if compared to the un-functionalized 3,3''-dihexyl-2,2':5',2''-terthiophene model. The presence of the bulky 4-pyridyl substituent on the central thienyl ring

Figure 4.3. UV-visible absorption spectra in chloroform solutions of **1** (black line), **4** (red line), **5** (blue line), **7** (green line), **13** (magenta line) and 3,3''-dihexyl-2,2':5',2''-terthiophene (purple line).

causes a distortion of the main conjugated terthiophene chain. The inter-ring distortion between the adjacent thienyl moieties is also evident by comparing the absorption maxima of the functionalized bithiophene **4** and **7** and of functionalized thiophene **1**. The highest bathochromic shift is present in the spectrum of **7**, in which the 4-pyridyl substituent is located in β-position with respect to the inter-ring bond, thus preventing the aforementioned distortion. On the contrary, the maximum absorbance in the spectrum of bithiophene **4** is located at an even shorter wavelength than the maximum in the spectrum of simple 3-(4-pyridil)-thiophene **1**, in which π-conjugation may derive only from a coplanar disposition of the thiophene and pyridil rings. Compound **4** is thus characterized by a complete distortion of the inter-ring bonds, regarding both the thiophene-thiophene linkage and the thiophene-pyridine linkage. Finally, the

122

absorption spectrum of compound **13** presents a significant charge-transfer nature, indicating a donor-acceptor character in the compound and a higher extent of π-conjugation with respect to compound **1**. This is further confirmed by acquiring a spectrum of the compound in an apolar solvent like hexane, in which the charge-transfer band disappears and the absorption maximum is blue-shifted with respect to the maximum in chloroform (Figure 4.4).
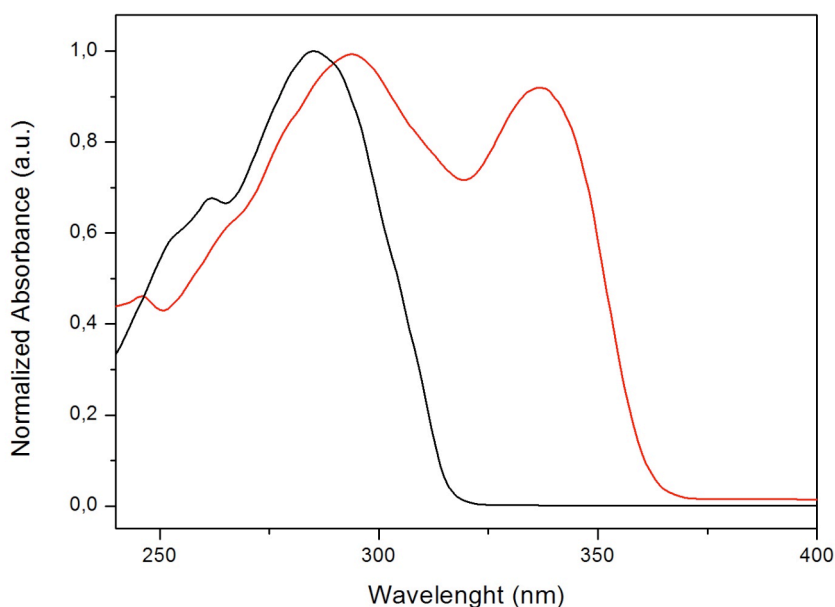
Figure 4.4. UV-visible absorption spectra of **13** in hexane (black line) and chloroform (red line).

For the sake of clarity, it is worth mentioning that the charge-transfer band observed in chloroform solution, might be attributed to a partial protonation of the pyridyl moiety, causing an inversion in the relative energy positions of the nπ* and $\pi\pi$* electronic states. Anyway, the solvent used for acquiring these spectra was taken from a freshly open

bottle of stabilized chloroform for spectroscopy, which should ensure a good quality and low acidity.

The UV-visible absorption spectra of 3-pyridyl functionalized oligothiophenes are reported in Figure 4.5, whereas those of the 4-carboxyphenyl functionalized oligothiophenes are reported in Figure 4.6.
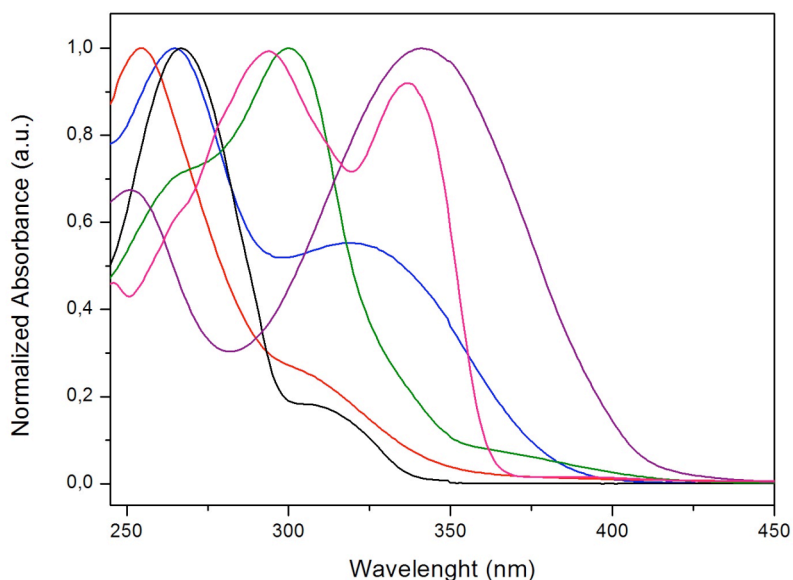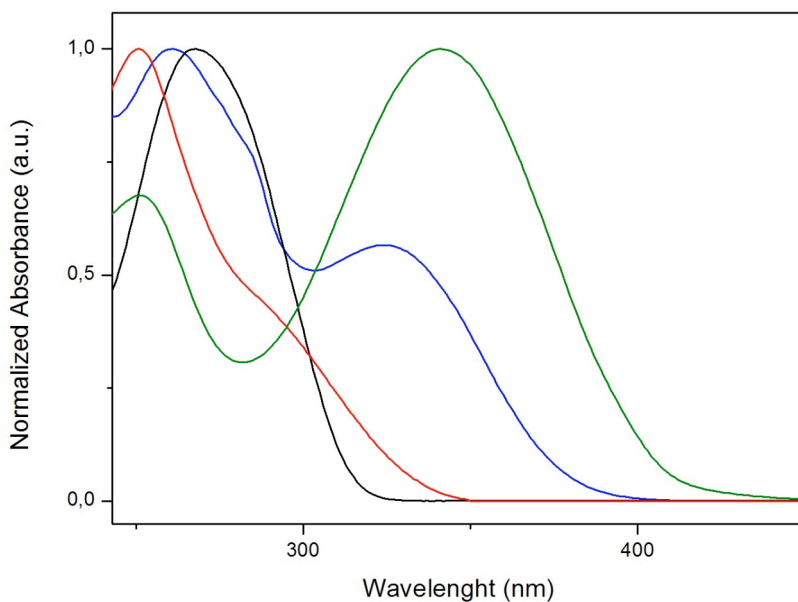

Figure 4.5. UV-visible absorption spectra in chloroform solutions of **8** (black line), **11** (red line), **12** (blue line) and 3,3''-dihexyl-2,2':5',2''-terthiophene (green line).

By looking at the three different series of UV-visible absorption spectra it is possible to evidence how the 4- and 3-pyridyl functionalized oligothiophenes often present two absorption bands, one more intense and a second one of minor but variable intensity, likely attributed to a partial charge-transfer character (see Table 4.2, these bands are named ct or sh, depending on the intensity). This behavior was not evident in the spectra of the 4-carboxyphenyl substituted oligothiophenes and might

124
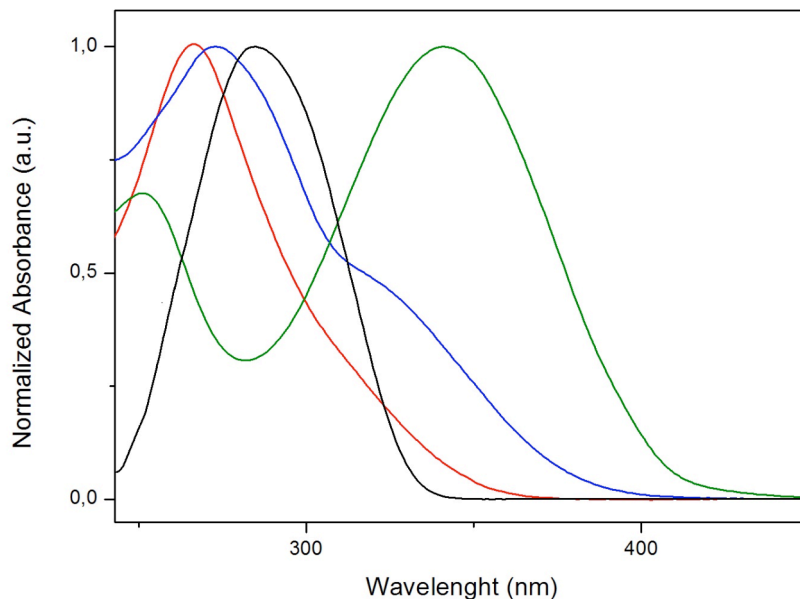
Figure 4.6. UV-visible absorption spectra in chloroform solutions of **14** (black line), **20** (red line), **21** (blue line) and 3,3''-dihexyl-2,2':5',2''-terthiophene (green line).

therefore be attributed to the presence of the pyridyl moiety, which is strongly electron-withdrawing. The absorption maxima relative to the 4-carboxyphenyl functionalized oligothiophenes appear slightly red-shifted with respect to maxima of the analogous 4-pyridyl and 3-pyridyl functionalized ones. This might be attributed to better coplanarity between the thiophene and phenyle moieties in these derivatives with respect to the pyridyl functionalized ones.

Other significant differences from the spectra of the corresponding 4-pyridyl functionalized derivatives are not evident, confirming the influence of the steric demanding functionalities on the degree of thiophene-thiophene inter-ring distorsion.

Table 4.2 furnishes an overview of the absorption properties measured for the all the functionalized oligothiophenes previously reported.

125

Table 4.2. Absorption maxima (λ_{max} abs) and absorption coefficients (ε_{max}) for functionalized thiophene, bithiophene and terthiophenes in chloroform solutions.

Compound	λ_{max} abs (nm)	ε_{max} (mol^{-1}cm^{-1})
1	267	20037
	304 (sh)[a]	3676
4	254	17293
	301 (sh)	4669
5	265	19808
	319 (ct)[b]	10961
7	268 (sh)	15864
	301	22345
8	269	24901
11	250	15863
	291 (sh)	6662
12	261	24388
	325 (ct)	13901
13	295	21385
	338 (ct)	19674
14	286	37947
20	268	19000
21	280	38849
	320 (sh)	19036
3,3''-dihexyl-2,2':5',2''-terthiophene	341	18277

[a] sh=shoulder. [b] ct=charge-transfer

The increase of the absorption coefficients appears generally correlated to the increase of the band gap, as it is reasonable to expect. The only exception is constituted by compound **14**, whose absorption coefficient resulted lower than that of the corresponding functionalized terthiophene, even if the absorption maximum of the former is located at higher wavelength with respect to the latter.

126

The HOMO and LUMO energy levels of the functionalized terthiophene derivatives **5**, **12** and **21** have been determined through a combination of cyclo-voltammetric measurements (see the Experimental section 4.4 for details) and UV-visible absorption data, and compared to the values obtained for unfunctionalized 3,3''-dihexyl-2,2':5',2''-terthiophene. Table 4.3 summarizes the energies of the frontier molecular orbitals of the four derivatives.

Table 4.3. HOMO and LUMO ebergy levels of functionalized terthiophenes **5**, **12** and **21** and unfucntionalized 3,3''-dihexyl-2,2':5',2''-terthiophene

Compound	E_{HOMO} (eV)	E_{LUMO} (eV)	$\Delta E_{HOMO/LUMO}$ (eV)
5	-5.536	-2.27	3.266
12	-5.466	-2.186	3.28
21	-5.506	-2.266	3.24
3,3''-dihexyl-2,2':5',2''-terthiophene	-5.376	-2.302	3.074

The HOMO energies were derived using the Fc^+/Fc couple as a standard according to the following equation:

$$E_{HOMO} (eV) = -e[E_{p,a} (V \text{ vs } Fc^+/Fc) + 4.8(V \, Fc^+/Fc \text{ vs zero})] \qquad (1)$$

where e corresponds to the number of exchanged electrons, while $E_{p,a}$ is the anodic peak potential (taken with the maxima criterion). The energy gaps HOMO-LUMO ($\Delta E_{HOMO/LUMO}$) were estimated from the absorption maxima of the UV-Vis spectra (in eV) and then used to calculate the absolute value of the LUMO energies. It is evident how functionalization causes a general decrease of the HOMO energies for all the three derivatives. The wider gaps, already discussed previously when describing UV-Vis data, are consequent to the displacements of the LUMO orbitals for the functionalized derivatives towards lower energies

with respect to the unfunctionalized terthiophene model compound. Unfortunately it was not possible to obtain electrochemical data for the functionalized bithiophene derivatives since their anodic oxidations occur outside of the active windows for all the solvents tested.

The absence of planarity in the ground-state molecular conformation of **4** evicted from UV-visible spectroscopy was further confirmed by crystal structure determination through x-ray diffraction analysis. The structure was solved at 100 K by Dr. J.M. Rujas, at CNST-IIT@Polimi. Figure 4.7 reports two images of the molecular structure of **4** at the solid state. The dihedral angle between the 4-pyridil and thiophene rings and between the two adjacent thiophenes are 40.7° and 88.61° respectively, confirming the predictions.
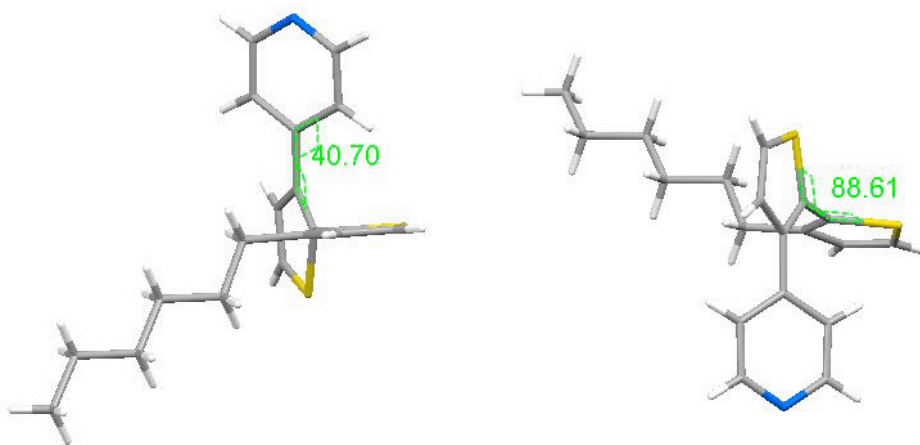
Figure 4.7. Two different views of the molecular structure of **4**.

From the analysis of the solid-state packing features it is evident that crystalline organization is ensured by the inter-digitation of the hexyl side-chains, driven by hydrophobic interactions. A hydrogen-bonding network builds among the nitrogen atoms of the 4-pyridil substituents

128

and the residual water molecules remaining from solution crystallization also occurs (Figure 4.8).
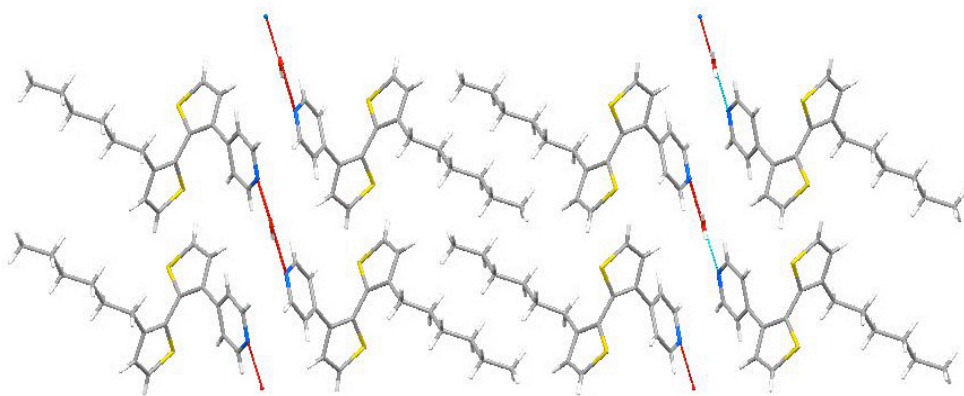
Figure 4.8. Crystal packing of **4** along the *b*-axis.

Table 4.4 reports the main information relative to crystal structure determination of compound **4**.

Table 4.4. Crystallographic information and structure refinement for compound **4**.

Formula	$C_{19}H_{14}NOS_2$
F_W	336.43
Crystal system	Monoclinic
Space group	$C2/c$
a (Å)	14.791(2)
b (Å)	5.6149(10)
c (Å)	42.057(7)
α (deg)	90.00
β (deg)	93.604(12)
γ (deg)	90.00
V (Å^3)	3486.0(10)
T (K)	100(2)
Z	8
F (000)	1400
ρ_{calcd} (g cm^{-3})	1.282
μ (mm^{-1})	2.785
T_{min}, T_{max}	0.7347, 0.9088
Crystal size (mm^3)	0.12×0.08×0.04
θ_{max} (deg)	68.33
No. Refl. collected	9656
R_{int}	0.0460
No.unique	3037
No. with $I> 2\sigma(I)$	2516
Refined parameters	209
Restraints	-
Final R indices [$I> 2\sigma(I)$]	$R1 = 0.0843$, $wR2 = 0.1510$
R indices (all data)	$R1 = 0.0606$, $wR2 = 0.1392$
$\Delta\rho$ [eÅ^{-3}]	-0.368, 0.403

130

4.2.3 Use of the functionalized oligothiophene interlayers in nc-TiO$_2$/P3HT hybrid solar cells.

The pyridil functionalized oligothiophenes were tested as interlayers in nc-TiO$_2$/P3HT hybrid solar cells. Device preparation and evaluation of the related photovoltaic performances were carried out at CNST-IIT@Polimi by Ing. S. Guarnera and Dr. Ing. M. Binda. Mesoporous films of the standard TiO$_2$ paste were immersed in interlayer solutions before P3HT deposition. The concentration of the solutions employed for TiO$_2$ sensitization were analogous to the ones used for dye loading in DSSCs.

As a first step, the derivative having the simplest molecular structure was chosen as interlayer, namely 3-(4-pyridil)-thiophene **1**. Its performance was compared with the one resulting from the use of its regioisomer **8** and with that of 4-thiophene-3-yl-benzoic acid **14**. The photovoltaic responses obtained with the use of these derivatives as interfacial modifiers in nc-TiO$_2$/P3HT hybrid devices are reported in Figure 4.9, together with the response obtained from a control device without any interfacial modification prepared under the same conditions.

Table 4.5 reports the photovoltaic parameters obtained for the hybrid devices. Two main conclusions may be derived from the present results. One is related to the influence on final device performance of the type of chemical moiety addressing the interaction of the interlayer with the titania surface. Indeed, for this particular type of interlayer, the carboxylic acid moiety appears detrimental for the improvement of device performance, while the pyridine moiety has a more beneficial effect. Such a pronounced difference in device performance when going from pyridil interlayer **1**, bearing a basic site for the interaction with TiO$_2$, to benzoic acid interlayer **14**, might therefore derive from their

131
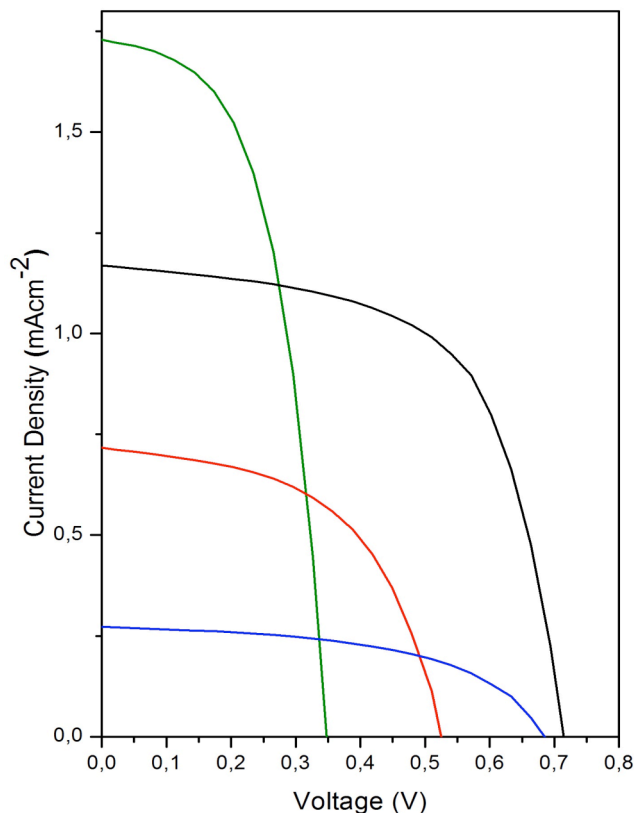
Figure 4.9. Current-voltage characteristics of nc-TiO$_2$/P3HT hybrid solar cells with different interfacial modifiers. **1** (black line), **8** (red line), **14** (blue line) and no-interlayer (green line). The P3HT employed here had M$_W$=20100, PD=1.7 and RR=95.3%.

different displacements on the titania surface. This difference in interlayer position may significantly influence the organization of P3HT chains on the hybrid interface. Alternatively, the two interlayers, while filling different type of surface defects, might be disposed in one case on sites of potential charge recombination, this way diminishing the process, known as one of the major causes of low device performance, whereas in the other case might be disposed on sites where charge separation takes place favorably, thus reducing photo-current generation.

Table 4.5. Characteristic solar cell parameters for ncTiO$_2$/P3HT hybrid devices with and without interlayer described previously.

Active-layer configuration	V_{OC} (V)	J_{SC} (mA cm^{-2})	FF	η (%)
nc-TiO$_2$/**1**/**P3HT**	0.72	1.19	0.62	0.61
nc-TiO$_2$/**8**/**P3HT**	0.52	0.73	0.52	0.24
nc-TiO$_2$/**14**/**P3HT**	0.68	0.26	0.43	0.09
nc-TiO$_2$/**P3HT**	0.35	1.74	0.54	0.39

As a second point, the role of interaction directionality in determining cell efficiency is highlighted. Indeed, the simple displacement of the nitrogen atom from the 4- to the 3-position of the pyridil ring, when going from interlayer **1** to interlayer **8**, leads also to an overall decrease of all the parameters determining solar cell performance.

The influence of P3HT molecular weight on solar cell efficiency was further investigated, by substituting the donor polymer previously used with one having a higher molecular weight. The effect was verified only for interlayer **1**, being the best performing material among those previously tested (Figure 4.10). Interestingly, the use of a higher molecular weight polymer causes a significant increase in the open circuit voltage of the device with interlayer **1**, with respect to the control device but also with respect to the voltage value obtained from the use of the same interlayer in combination with lower molecular weight P3HT (Figure 4.9). The value is almost reaching the theoretical limit, given by the energy difference, expressed in volts, between the P3HT HOMO level and the TiO$_2$ conduction band. Furthermore, the device with interfacial modification maintains the same value of photo-current as the one extracted from the device based on bare TiO$_2$. Table 4.6 shows the characteristic parameters for the two devices.
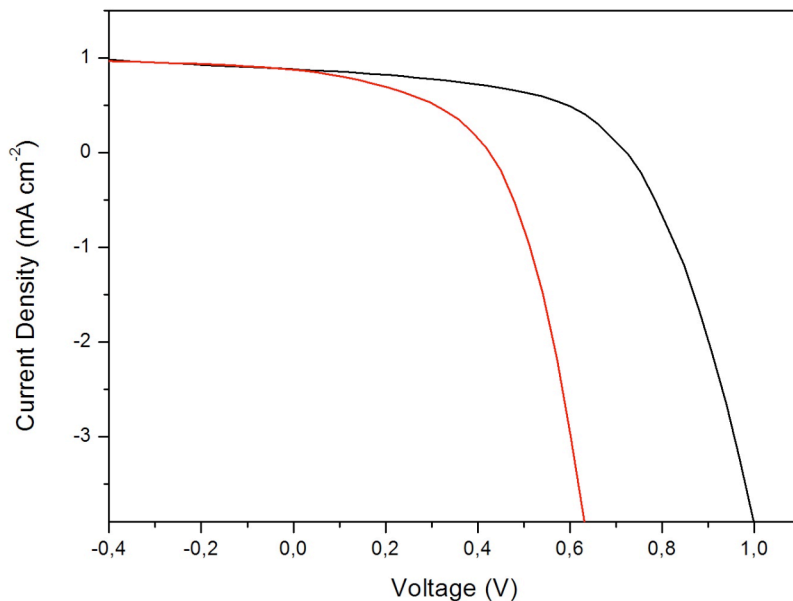
Figure 4.10. Current-voltage characteristics of nc-TiO$_2$/P3HT hybrid solar cells with interlayer **1** (black line) and without any interlayer (red line). The P3HT employed here had M$_W$=77500, PD=2 and RR=96.3%.

Table 4.6. Characteristic solar cell parameters for ncTiO$_2$/P3HT hybrid devices with and without interlayer **1**.

Active-layer configuration	V_{OC} (V)	J_{SC} (mA cm^{-2})	FF	η (%)
nc-TiO$_2$/**1**/**P3HT**	1	1	0.53	0.46
nc-TiO$_2$/**P3HT**	0.61	1	0.44	0.23

As a second step in the testing of the novel functionalized oligothiophene interlayers for nc-TiO$_2$/P3HT hybrid devices, bithiophene derivatives **4** and **7** were selected and their activities were compared with those of compound **1** and of its regioisomer **13**, under the same experimental conditions. As good practice, reference samples are produced and measured in each devices batch: due to experimental variability when going from one batch of devices to another, recurrent comparison of each

134

interlayer effect with the one of the best performing derivative and, at the same time, with the one of a device without any interfacial modification is advised. Figure 4.11 reports the variations in the characteristic solar cell parameters as a function of the different interlayer used. Up till now, these devices have been tested on a home-made apparatus mimicking solar spectrum, with lower radiation power with respect to standard AM1.5 conditions. This is the reason of the general low values shown here for this set of hybrid solar cells. Reasonable conclusions may be derived anyway from the experiment, thanks to the internal control devices. At first glance, the leading performance of interlayer **1** above all the tested interlayers is further confirmed here. The record is detained not only in the final PCE of the device, but also in all the other characteristic parameters. Secondly, the role of directionality in the interaction with the metal oxide surface is further confirmed here by the worst photovoltaic performance obtained with regioisomeric interlayer **13**. Indeed, a general decrease in photovoltaic parameters is observed when using an interlayer, compund **13**, in which the 4-pyridyl ring has been moved in α-position of the thienyl ring with respect to the homologous interlayer bearing the 4-pyridyl moiety in β-position of the thienyl ring, namely compound **1**. Finally, the insertion of the alkyl side-chains on the interlayer structure doesn't lead to the expected improvement, resulting from better ordering of the P3HT chains onto the hybrid interface. Among the two bithiophene derivatives bearing alkyl side-chains anyway, better performance is reached with interlayer **7** in comparison to interlayer **4**, and this behavior might be explained with the more pronounced

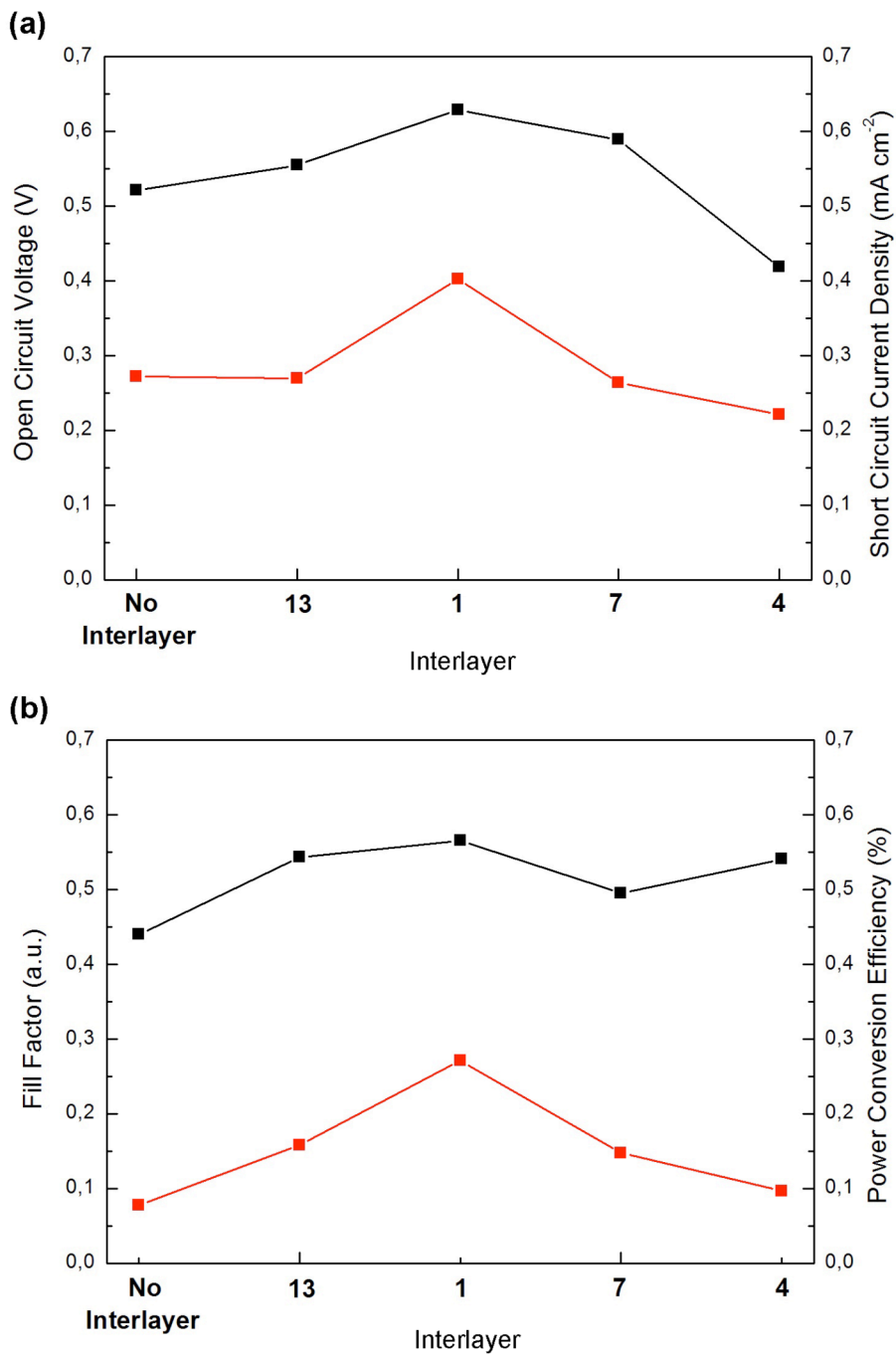**(a)**

(b)

Figure 4.11. Characteristic parameters for nc-TiO$_2$/P3HT hybrid solar cells with interlayers **1**, **4**, **7** and **13** and with no interlayer. a) Open-circuit voltages (black squares), short-circuit current densities (red squares). b) Fill-factors (black squares), power conversion efficiencies (red squares).

distortion encountered for compound **4** conformation, impeding the occurrence of the proper interactions with both the porous metal oxide scaffold and the polymer chains required for interface optimization. The major planarity characterizing interlayer **7**, is likely the cause of its better performance in nc-TiO$_2$/P3HT hybrid solar cells. Further studies are required to furnish a definitive interpretation of these photovoltaic results. Molecular modeling might be helpful to demonstrate the role of molecular inter-ring distorsion in compounds **4** and **7** in determining the effective disposition of the P3HT chains on the functionalized titania surface.

For the sake of clarity it is worth mentioning here that, given the detrimental performances obtained by using 3-pyridyl functionalized and 4-carboxyphenyl functionalized interlayers **8** and **14**, the further testing of other related derivatives, namely bithiophenes **11** and **20** and terthiophenes **12** and **21**, was not attempted.

4.3 Conclusions and outlook

In conclusion, this work further demonstrates the possibility of improving the performance of nc-TiO$_2$/P3HT hybrid solar cells by insertion of a proper molecular interlayer on the hybrid interface, able to simultaneously interact with the titania surface and to induce the local organization of the polymer chains. The significant role played by the molecular configuration of the interlayer was highlighted by the results here reported. Even if up to now the best performances were obtained with the simple 3-(4-pyridil)-thiophene interlayer, which in one case almost doubled solar cell efficiency, valuable guidelines were traced for the design of novel interfacial modifiers, with increased activities.

Specifically, the importance of the relative position of side-groups on the interlayer structure has arisen, stating the need for a stringent control over the directionality of intermolecular interactions established at the interface. Indeed, the insertion of lateral alkyl chains on the oligothiophene backbone might be effective in reaching an improved organization of the polymer chains on the hybrid interface, if these substituents are disposed properly.

Based on these indications, new molecules have been designed. One of this new species is represented by compound **22**, reported in Figure 4.12.

22
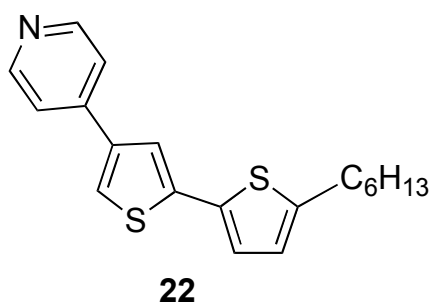
Figure 4.12. Chemical structure of prospected interlayer **22**.

This configurational isomer of compounds **4** and **7**, presents a displacement of the hexyl chain on the furthest position with respect to the 4-pyridil ring, thus resulting in a complete planarity of the bithienylenic backbone but also, possibly, in the right directionality for establishing the correct, interactions with both the metal oxide surface and polymer chains. The synthesis of compound **22**, together with the testing of its effectiveness as interlayer in nc-TiO$_2$/P3HT hybrid devices, is therefore significantly envisaged in order to extend the perspectives of the present work.

4.4 Experimental

Materials

All chemicals were purchased from commercial suppliers and used without further purification. When requested, dry solvents were obtained by classical methods and kept under argon. ^{1}H and ^{13}C NMR spectra were measured on a Bruker ARX 400. ESI-MS was performed on a Bruker Esquire 3000 plus.

The 4- and 3-pyridil functionalized thiophene, bithiophene and terthiophene derivatives were synthesized as follows.

3-(4-pyridyl)-thiophene (**1**). **Route A**. This procedure was adapted from the literature.[7] 3-Bromothiophene (0.36 ml, 3.8 mmol) was dissolved in argon degassed DME (25 ml) and H_2O (12.5 ml). K_2CO_3 (3.7 g, 26.6 mmol) and $Pd(PPh_3)_4$ (440 mg, 0.38 mmol) were added and the resulting yellow solution was stirred at room temperature for 10 min. 4-Pyridinylboronic acid (470 mg, 3.8 mmol) was then added and the reaction mixture was heated up to reflux for 8 h under argon. After cooling to room temperature, it was transferred to a separator funnel, where water (15 ml) was added. The mixture was extracted with Et_2O (2 x 40 ml). Organics were combined, dried (Na_2SO_4), filtered and concentrated to leave a dark-yellow residue, which was charged on a silica-gel column. Elution with pure ethyl acetate gave the pure product as a white solid (220 mg, 36%).

Route B. This procedure was also adapted from the literature.[8] To a solution of 4-iodopyridine (500 mg, 2.5 mmol) in DME/H_2O (30 ml + 15 ml respectively), previously purged with argon for 15 min, K_2CO_3 (2.4 g, 17.5 mmol), $Pd(PPh_3)_4$ (289 mg, 0.25 mmol) and 3-thiophene boronic acid (320 mg, 2.5 mmol) were added. The reaction mixture was taken to reflux and stirred at that temperature for 8 h under an argon atmosphere.

139

After cooling to room temperature, it was transferred to a separator funnel and water (15 ml) was added. The mixture was extracted with Et_2O (2 x 30 ml) and the combined organic layers were dried (Na_2SO_4), filtered and the solvent was evaporated. The crude product was purified by column chromatography on silica-gel eluting with ethyl acetate and dried under vacuum to give **1** as a white solid (294 mg, 73%)

Route C. This procedure was taken from the literature,[5] but used here for the first time for the synthesis of **1**. 3-Thiopheneboronic acid MIDA ester (597 mg, 2.5 mmol), 4-iodopyridine (500 mg, 2.5 mmol), SPhos (103 mg, 0.25 mmol) and $Pd(OAc)_2$ (27 mg, 0.12 mmol) were added to argon degassed dioxane (30 ml) and H_2O (15 ml). The resulting mixture was stirred at room temperature for 10 min. K_3PO_4 (4 g, 18.7 mmol) was then added and the reaction mixture was heated up to 80 $^{\circ}$C for 6 h under an argon atmosphere. After cooling to room temperature the mixture was transferred to a separatory funnel together with Et_2O (30 ml) and water (30 ml). The mixture was shacked and the two phases were separated. The aqueous phase was further extracted with Et_2O (2 x 20 mL). Organics were combined, dried (Na_2SO_4), filtered and concentrated in vacuo. The crude residue was subjected to flash chromatography (ethyl acetate) to give **1** as white solid in 61% yield (246 mg). ^{1}H-NMR (400 MHz, $CDCl_3$, ppm): δ 8.61 (2 H, dd, J = 4.7, 1.6 Hz, PyH), 7.69 (1H, dd, J = 2.5, 1.6 Hz, Th$H2$), 7.52 (2H, dd, J = 4.7, 1.6 Hz, PyH), 7.49-7.42 (2H, m, Th$H4$, Th$H5$).

2-Bromo-3-(4-pyridyl)-thiophene (**2**). This procedure and the following one were adapted from the literature.[8] To a solution of **1** (120 mg, 0.74 mmol) in acetic acid (10 ml) was added dropwise a solution of NBS (197 mg, 1.11 mmol) in acetic acid (15 ml) and the mixture was allowed to react for 4 h at room temperature and at repair from light. The mixture

140

was poured gently in a saturated sodium bicarbonate solution (100 ml) and stirred until complete evolution of CO_2. It was then transferred to a separator funnel and extracted with dichloromethane (3 x 30 ml). The combined organic extracts were dried over Na_2SO_4, filtered and concentrated. The residue was purified by column chromatography (silica gel, hexane:ethyl acetate 20/80) to afford **2** as a yellowish solid (78 mg, 44%). ^{1}H-NMR (400 MHz, $CDCl_3$, ppm): δ 8.67 (2 H, d, $J = 4.1$ Hz, Py*H*), 7.50 (2H, d, $J = 5.3$ Hz, Py*H*), 7.35 (1H, d, $J = 5.7$ Hz, Th*H5*), 7.05 (1H, d, $J = 5.7$ Hz, Th*H4*).

2,5-Dibromo-3-(4-pyridyl)-thiophene (**3**). The compound was synthesized following the same procedure as described for **2**, employing 215 mg of **1** (1.33 mmol) and 710 mg of NBS (3.99 mmol). Column chromatography (hexane:ethyl acetate 30/70) gave **3** as a light yellow solid (407 mg, 96%). ^{1}H-NMR (400 MHz, $CDCl_3$, ppm): δ 8.69 (2 H, d, $J = 5.3$ Hz, Py*H*), 7.49 (2H, d, $J = 5.8$ Hz, Py*H*), 7.06 (1H, s, Th*H4*).

Pyridine,4-(3'-hexyl[2,2'-bithiophene]-3yl) (**4**). The synthesis and characterization of this compound is reported here for the first time. **2** (70 mg, 0.29 mmol) was dissolved in argon degassed DME/H_2O mixture (20 ml + 10 ml respectively). K_2CO_3 (280 mg, 2.03 mmol) was then added, together with $Pd(PPh_3)_4$ (34 mg, 0.03 mmol). The mixture was stirred at room temperature for 15 min and 3-hexylthiophene-2-boronic acid pinacol ester (95 mg, 0.32 mmol) was added. Heating was then carried under an argon atmosphere at reflux temperature for 8 h, whereupon the solution was cooled down to room temperature. It was then transferred to a separator funnel, together with water (15 ml) and diethyl ether (25 ml) and, after vigorous shaking, phases were separated and the aqueous phase was extracted agin with Et_2O (2 x 15 ml). Organics were combined, dried (Na_2SO_4), filtered and concentrated, to leave a yellowish oily residue.

Purification by column chromatography (silica gel, 1:2 hexane/EtOAc) afforded the pure product as a brownish oil, which become a crystalline waxy solid after 2 h of storage in the fridge at 4 °C (35 mg, 37%). Melting point (from DSC): 39.4 °C. ^{1}H-NMR (400 MHz, CDCl$_3$, ppm): δ 8.47 (2H, dd, J = 4.7, 1.56 Hz, Py$H3,5$), 7.43 (1H, d, J= 5.27 Hz, Th$H4$), 7.29 (1H, d, J= 5.1 Hz, Th$H5$), 7.25 (1H, d, J= 5.27 Hz, Th$H5'$), 7.17 (2H, dd, J= 4.7, 1.56 Hz, Py$H2,6$), 6.90 (1H, d, J= 5.27 Hz, Th$H4'$), 2.25 (2H, t, J = 8 Hz, ThCH_2), 1.33-1.11 (8H, m, -(CH_2)$_4$-), 0.821 (3H, t, J= 7.2 Hz, -CH_3). ^{13}C-NMR (100.8 MHz, CDCl$_3$, ppm): δ 149.6, 143.9, 142.4, 137.7, 132.9, 128.9, 128.2, 127.7, 126.6, 126.2, 122.7, 31.4, 29.9, 29.0, 28.6, 22.4, 13.9. MS (ESI): m/z [M$^+$] 327.11; calcd m/z [M$^+$] 327.5.

Pyridine,4-(3,3''-dihexyl[2,2':5',2''-terthiophene]-3'yl) (**5**). The synthesis and characterization of this compound is reported here for the first time. The synthetic procedure is totally analogous to the one described for **4**, starting from **3** (400 mg, 1.25 mmol), 3-hexylthiophene-2-boronic acid pinacol ester (812 mg, 2.75 mmol), Pd(PPh$_3$)$_4$ (138 mg, 0.12 mmol) and K$_2$CO$_3$ (1.2 g, 8.75 mmol) in DME/H$_2$O mixture (25 ml + 12.5 ml). **5** was obtained as a light-yellow oil after purification on a silica-gel column with hexane:ethyl acetate 1/1 mixture in 30% yield (185 mg). ^{1}H-NMR (400 MHz, CDCl$_3$, ppm): δ 8.53 (2H, dd, J = 4.7, 1.56 Hz, Py$H3,5$), 7.32 (1H, d, J= 5.27 Hz, Th$H5'$), 7.25 (1H, s, Th$H4$), 7.19-7.23 (3H, m, Py$H2,6$ + Th$H5''$), 6.98 (1H, d, J= 5.27 Hz, Th$H4'$), 6.93 (1H, d, J= 5.27 Hz, Th$H4''$), 2.83 (2H, t, J = 8 Hz, ThCH_2'), 2.34 (2H, t, J = 8 Hz, ThCH_2''), 1.61-1.71 (2H, m, ThCH$_2$CH_2'), 1.42-1.12 (14H, m, -(CH_2)'$_3$- + -(CH_2)''$_4$-), 0.97-0.82 (6H, m, -CH_3). ^{13}C-NMR (100.8 MHz, CDCl$_3$, ppm): δ 149.6, 143.7, 142.6, 140.3, 137.7, 137.4, 132.2, 130.1, 129.5, 129.1, 129, 127.5, 126.5, 126.4, 124.2, 122.8. MS (ESI): m/z [M+H$^+$] 494.6; calcd m/z [M+H$^+$] 494.20.

4-Bromo-3'-hexyl(2,2'-bithiophene) (**6**). The synthesis of this compound is reported here for the first time. 2,4-Dibromothiophene (500 mg, 2.07 mmol) was dissolved in argon degassed DME (25 ml). Degassed H_2O (12.5 ml), together with K_2CO_3 (1.8 g, 13.16 mmol) and Pd(PPh$_3$)$_4$ (219 mg, 0.19 mmol) were added and the mixture was stirred for 10 min. 3-hexylthiophene-2-boronic acid pinacol ester (553 mg, 1.88 mmol) was then added and the reaction mixture was refluxed for 8 h, whereupon it was cooled down to room temperature. The mixture was poured into water (20 ml) and extracted with Et_2O (2 x 30 ml). Organics were combined, dried (Na_2SO_4), filtered and concentrated to leave a yellow oily residue. Column chromatography on silica gel afforded a transparent oil, which was not yet the pure product. Further purification was achieved by adding the minimum amount of pentane needed for the total dissolution of the oily residue and placing the solution in the fridge at -20 ^{o}C. A white crystalline precipitate formed, which was filtered and washed with cold pentane. The solid was one of the side-products, formed after bromo-boronic exchange, namely 4,4'-dibromo-2,2'-bithiophene. The other side-product resulting from the aforementioned exchange, 3,3'-dihexyl-2,2'-bithiophene, resulted impossible to separate from **6**, both compounds obtained after evaporation of pentane in vacuo as a colorless oil. The relative amount of the two bithiophenes was determined from the ratio between the integral values of selected signals in the ^{1}H NMR spectra. Given the total un-reactivity of the 3,3'-dihexyl-2,2'-bithiophene side-product towards the conditions used for the following cross-coupling step, it was decided to avoid the further purification of **6**, which resulted to be formed in 15% yield (92 mg). ^{1}H-NMR (400 MHz, CDCl$_3$, ppm): δ 7.19 (2H, m, Th*H5 + 5'*), 7 (1H, *J* = 1.37 Hz, Th*H3*), 6.93 (1H, d, *J* = 5.01 Hz, Th*H4'*), 2.72 (2H, t, *J* = 8 Hz,

ThCH_2), 1.61 (2H, m, ThCH$_2$CH_2), 1.4-1.21 (6H, m, -(CH_2)$_3$-), 0.89 (3H, t, J= 7.2 Hz, -CH_3).

Pyridine,4-[3'-hexyl(2,2'-bithiophene)-4yl] (**7**). The synthesis and characterization of this compound is reported here for the first time. The synthetic procedure is analogous to the one described for **1** (**Route A**) by employing 87 mg of **6** (0.26 mmol), 4-pyridilboronic acid (36 mg, 0.29 mmol), K$_2$CO$_3$ (251 mg, 1.82 mmol) and Pd(PPh$_3$)$_4$ (30 mg, 0.026 mmol) in argon degassed DME/H$_2$O (15 ml + 7.5 ml). The compound was purified by column chromatography (silica, hexane:ethyl acetate 1/1) and was isolated as a brownish oil in 42% yield (36 mg). ^{1}H-NMR (400 MHz, CDCl$_3$, ppm): δ 8.63 (2H, dd, J = 4.68, 1.56 Hz, Py$H3,5$), 7.61 (1H, d, J = 1.4 Hz, Th$H3$), 7.49 (2H, dd, J = 4.68, 1.56 Hz, Py$H2,6$), 7.4 (1H, d, J = 1.4 Hz), 7.21 (1H, d, J = 5.27 Hz, Th$H5'$), 7.96 (1H, d, J = 5.27 Hz, Th$H4'$), 2.78 (2H, t, J = 8 Hz, ThCH_2), 1.71-1.58 (2H, m, ThCH$_2$CH_2), 1.24-1.41 (6H, m, -(CH_2)$_3$-), 0.88 (3H, t, J= 7.2 Hz, -CH_3). MS (ESI): m/z [M+H$^+$] 328.4; calcd m/z [M+H$^+$] 328.51; [M+Na$^+$] 350.3; calcd m/z [M+Na$^+$] 350.1.

3-(3-pyridyl)-thiophene (**8**). The preparation of this compound and of its bithiophene and terthiophene derivatives **11** and **12** is reported here for the first time.

Route A. This procedure for the synthesis and purification of **8** was identical to the one described for **1** (**Route A**), using 3-bromothiophene (0.38 ml, 4.05 mmol), 3-pyridilboronic acid (500 mg, 4.05 mmol), K$_2$CO$_3$ (7.8 g, 57 mmol) and Pd(PPh$_3$)$_4$ (924 mg, 0.8 mmol) in argon degassed DME/H$_2$O (30 ml + 15 ml) and affording the product as a white solid in 44% yield (574 mg).

Route B. Identical procedure as for **1** (**Route B**), using 3-thiophene boronic acid (312 mg, 2.44 mmol), 3-iodopyridine (500 mg, 2.44 mmol),

144

K$_2$CO$_3$ (2.35 g, 17 mmol) and Pd(PPh$_3$)$_4$ (277 mg, 0.24 mmol) in argon degassed DME/H$_2$O (15 ml + 7.5 ml) and affording **8** in 63% yield (248 mg).

Route C. Identical procedure as for **1** (**Route C**), using 3-thiopheneboronic acid MIDA ester (583 mg, 2.44 mmol), 3-iodopyridine (500 mg, 2.44 mmol), K$_3$PO$_4$ (3.9 g, 18.3 mmol), SPhos (98 mg, 0.24 mmol) and Pd(OAc)$_2$ (27 mg, 0.12 mmol) in argon degassed dioxane/H$_2$O (30 ml + 15 ml) and affording the product in 70% yield (275 mg). ^{1}H-NMR (400 MHz, CDCl$_3$, ppm): δ 8.87 (1H, s, Py*H2*), 8.52 (1H, dd, *J* = 3.9, 0.78 Hz, Py*H4*), 7.92-779 (1H, m, Py*H5*), 7.52 (1H, dd, *J* = 2.93, 1.17 Hz, Th*H2*), 7.44 (1H, dd, *J* = 5.07, 2.93 Hz, Th*H5*), 7.38 (1H, dd, *J* = 5.07, 1.17 Hz, Th*H4*), 7.39-7.28 (1H, m, Py*H6*).

2-Bromo-3-(3-pyridyl)-thiophene (**9**). The compound was synthesized following the procedure already described for the preparation of **2**, starting from **8** (100 mg, 0.62 mmol) and NBS (193 mg, 1.08 mmol) in acetic acid (10 + 5 ml). The pure product was obtained in 51% yield (76 mg) after flash chromatography (silica gel, hexane:ethyl acetate 20/80). ^{1}H-NMR (400 MHz, CDCl$_3$, ppm): δ 8.79 (1 H, s, Py*H2*), 8.59 (1H, d, *J* = 4.4 Hz, Py*H4*), 7.89 (1H, dt, *J* = 7.6, 2 Hz, Py*H5*), 7.36 (2H, m, Py*H6*, Th*H5*), 7.04 (1H, d, *J* = 5.6 Hz, Th*H4*).

2,5-Dibromo-3-(3-pyridyl)-thiophene (**10**). The same bromination procedure used for **2**, **3** and **9** was employed for the synthesis of **10**, starting from **8** (300 mg, 1.86 mmol) and NBS (1.16 g, 6.51 mmol) in 10 + 10 ml of acetic acid. Purification was achieved *via* flash chromatography on silica gel, eluting with hexane:ethyl acetate 30/70, affording **10** in 65% yield (386 mg). ^{1}H-NMR (400 MHz, CDCl$_3$, ppm): δ 8.72 (1 H, d, *J* = 1.6 Hz, Py*H2*), 8.57 (1H, dd, *J* = 4.7, 1.6 Hz, Py*H4*),

7.79 (1H, ddd, J = 7.6, 2.2, 1.8 Hz, Py*H5*), 7.32 (1H, ddd, J = 8, 4.9, 0.8 Hz, Py*H6*), 7.00 (1H, s, Th*H4*).

Pyridine,3-(3'-hexyl[2,2'-bithiophene]-3yl) (**11**). The compound was prepared starting from compound **9** (70 mg, 0.29 mmol) and using the same procedure as described for the synthesis of **4**. 3-hexylthiophene-2-boronic acid pinacol ester (94 mg, 0.32 mmol), Pd(PPh$_3$)$_4$ (35 mg, 0.03 mmol) and K$_2$CO$_3$ (280 mg, 2.03 mmol) were employed in DME/H$_2$O mixture (15 ml + 7.5 ml). **11** was obtained as a transparent oil after purification on a silica-gel column with hexane:ethyl acetate 1/2 mixture in 51% yield (48 mg). ^{1}H-NMR (400 MHz, CDCl$_3$, ppm): δ 8.57 (1 H, d, J = 1.6 Hz, Py*H2*), 8.45 (1H, dd, J = 4.7, 1.6 Hz, Py*H4*), 7.54 (1H, ddd, J = 7.6, 2.2, 1.7 Hz, Py*H5*), 7.43 (1H, d, J = 5.3 Hz, Th*H5*), 7.25 (1H, d, J = 5.3 Hz, Th*H4*), 7.22 (1H, d, J = 5.3 Hz, Th*H5'*), 7.17 (1H, ddd, J = 8, 4.9, 0.8 Hz, Py*H6*), 6.88 (1H, d, J = 5.3 Hz, Th*H4'*). ^{13}C-NMR (100.8 MHz, CDCl$_3$, ppm): δ 149.1, 147.7, 142.2, 137.1, 135.5, 132.2, 131.7, 128.9, 128.4, 127.9, 126.5, 126.1, 123.1, 31.5, 30.0, 29.0, 28.7, 22.4, 13.9. MS (ESI): m/z [M+H^{+}] 328.5; calcd m/z [M+H^{+}] 328.51; [M+Na^{+}] 350.4; calcd m/z [M+Na^{+}] 350.1.

Pyridine,4-(3,3''-dihexyl[2,2':5',2''-terthiophene]-3'yl) (**12**). The compound was prepared according to the same procedure described for compound **5**, starting from **10** (240 mg, 0.76 mmol), 3-hexylthiophene-2-boronic acid pinacol ester (188 mg, 1.66 mmol), Pd(PPh$_3$)$_4$ (70 mg, 0.06 mmol) and K$_2$CO$_3$ (560 mg, 4.06 mmol) were employed in DME/H$_2$O mixture (30 ml + 15 ml). **12** was obtained as a yellow dense oil after purification *via* flash chromatography (silica gel, hexane:ethyl acetate 1/1) in 47% yield (176 mg). ^{1}H-NMR (400 MHz, CDCl$_3$, ppm): δ 8.60 (1 H, d, J = 1.6 Hz, Py*H2*), 8.47 (1H, dd, J = 4.7, 1.6 Hz, Py*H4*), 7.58 (1H, ddd, J = 8, 2.2, 1.7 Hz, Py*H5*), 7.27 (1H, d, J = 5.3 Hz, Th*H5'*), 7.24

(4H, m, Py*H3*,Py*H6*, Th*H4*, Th*H5''*), 6.97 (1H, d, J = 5.3 Hz, Th*H4'*), 6.89 (1 H, d, J = 5.3 Hz, Th*H4''*). ^{13}C-NMR (100.8 MHz, CDCl$_3$, ppm): δ 149.2, 147.9, 142.3, 140.2, 137.2, 135.5, 132.0, 131.1, 130.1, 129.0, 127.7, 126.8, 126.2, 124.1, 123.1, 115.5, 31.6, 31.5, 30.6, 30.1, 29.3, 29.1, 29.0, 28.8, 22.5, 22.5, 14.0. MS (ESI): m/z [M+H$^+$] 494.5; calcd m/z [M+H$^+$] 494.2; [M+Na$^+$] 516.4; calcd m/z [M+Na$^+$] 516.18.

2-(4-pyridyl)-thiophene (**13**). This compound is already reported in the literature,[9] but the synthetic procedures used here are slightly different. The three procedures are the same as reported for **1** and **8** (**Routes A**, **B**, **C**), for both synthesis and purification. Only reactants quantities and yields will be reported here.

Route A. 2-bromothiophene (0.19 ml, 2.03 mmol), 4-pyridilboronic acid (250 mg, 2.03 mmol), K$_2$CO$_3$ (1.9 g, 14 mmol), Pd(PPh$_3$)$_4$ (235 mg, 0.2 mmol), DME (20 ml), H$_2$O (10 ml). Yield: 64% (210 mg, light yellow solid).

Route B. 2-thiophene boronic acid (137 mg, 1.07 mmol), 4-iodopyridine (219 mg, 1.07 mmol), K$_2$CO$_3$ (1 g, 7.5 mmol), Pd(PPh$_3$)$_4$ (115 mg, 0.1 mmol), DME (20 ml), H$_2$O (10 ml). Yield: 55% yield (95 mg).

Route C. 2-thiopheneboronic acid MIDA ester (200 mg, 0.84 mmol), 4-iodopyridine (171 mg, 0.84 mmol), K$_3$PO$_4$ (1.34 g, 6.3 mmol), SPhos (33 mg, 0.08 mmol), Pd(OAc)$_2$ (9 mg, 0.04 mmol), dioxane (15 ml), H$_2$O (7.5 ml). Yield: 68% (92 mg). ^{1}H-NMR (400 MHz, CDCl$_3$, ppm): δ 8.59 (2H, dd, J = 4.68, 1.56 Hz, Py*H*), 7.5 (1H, dd, J = 3.51, 0.98 Hz, Th*H3*), 7.48 (2H, dd, J = 4.68, 1.56 Hz, Py*H*), 7.41 (1H, dd, J = 5.07, 0.98 Hz, Th*H5*), 7.14 (1H, dd, J = 5.07, 3.51 Hz, Th*H4*).

The 4-carboxyphenyl functionalized thiophene, bithiophene and terthiophene derivatives were synthesized as follows.

4-Thiophene-3-yl-benzoic acid **14** was synthesized following a literature procedure.[10] The synthesis and characterization of compound **15** *via* **Route A** has been already reported in Chapter 3, together with the synthesis of compounds **17** and **19**, therefore they will not be reported here again. The procedures relative to the syntesis of compound **15** *via* **Routes B** and **C** are the same as reported for compounds **1**, **8** and **13**. Only reactants quantities and yields will be reported therefore. Ethyl-4-bromobenzoate was prepared following a literature procedure.[11]

Route B. 2-thiophene boronic acid (2.02 g, 15.8 mmol), Ethyl-4-bromobenzoate (3.62 g, 15.8 mmol), K_2CO_3 (15.29 g, 110.6 mmol), $Pd(PPh_3)_4$ (1.85 g, 1.6 mmol), DME (60 ml), H_2O (30 ml). The product was purified by flash chromatography (silica gel, 1:1 hexane/CH_2Cl_2). Yield: 55% yield (2.64 g).

Route C. 2-thiopheneboronic acid MIDA ester (500 mg, 2.1 mmol), Ethyl-4-bromobenzoate (479 mg, 2.1 mmol), K_3PO_4 (3.3 g, 15.75 mmol), SPhos (82 mg, 0.2 mmol), $Pd(OAc)_2$ (22 mg, 0.2 mmol), dioxane (25 ml), H_2O (12.5 ml). The product was purified by flash chromatography (silica gel, 1:1 hexane/CH_2Cl_2). Yield: 87% (424 mg).

2-Bromo-3-(4-ethylbenzoate)-thiophene (**16**). The compound was synthesized following the same procedure described for the synthesis of *2,5-dibromo-3-(4-ethylbenzoate)-thiophene* reported in Chapter 2, using **15** (500 mg, 2.15 mmol) and NBS (420 mg, 2.36 mmol) in 15 ml of dry DMF. Purification through column chromatography (silica gel, 1:1 hexane/CH_2Cl_2) gave **16** as a light yellow waxy solid in 54% yield (359 mg). ^{1}H-NMR (400 MHz, $CDCl_3$, ppm): δ 8.1 (2 H, d, J = 8.4 Hz, Ph*H3,5*), 7.64 (2H, d, J = 8.4 Hz, Ph*H2,6*), 7.33 (1H, s, Th*H5*), 7.04 (1H, s, Th*H4*), 4.40 (2H, q, -OC*H2*), 1.43 (3H, t, -C*H3*).

(4-Ethoxycarbonyl)3-phenyl-3'-hexyl-2,2'-bithiophene (**18**). The compound was synthesized following the same procedure described for the synthesis of *(4-Ethoxycarbonyl)3-phenyl-3',3''-dihexyl-2,2':5',2''-terthiophene* reported in Chapter 2, using compound **16** (400 mg, 1.28 mmol), 3-hexylthiophene-2-boronic acid pinacol ester (416 mg, 1.42 mmol), Pd(PPh$_3$)$_4$ (52 mg, 0.04 mmol) and K$_2$CO$_3$ (1.27 g, 9.2 mmol) in argon degassed DME/H$_2$O mixture (30 ml/15 ml). Purification was achieved *via* flash chromatography (silica gel, 1:1 petroleum ether/CH$_2$Cl$_2$), affording the product as transparent oil in 37% yield (188 mg). ^{1}H-NMR (400 MHz, CDCl$_3$, ppm): δ 7.92 (2 H, d, *J* = 8.4 Hz, Ph*H3,5*), 7.41 (1H, d, *J* = 5.3 Hz, Th*H5*), 7.33 (2H, d, *J* = 8.4 Hz, Ph*H2,6*), 7.25 (1H, d, *J* = 5.6 Hz, Th*H5'*), 7.23 (1H, d, *J* = 5.3 Hz, Th*H4*), 6.86 (1H, d, *J* = 5.3 Hz, Th*H4'*), 4.34 (2H, q, *J* = 7.2 Hz, OC*H$_2$*), 2.23 (2H, t, *J* = 7.7 Hz, ThC*H$_2$*), 1.37 (3H, t, *J* = 7.2 Hz, OCH$_2$C*H$_3$*), 1.26-1.08 (8H, m, -C*H$_2$*-), 0.81 (3H, t, *J* = 7.2 Hz, -C*H$_3$*). ^{13}C-NMR (100.8 MHz, CDCl$_3$, ppm): δ 166.4, 142.1, 140.8, 139.7, 131.5, 129.6, 128.8, 128.2, 126.1, 125.9, 60.8, 31.5, 30.8, 29.9, 29.0, 28.7, 22.4, 14.3, 13.9. MS (ESI): m/z [M+Na]$^+$ 421.1, calcd m/z for [M+Na]$^+$ 421.13.

(4-Carboxy)3-phenyl-3'-hexyl-2,2'-bithiophene (**20**). A solution of **18** (174 mg, 0.44 mmol) in 15 ml of THF was treated with 1.5 ml of a 1M KOH solution and heated up to reflux for 6 h. Since, after this time, residual ethyl ester was still present in the reaction mixture, as evidenced by TLC, other 1.5 ml of 1M KOH were added and reflux was continued for other 7 h. After cooling to room temperature, the mixture was treated with 0.1 M HCl until neutrality and then transferred to a separatory funnel where H$_2$O (10 ml) and CH$_2$Cl$_2$ (40 ml) were added. After phase separation, the aqueous phase was further extracted with CH$_2$Cl$_2$ (2 x 10 ml). The combined organics were dried over Na$_2$SO$_4$, filtered and

149

concentrated to leave a transparent oily residue, containing the hydrolized product together with the ethyl ester reagent. Pure **20** was obtained by adding 10 ml of hexane to the residue, causing the precipitation of a white solid, which was filtered, washed with hexane and dried in *vacuo* (102 mg, 63% yield). ^{1}H-NMR (400 MHz, CDCl$_3$, ppm): δ 8.01 (2 H, d, J = 8.2 Hz, Ph*H3,5*), 7.43 (1H, d, J = 5.3 Hz, Th*H5*), 7.39 (2H, d, J = 8.4 Hz, Ph*H2,6*), 7.28 (1H, d, J = 5.5 Hz, Th*H5'*), 7.26 (1H, d, J = 5.3 Hz, Th*H4*), 6.89 (1H, d, J = 5.3 Hz, Th*H4'*), 2.26 (2H, t, J = 7.8 Hz, ThC*H2*), 1.32-1.11 (8H, m, -C*H2*-), 0.83 (3H, t, J = 7.5 Hz, -C*H3*). MS (ESI): m/z 393.4 [M+Na]$^+$, calcd m/z for [M+Na]$^+$ 393.09.

(4-Carboxy)3-phenyl-3',3''-dihexyl-2,2':5',2''-terthiophene (**21**). The compound was prepared following the same procedure as described for **20**, starting from **19** (80 mg, 0.14 mmol) dissolved in 10 ml of THF and 1M KOH (0.5 + 0.5 ml). The carboxylic acid was obtained in pure form after filtration on a very short silica gel column, first eluting with 1:1 hexane/ethyl acetate to get rid of the residual, un-hydrolized ethyl ester and then increasing the polarity up to 9:1 ethyl acetate/methanol to elute the product, which, after solvent removal and thorough vacuum drying resulted a yellow dense oil (37 mg, 49% yield). ^{1}H-NMR (400 MHz, (CD$_3$)$_2$CO, ppm): δ 7.98 (2 H, d, J = 8.6 Hz, Ph*H3,5*), 7.34-7.24 (5H, m, Ph*H2,6* + Th*H4,5',5''*), 7.02 (1H, d, J = 5.2 Hz, Th*H4'*), 6.89 (1H d, J = 5.2 Hz, Th*H4''*), 2.82 (2H, t, J = 7.7 Hz, ThC*H2*), 2.31 (2H, t, J = 7.7 Hz, ThC*H2*CH2), 1.66 (2H, quin, J = 7.7 Hz, ThCH2C*H2*), 1.37-1.12 (14H, m, -C*H2*-), 0.88-0.8 (6H, m, -C*H3*). MS (ESI): m/z 535.7 [M-H]$^-$, calcd m/z for [M-H]$^-$ 535.18.

Methods

UV-visible absorption spectra were recorded on a Cary Cary 5000 spectrophotometer (Varian). Electrochemical measurements were carried out by cyclic-voltammetry (CV) using an Autolab PGSTAT 30 potentiostat of Eco-Chemie (Utrecht, the Netherlands), run by a PC with the NOVA 1.8 software. The working electrode was a 0.071 cm^2 glassy carbon GC disk embedded in Teflon (Amel, Italy), and the counter electrode was a platinum wire. Aqueous saturated calomel (SCE) was used as operating reference electrode, in a double bridge containing CH_2Cl_2 + 0.1 M tetrabutylammonium perchlorate (TBAP) solution, to avoid water and KCl pollution of the working solution. The measurements were carried out in a three necked glass cell, dissolving the compounds at 10^{-3} M concentration in 25 ml of CH_2Cl_2 + 0.1 M tetrabutylammonium perchlorate (TBAP) solutions.

Single crystals of **4** suitable for x-ray diffraction analysis were obtained by slow evaporation of an acetone solution of the compound. Diffraction data were recorded using Cu-K$_\alpha$ radiation in a Bruker X8 Prospector diffractometer keeping the crystal at a temperature of 100 K with a flux of liquid N_2, in order to avoid crystal melting. The data have been reduced with empirical absorption correction and structures have been solved by direct methods using SHELXL97.[12] The molecular diagrams were generated using Mercury.[13] The non-hydrogen atoms were refined anisotropically and hydrogen atoms positioned geometrically. The photovoltaic cells were prepared as described previously in Chapter 3 of this thesis. In the cases of devices provided with the functionalized oligothiophene interlayers, the cooled TiO_2 substrates were immersed in 0.4 mM solutions of the different interlayers in acetonitrile for 20 h, followed by rinsing with acetonitrile. P3HT was then spin-coated in the

same way as described previously and thermal annealing at 130 ºC for 30' in inert N_2 atmosphere was then performed for all samples, followed by 80 nm thick silver electrodes evaporation. Current density/voltage (J-V) characteristics were also measured as already described in Chapter 3.

References

[1] (a) Heimel, G.; Salzmann, I.; Duhm, S.; Koch, N. *Chem. Mater.*, **2011**, *23*, 359−377. (b) Goh, C.; Scully, S.R.; McGehee, M.D. *J. Appl. Phys.*, **2007**, *101*, 114503.

[2] (a) Hoshikawa, T.; Ikebe, T.; Kikuchi, R.; Eguchi, K. *Electrochim. Acta*, **2006**, *51*, 5286−5294. (b) Nazeeruddin, M. K.; Kay, A.; Rodicio, I.; Humphry-Baker, R.; Muller, E.; Liska, P.; Vlachopulos, N.; Graetzel, M. *J. Am. Chem. Soc.*, **1993**, *115*, 6382−6390.

[3] Boschloo, G.; Häggman, L.; Hagfeldt, A. *J. Phys. Chem. B*, **2006**, *110*, 13144−13150.

[4] Canesi, E.V.; Binda, M.; Abate, A.; Guarnera, S.; Moretti, L.; D'Innocenzo, V.; Kumar, R.S.S.; Bertarelli, C.; Abrusci, A.; Snaith, H.J.; Calloni, A.; Brambilla, A.; Ciccacci, F.; Aghion, S.; Moia, F.; Ferragut, R.; Melis, C.; Malloci, G.; Mattoni, A.; Lanzani, G.; Petrozza, A. *Energy Environ. Sci.*, **2012**, *5*, 9068-9076.

[5] Knapp, D.M.; Gillis, E.P.; Burke, M.D. *J. Am. Chem. Soc.*, **2009**, *131*, 6961-6963.

[6] (a) Martra, G. *Appl. Catal. A:General*, **2000**, *200*, 275-285. (b) Calloni, A.; Brambilla, A.; Berti, G.; Bussetti, G.; Canesi, E.V.; Binda, M.; Petrozza, A.; Finazzi, M.; Ciccacci, F.; Duò, L. *Langmuir*, **2013**, *29*, 8302-8310.

[7] Billingsley, K.; Buchwald, S.L. *J. Am. Chem. Soc.*, **2007**, *129*, 3358-3366.

[8] Eichen, Y.; Tal, S.; Abraham, Y. *US. Pat. Appl. Publ. 20110281742*, **2011**.

[9] (a) Effenberger, F.; Endtner, J.M.; Miehlich, B.; Munter, J.S.R.; Vollmer, M.S. *Synthesis*, **2000**, *9*, 1229-1236. (b) Sahu, D.; Padhy, H.; Patra, D.; Kekuda, D.; Chu, C.W.; Chiang, I.H.; Lin, H.C. *Polymer*, **2010**, *51*, 6182-6192. (c) Oyama, Y.; Harima, H.; Oshita, J. *Jpn. Kokai Tokkyo Koho* 2012144447, **2011**. (d) Gurung, S.K.; Thapa, S.; Vangala, A.S.; Giri, R. *Org. Lett.*, **2013**, *15*, 5378-5381.

[10] Porcelloni, M.; D'Andrea, P.; Rossi, C.; Sisto, A.; Ettorre, A.; Madami, A.; Altamura, M., Giuliani, S.; Meini, S.; Fattori, D. *ChemMedChem*, **2008**, *3*, 1048-1060.

[11] Pauly, A.C.; Theato, P. *J. Polym. Sci.: Part A: Polym. Chem.*, **2011**, *49*, 211-224.

[12] Sheldrick, G. M. *Acta Crystallogr. A* **2008**, *64*, 112–122.

[13] Macrae, C. F.; Bruno, I. J.; Chisholm, J. A.; Edgington, P. R.; McCabe, P.; Pidcock, E.; Rodriguez-Monge, L.; Taylor, R.; van de Streek, J. and Wood, P. A. *J. Appl. Crystallogr.* **2008**, *41*, 466–470.

PART TWO

CHAPTER 5

Insights into the Emissive Features of Phenyl End-Capped Oligothiophenes

5.1 Introduction

Conjugated organic solid-state luminescent materials have been widely studied during the past twenty years because of their excellent optoelectronic characteristics leading to applications in light emitting diodes,[1] lasers,[2] sensors[3] and biological imaging.[4] Their low cost, facile processing and flexibility also lead to their potential uses in large-scale flat panel displays. In order to develop new types of multi-color displays and tunable dye-lasers,[5] it is necessary to find ways of tailoring the luminescent properties of a particular organic chromophore. Obviously, acting on the chemical structure of the molecule has an effective and immediate consequence on its optical response. For example, by considering the series of α-oligothiophenes reported in Figure 5.1, with one to seven thienyl rings, Becker *et al.* found a steady increase in the wavelength of the emission maximum (λ_{em} max) and in the fluorescence quantum yields (ϕ_F) of the molecules in solution as the number of aromatic rings was increased.[6]
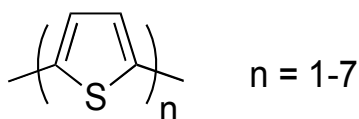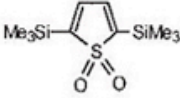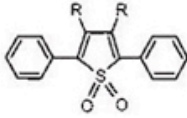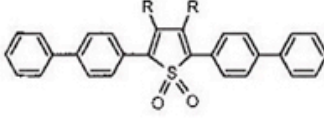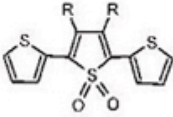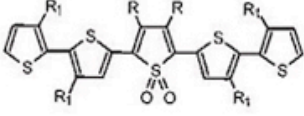

Figure 5.1. Chemical structures of α-oligothiophenes with n = 1-7.

Unfortunately, when going to the solid-state, conventional thiophene based oligomers have very low photoluminescence efficiencies, because intermolecular interactions quench radiative emission.[7] Further chemical modification may help reaching higher photoluminescence responses at the solid state. Barbarella *et al.* reported on the insertion of a central thiophene-*S,S*-dioxide moiety into the backbone of thienylene and phenylene based oligomers to bring about a large increase in the solid-

156

state photoluminescence efficiency (Figure 5.2).[8] The presence of the strongly dipolar sulfonyl group in these derivatives introduces other kinds of intermolecular interactions, which counteract the tendency to arrange in parallel layers and then decreases the number of possible non-radiative patterns for energy relaxation from the singlet excited state arising from strong intermolecular interactions.

Furthermore, for low-molecular-weight organic solid materials, it is widely recognized that the bulk optical properties are not just governed by the photo-activity of single molecules but by their collective arrangement and interaction modes.[9] During the last decade, a number of pure organic solid-state chromophore systems with controllable emission properties have been developed. The luminescent properties of these materials are generally tailored by altering the molecular packing mode within the crystal structure, *i.e.*, by forming polymorphs,[10] which are different solid crystalline phases of a specific compound resulting from different arrangements of the molecules within the solid state. Such tunable polymorph-based emissive behavior not only paves an effective way to tailor the luminescence of molecular materials, but also provides an insight into the relationship between the molecular arrangement/packing fashion and bulk optical properties. The study of the luminescent properties of π-conjugated molecular systems provides a valuable platform for understanding the way in which solid-state optical properties depend on molecular aggregation.[11]

In theory, packing arrangements, molecular conformations, intermolecular interactions and lattice energies of the same molecules in different crystalline polymorphs can all influence their fluorescence properties. Up to now, different packing arrangements that result in different intermolecular interactions have played the most significant role

(a)

	R	R1	λem max Solid-state	φF
			405	29
	methyl		470	42
	n-hexyl		485	63
	neo-pentyl		500	7
	H		500	24
	phenyl		510	42
	n-hexyl		500	70
	n-hexyl		525	45
	methyl		535	6
	phenyl		565	8
	n-hexyl	methyl	600	37
	neo-pentyl	neo-pentyl	605	6
	n-hexyl	H	625	12
	methyl	methyl	632	12
	phenyl	methyl	660	4

Figure 5.2. (a) Chemical structure, solid state photoluminescence frequencies (λem max) and quantum efficiencies (φF) of thienylene and phenylene oligomers with a central thiophene-*S,S*-dioxide moiety.

158

in tuning the luminescence properties.[12] In the case of planar π-conjugated molecular systems, the emission behavior is largely dependent on the relative orientations and degree of overlap between the chromophores: H- and J-type aggregates correspond to $\theta > 54.7°$ and $\theta < 54.7°$ respectively, where θ is the angle between the transition dipole vector and the line between the centers of the two photoactive molecules.[13] Normally, the presence of H- or J-type dimers results in blue or red-shifts, respectively, compared with the monomer luminescence.[14]

Thiophene/phenylene co-oligomers are known for their peculiar optical properties and good charge mobility, which make them suitable candidates for molecular electronics or optoelectronic applications.[15] Notably, when appropriate side groups are introduced on the conjugated backbone, solubility generally improves, paving the way for easier and cheaper solution processing.[16]

Here, we report about the luminescence properties of three analogous phenyl end-capped oligothiophenes, differing for the lateral substituents and for the length of the π-conjugated backbone, in correlation with their solid-state arrangements and thermal behaviors. Particularly, we were able to evidence polymorphism for one of this derivative and we will give a detailed structural characterization of the two crystalline phases, together with some theoretical insights aimed at explaining the differences in emissive properties found for the two polymorphs.

5.2 Results and discussion

5.2.1 Role of molecular configuration on the emissive features of phenyl end-capped oligothiophenes

The chemical structures of the three thiophene/phenylene co-oligomers are reported in Figure 5.8.
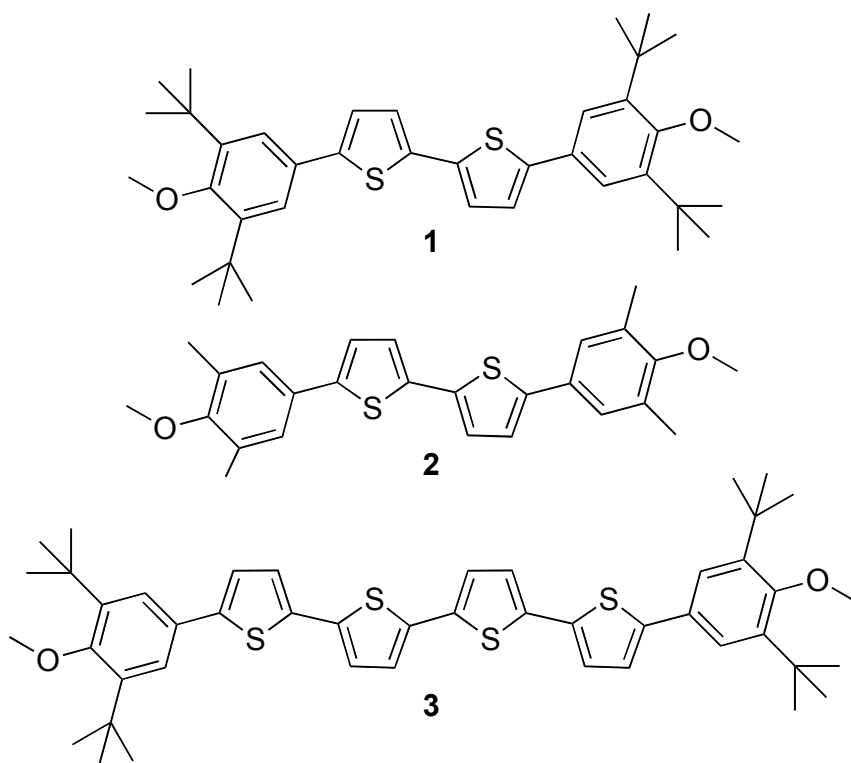

Figure 5.8. Chemical structures of thiophene/phenylene co-oligomers **1-3**.

The conjugated compounds were synthesized in one step *via* Suzuky coupling of α,α'-dibromo derivates of the central oligothienyl units with suitably functionalized phenylboronic acid (synthetic details are given in the Experimental section 5.4). Differences among the three chemical structures are found in the lateral substituents, *tert*-butyl and methyl for

1, 3 and for **2** respectively, and in the length of the central oligothienyl units, a bithiophene unit for **1** and **2** and tetrathiophene unit for **3**. The three compounds are all solids and have a yellow-orange color. Crystalline materials were obtained through slow evaporation of diethyl ether solutions of **1** and **2**, whereas for **3**, the same method resulted uneffective in obtaining good quality crystals. Crystallization was only induced by slow diffusion of methanol into a toluene solution of the compound kept at 4 °C. The crystals thus obtained were used for single crystal X-ray diffraction analysis.

The optical properties of the three species were investigated by means of absorption and photoluminescence (PL) spectroscopy.

The UV-vis absorption spectra in THF solutions are reported in Figure 5.9.
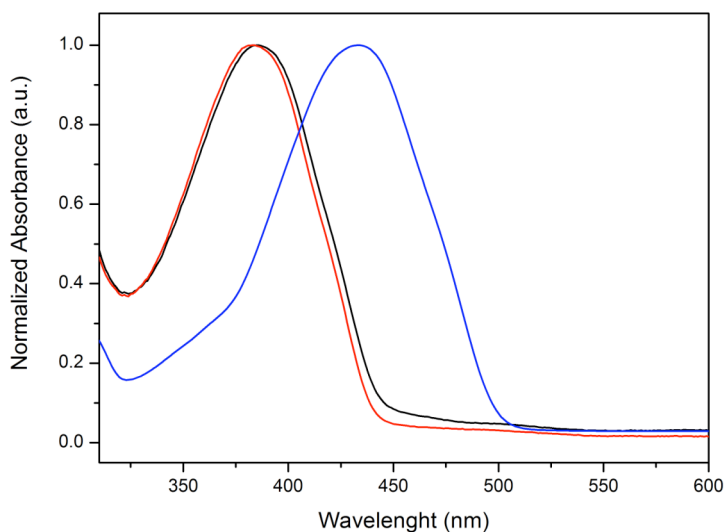

Figure 5.9. UV-vis absorption spectra of thiophene/phenylene co-oligomers **1** (black line), **2** (red line) and **3** (blue line).

The significant bathochromic shift observed for the absorption maximum of compound **3** highlights the longer π-conjugation of this derivative, having two thienyl units more than compounds **1** and **2** along the main backbone.

Diffuse reflectance spectra, converted into absorption by means of the Kubelka-Munk equation, were acquired for the three co-oligomers in crystalline form and are reported in Figure 5.10.
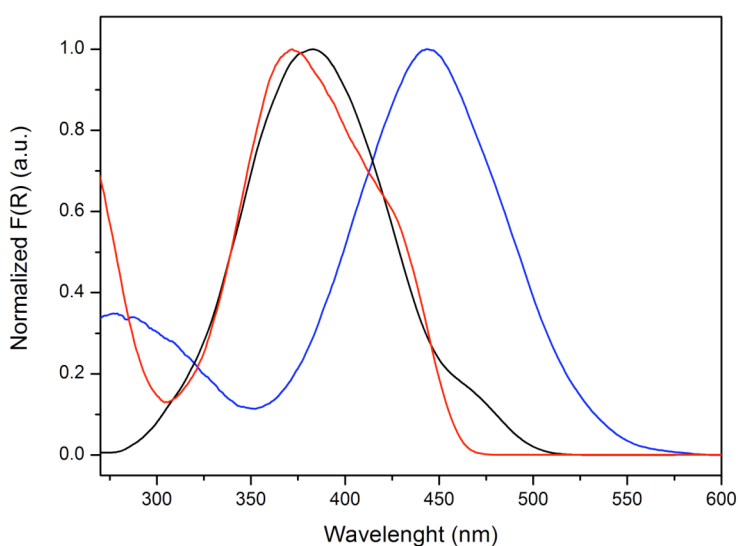

Figure 5.10. Kubelka-Munk converted diffuse reflectance spectra of **1** (black line), **2** (red line) and **3** (blue-line).

The relative positions of the three bands resemble those obtained in solution, confirming the higher extent of conjugation in compound **3** with respect to **1** and **2**. The absorption maximum of compound **3** is red-shifted with respect to solution, indicating a more extended planarity of the backbone at the solid-state, whereas in solution free-rotations about covalent bonds leads to a more distorted mean conformation. Surprisingly, a slight blue-shift is observed for the absorption maxima of

both **1** and **2** in comparison with solution spectra, indicating in this case more distorted conjugated backbones.

The photoluminescence spectra of the three derivatives in THF solution are reported in Figure 5.11.
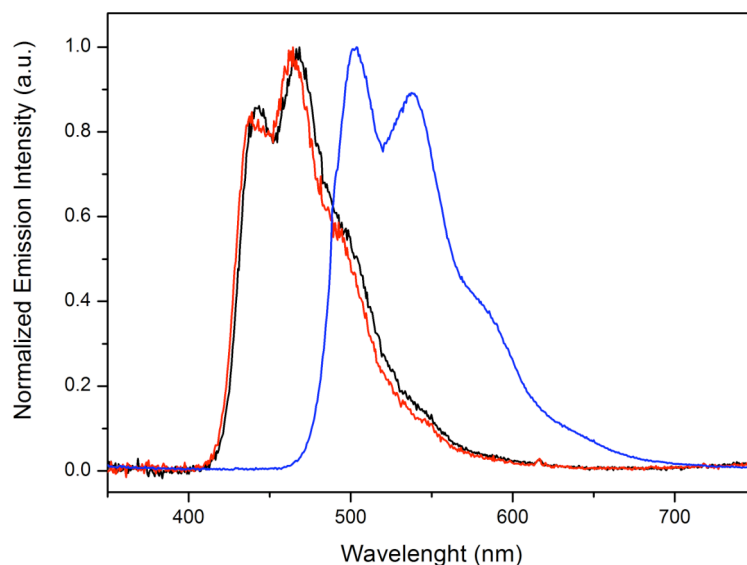

Figure 5.11. Photoluminescence spectra in THF solutions of **1** (black line), **2** (red line) and **3** (blue line).

Also in this case the spectra appear similar to the solution absorbance spectra in terms of relative positions of the bands.

The emissive features of the crystalline solid materials were also measured and the corresponding spectra are depicted in Figure 5.12. Notable differences arise from these spectra with respect to solution ones. Emission bands are all red-shifted if compared to the corresponding solution bands, resulting therefore in higher Stokes shift at the solid-state. Furthermore, the emission band of crystalline **2** appears red-shifted, enlarged and highly structured with respect to the band of crystalline **1**, which is instead quite narrow and lacking any structuring feature. This
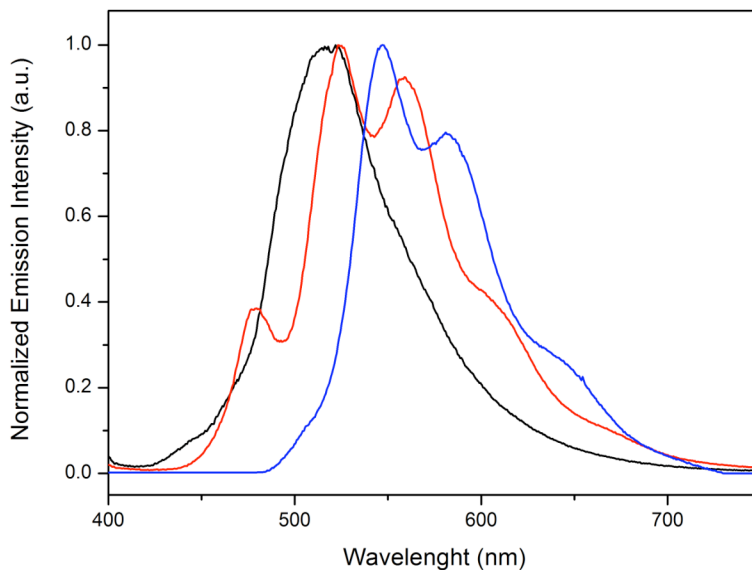
163

Figure 5.12. Photoluminescence spectra of crystalline **1** (black line), **2** (red line) and **3** (blue line).

behavior might be attributed to a more rigid conformation in crystalline **2** with respect to crystalline **1**. Table 5.1 reports the overall absorption and emission features of the three thiophene/phenylene co-oligomers in solution and in the crystalline state, together with the relative Stokes shifts.

Table 5.1. Absorption maxima, photoluminescence maxima and Stokes shifts for thiophene/phenylene co-oligomers **1-3** in solution (THF) and at the solid state.

Compound	λ_{abs} max (nm) Solution	λ_{abs} max (nm) Crystals	λ_{em}max (nm) Solution	λ_{em}max (nm) Crystals	Stokes shift (eV) Solution	Stokes shift (eV) Crystals
1	385	383	468	517	0.57	0.84
2	383	372	465	523	0.57	0.96
3	434	443	503	548	0.39	0.54

Absolute values for photoluminescence quantum yields (PLQY) were measured for the three phenyl end-capped oligothiophenes, both in solution and solid-state (Table 5.2).

Table 5.2. Photoluminescence quantum yields for thiophene/phenylene co-oligomers **1-3** in solution (THF) and at the solid state.

	PLQY (%) Solution	PLQY (%) Crystals
1	19	16
2	19	25
3	45	18

Similar values were found for the solution PLQY of compounds **1** and **2**, as expected from the strong similarity between their respective conjugated backbones. Indeed, the PLQY of compound **3** in solution is more than double, because of longer conjugation length. Solid-state PLQY are noticeably high if compared to other thiophene derivatives, for which a photoluminescence quenching at solid state is usually observed.[7] Moreover, the presence of methyl groups (**2**) compared to the more steric demanding *tert*-butyl groups (**1**) was expected to favor intermolecular quenching effects due to stacking of conjugated moieties, but the higher PLQY found for crystalline **2** with respect to **1** goes in the opposite direction. A remarkable quenching is found for **3** when going from solution to solid state. The reason is certainly found in the existence of strong intermolecular interactions in the crystalline state, which activate non-radiative pathways for the decay from the lower singlet excited state. These results suggested carrying out a deeper analysis of the effective intermolecular interactions occurring in these thiophene/phenylene co-oligomers.

Thermal behaviors of the three derivatives were studied by differential scanning calorimetry (DSC). Figure 5.13 shows the DSC traces obtained for the three crystalline materials. Melting points extracted from the first heating scan are reported in Table 5.3. The lower melting temperature of crystalline thiophene/phenylene co-oligomer **2** is accompanied by a significant reversibility in the melting-crystallization processes: recrystallization from the melt takes place during cooling at a temperature slightly lower, but very close to the melting one (T_c peak = 174 °C). On the contrary, recrystallization of compounds **1** and **3** after melting is induced only during the second heating scans, indicating a pronounced resistance of the two derivatives to organize in an ordered fashion at the solid-state. The difference between the two thermal behaviors is most likely attributed to the different lateral substituents on the phenyl rings. Indeed, the bulky *tert*-butyl groups seem to hinder intermolecular organization of the materials in the crystalline state, whereas methyl groups seem to favor crystallization. The unusual first heating trace observed for crystalline **3**, which shows two apparent melting peaks at 194 and 220 °C (T_m peaks), is likely related to polymorphism and will be discussed thoroughly in the next paragraph. On the other hand, single phases are apparent for both **1** and **2**, rationally coinciding with the crystal phases obtained from slow solvent evaporation. X-ray diffraction data are reported in Table 5.4. Crystal structures were solved by Prof. S.V. Meille at the "G. Natta" Department of Politecnico di Milano. Figure 5.14 illustrates the crystal packing modes of compounds **1** and **2**. Crystal structure analysis of the two phenyl end-capped α-bithiophenes reveals loose packing modes in both cases, with molecules consistently isolated from one another in the tri-dimensional crystal. This excludes the occurrence of a pronounced
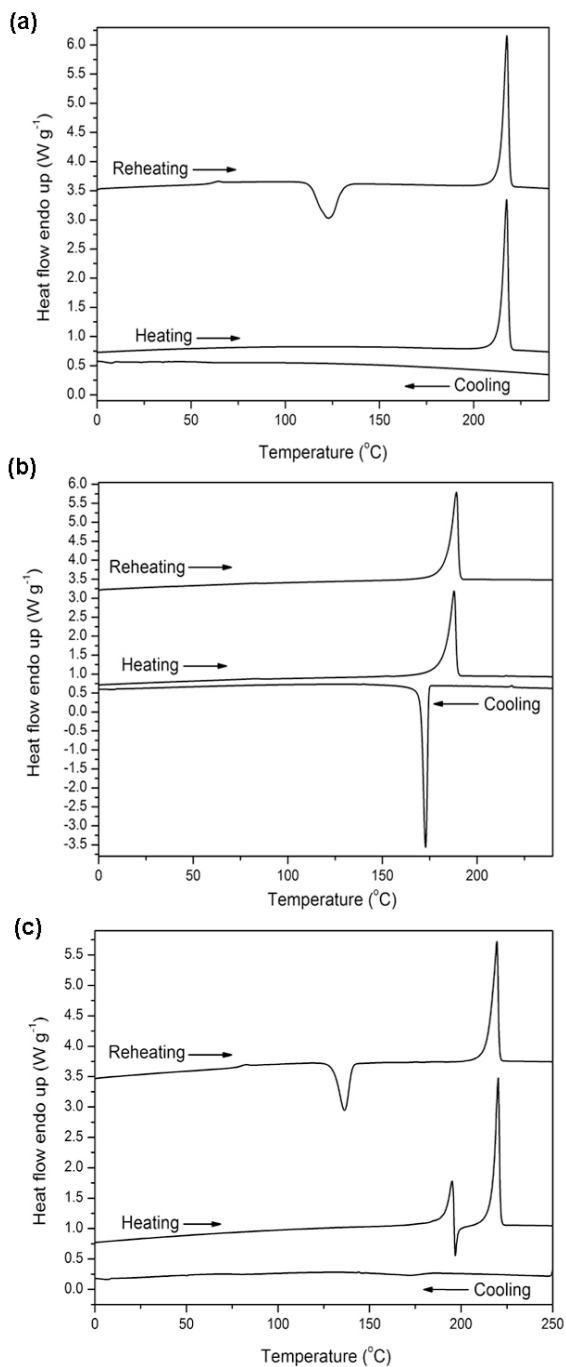
Figure 5.13. DSC heating, cooling and reheating scans at constant rates of 10 °C min^{-1} obtained starting from crystalline samples of (a) compound **1**, (b) compound **2** and (c) compound **3**.

Table 5.3. Melting points for thiophene/phenylene co-oligomers **1**-**3** extracted from the first DSC heating scans (onset and peak temperatures are given).

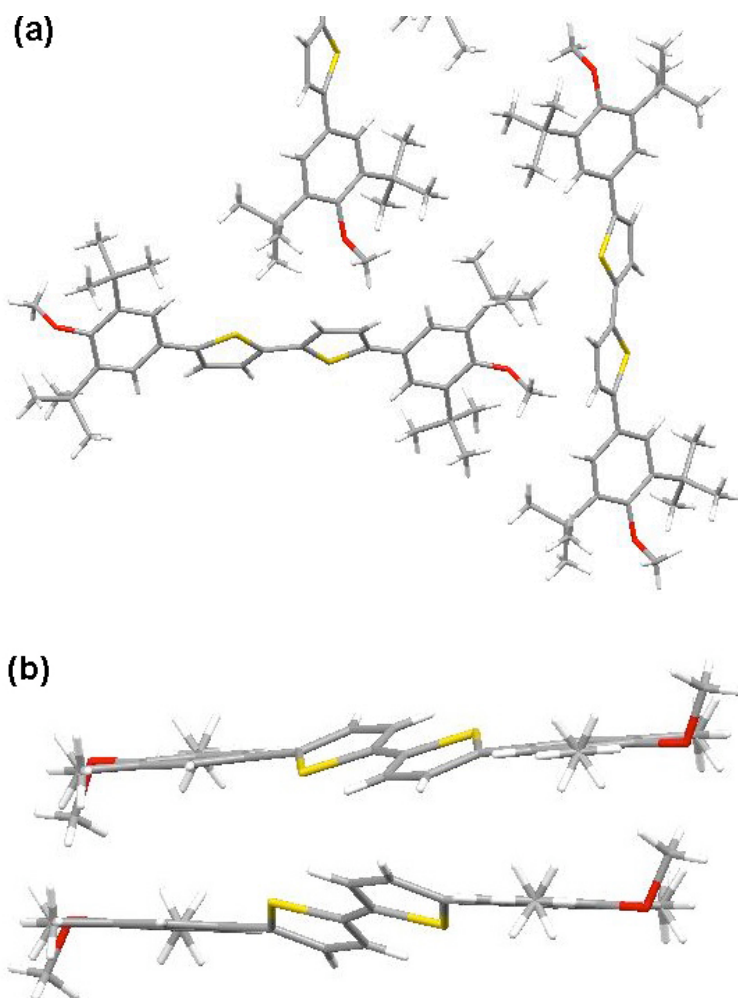|	T_m (°C) Peak	T_m (°C) Onset
1	217	214
2	189	184
3	194 (first peak)	190 (first onset)
	220 (second peak)	216 (second onset)

Figure 5.14. Crystal packing modes of (a) compound **1** along the *a*-axis and (b) compound **2** along the *b*-axis.

168

photoluminescence quenching originated from the stacking of the aromatic backbones. The presence of the methyl substituents in compound **2** does not result therefore in tighter packing, as was expected.

Table 5.4. Crystallographic information and structure refinement for **1** and **2**.

Compound	1	2
Formula	$C_{38}H_{50}O_2S_2$	$C_{26}H_{26}O_2S_2$
F_W	602.9	434.59
Crystal system	Monoclinic	Triclinic
Space group	$P21/c$	P-1
a (Å)	6.1220(6)	8.0462(5)
b (Å)	19.4400(14)	9.0710(8)
c (Å)	15.1629(12)	16.8778(14)
α (deg)	90.00	80.939(8)
β (deg)	95.857(8)	85.830(7)
γ (deg)	90.00	69.725(7)
V (Å^3)	1795.1(3)	1140.90(16)
T (K)	300(2)	293(2)
Z	2	2
F (000)	652	460
ρ_{calcd} (g cm^{-3})	1.115	1.265
μ (mm^{-1})	1.559	2.262
T_{min}, T_{max}	0.401, 0.692	0.28091, 0.85070
Crystal size (mm^3)	0.58×0.10×0.10	0.82×0.70×0.07
θ_{max} (deg)	67.49	40.455
No. Refl. collected	4263	4884
R_{int}	0.0454	0.0981
No.unique	3038	4020
No. with $I> 2\sigma(I)$	2299	3655
Refined parameters	218	272
Restraints	27	-
Final R indices [$I> 2\sigma(I)$]	$R1 = 0.0672$, $wR2 = 0.1762$	$R1 = 0.0737$, $wR2 = 0.1962$
R indices (all data)	$R1 = 0.0826$, $wR2 = 0.1938$	$R1 = 0.0708$, $wR2 = 0.1914$
$\Delta\rho$[eÅ^{-3}]	-0.418, 0.583	-0.586, 1.084

5.2.2 Role of solid-state conformation on the emissive features of bulky-group substituted phenyl end-capped quaterthiophene

Polymorphism in quaterthiophenes (4T) is widespread, ranging from unsubstituted quaterthiophene, which may adopt two similar crystal forms differing for the number of molecules in the unit cell,[16] to α- and β-substituted derivatives, for which conformational polymorphs have been found.[17,18] In the latter cases, the formation of one particular phase has general relevance and studies aimed at understanding phenomena behind phase transitions can guide the choice of the right processing conditions for the preparation of active layers with specific optoelectronic responses. Here we describe the case of compound **3**, a 4T derivative showing two stable polymorphs that can be produced selectively (Figure 5.15). Phase-**I** is formed from solution, whereas a second, more stable phase (phase-**II**) is obtained by controlled thermal treatment. Unlike the case reported by Barbarella e*t al.*,[17] evaporation from solution selectively affords only phase-**I**. This has been thouroghly verified by checking the unit cell of a large number of single crystals prepared from solution. As reported previously, DSC analysis performed on phase-**I** crystals, shows the formation of a high temperature polymorph (phase-**II**) after melting of the starting phase (Figure 5.13). The higher melting point of phase-**II** suggests that it is thermodynamically more stable than phase-**I** differently from other cases,[18] in which the most stable phase is obtained from solution, whereas a less stable phase is formed by rapid cooling of the melt. Attempts to grow single crystals of phase-**II** from solution, including seeding methods, were unsuccessful,[19] always resulting in phase-**I** crystals. Keeping single crystals of phase-**I** at 200 °C for 30 min resulted in the conversion into phase-**II** single crystals of sufficient size (> 50 μm)
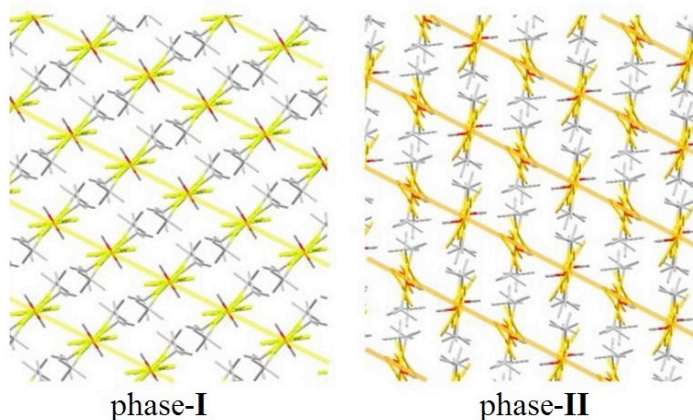
phase-**I**   phase-**II**

Figure 5.15. Crystal structures of phase-**I** and phase-**II**. Crystal structures are shown along the direction of the aromatic backbone (yellow and orange thick lines show molecular layers characterized by significant inter-aromatic intermolecular interactions within structures).

and quality for high resolution X-ray diffraction. An interesting aspect of this transition is that also polycrystalline material obtained from large crystals of phase-**I** retains the needle shape of the starting crystals (Figure 5.16c, 5.17c and 5.18). From DSC it is possible to evidence the selective formation of sole phase-**II** after complete melting of phase-**I** crystals at 220 °C, followed by cooling and induced re-crystallization at 150 °C. The subsequent heating scan of the re-crystallized material furnishes indeed only the high-temperature melting peak, characteristic of phase-**II** (Figure 5.16).

From solution, **3** (phase-**I**) crystallizes in space group P-1, with half a molecule in the asymmetric unit and a single **3** molecule in the unit cell (Table 5.5 and Figure 5.17a). Crystal structure was solved by Dr. E. Parisini and Dr. J.M. Rujas at CNST-IIT@Polimi. The quaterthiophene moiety is in an all-*trans* conformation and shows good planarity (r.m.s.d. = 0.08 Å) while the terminal phenyl rings form a 35° angle with respect to the mean thiophene plane. In phase-**I** crystals molecules arrange
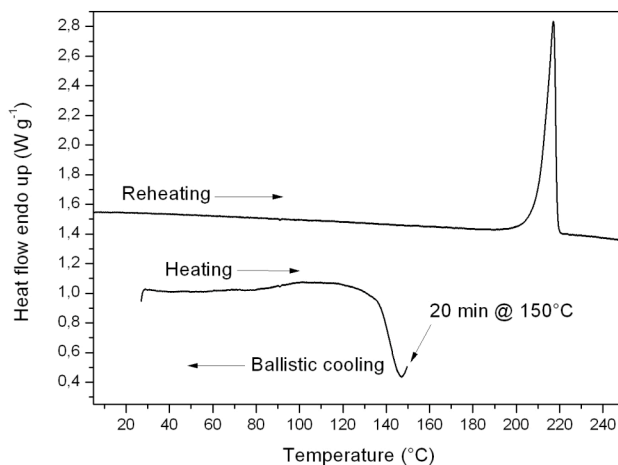
172

Figure 5.16. DSC heating and reheating scans at constant rates of 10°C min^{-1} obtained starting from crystalline material obtained from solution which was completely melted at 220 °C and cooled to room temperature at the same rate of 10 °C min^{-1}. After the first heating scan here presented, the material was kept at the re-crystallization temperature of phase-**II** (150 °C) for 20 min, in order to induce complete re-crystallization. The reheating scan shows the presence of the only melting peak due to phase-**II**.

parallel in loose stacks (Figures 5.15 and 5.17) deviating from the herringbone motif typically observed in most substituted and unsubstituted oligothiophenes.[16] The steric requirements of *tert*-butyl substituents are plausibly a key factor leading to the phase-**I** molecular arrangement. The space group of phase-**II** is also *P*-1, but the asymmetric unit is now defined by two independent half molecules (Table 5.5 and Figure 5.17a) and hence two different molecules are present in the unit cell. Since the midpoint of both molecules lies on crystallographic centers of inversion, the central interthiophene bond is *trans* in both **3** molecules. In one case the tetrathiophene ring system is arranged in a *cis-trans-cis* planar conformation (out-of-plane r.m.s.d. = 0.06 Å) while the second molecule in phase-**II** maintains the all-*trans* conformation found

173

Table 5.5. Crystallographic information and structure refinement for the two polymorphs of **3**.

| Polymorph	Phase-**I**	Phase-**II**
Crystal system	Triclinic	Triclinic
Space group	P-1	P-1
a (Å)	5.8691(6)	10.0773(16)
b (Å)	14.2212(15)	12.626(2)
c (Å)	14.2606(14)	17.705(4)
α (deg)	113.921(7)	82.176(14)
β (deg)	100.286(7)	77.112(12)
γ (deg)	93.039(7)	76.890(13)
V (Å^3)	1060.09(19)	2129.9(7)
T (K)	296(2)	296(2)
Z	1	2
F (000)	410	820
ρ_{calcd} (g cm^{-3})	1.202	1.196
μ (mm^{-1})	2.326	2.316
T_{min}, T_{max}	0.830, 0.877	0.6298, 0.9131
Crystal size (mm^3)	0.08×0.08×0.06	0.22×0.10×0.04
θ_{max} (deg)	67.82	58.49
No. Refl. collected	11990	23751
R_{int}	0.0643	0.0630
No.unique	3645	7154
No. with $I> 2\sigma(I)$	2486	3753
Refined parameters	242	483
Restraints	-	-
Final R indices [$I> 2\sigma(I)$]	$R1 = 0.0435$, $wR2 = 0.1172$	$R1 = 0.0890$, $wR2 = 0.2615$
R indices (all data)	$R1 = 0.0843$, $wR2 = 0.1510$	$R1 = 0.1575$, $wR2 = 0.318$
$\Delta\rho$[eÅ^{-3}]	-0.486, 0.424	-0.337, 1.091
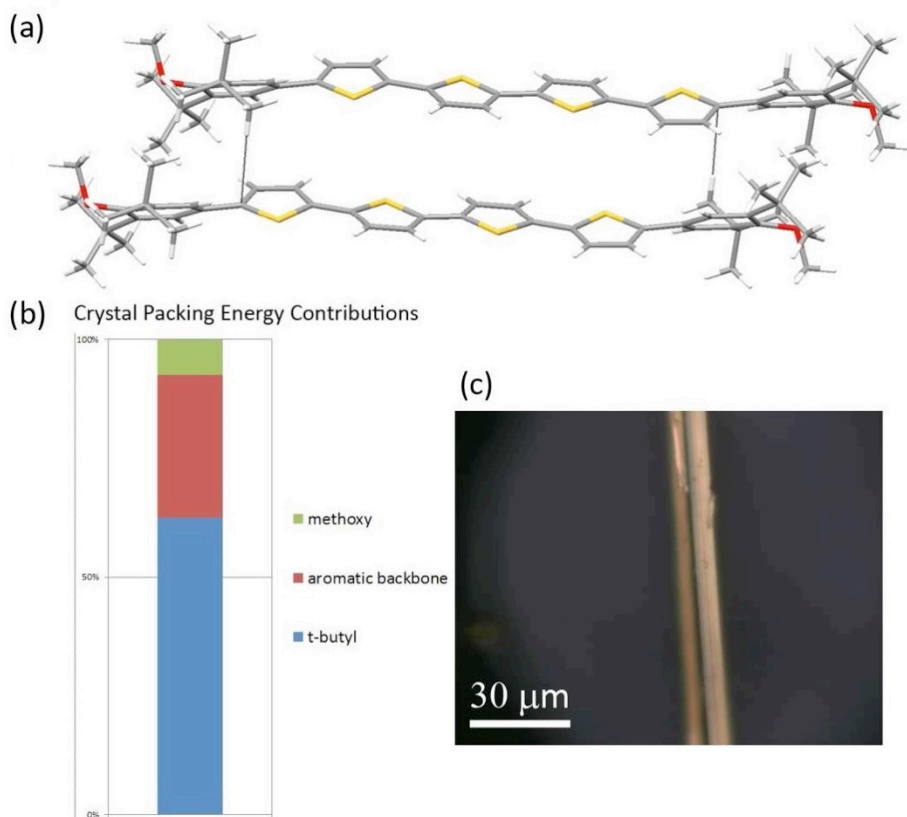
Figure 5.17. (a) Crystal structure of phase-**I**. View of two molecules showing short contacts stemming from alkyl C-H···π interactions (shown as black lines, 2.796 Å). (b) Crystal packing energy contributions of methoxy, aromatic backbone and *tert*-butyl moieties. (c) Needle-like crystal of phase-**I**.

in phase-**I**, however with a more pronounced distortion from planarity (r.m.s.d. = 0.19 Å). The phenyl rings in both phase-**II** conformers remain tilted at about 30° from the plane of the adjacent thiophenes. A further relevant feature of the phase-**II** structure is the loss of the parallel stacking arrangement observed in phase-**I**, as the two independent molecules form a T-shaped dimer in which the *cis-trans-cis* conformer faces edge-on the all-*trans* molecule at an angle of 71°. The stacking of the **3** molecules in phase-**II** is thus a herringbone-like packing (Figure
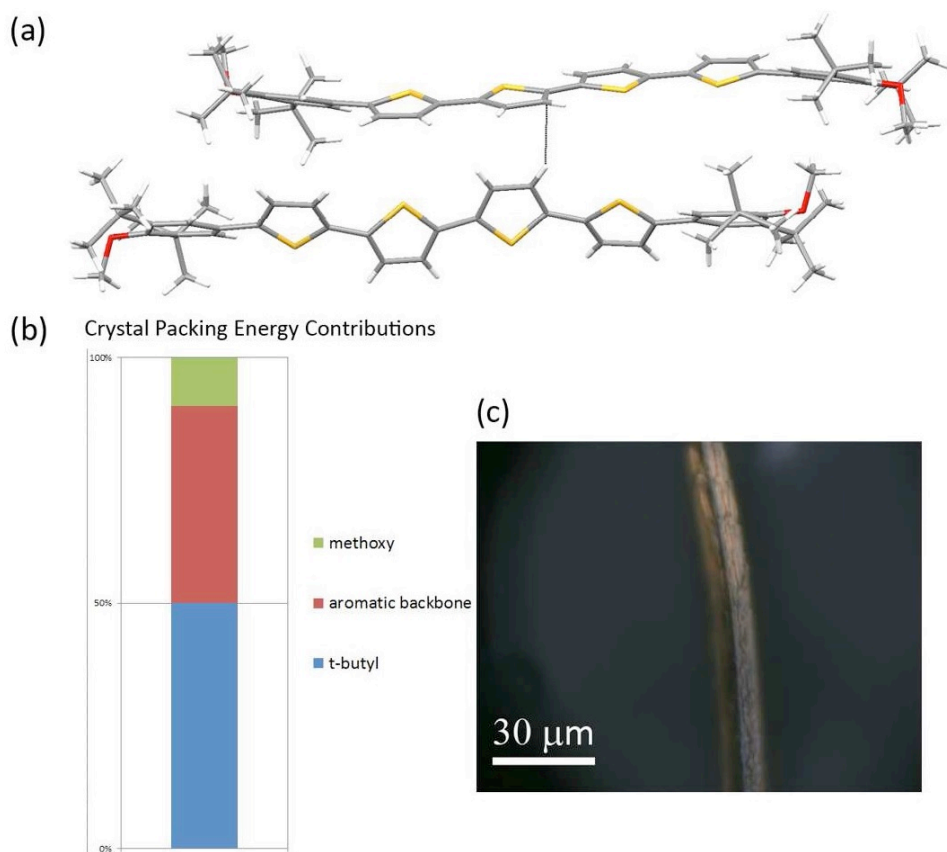
Figure 5.18. (a) Crystal structure of phase-**II**. View of two molecules showing shot contacts stemming from alkyl C-H···π interactions (shown as black lines, 2.875 Å). (b) Crystal packing energy contributions of methoxy, aromatic backbone and *tert*-butyl moieties. (c) Crystal of phase-**I** after transformation to phase-**II** polycrystalline aggregate.

5.18a) and not the parallel stacking found in phase-**I**. As a consequence the slightly denser (+0.5%) phase-**I** allows for relatively large voids where the loose packing between tetrathiophene units occurs. These voids are absent in phase-**II** presenting a lower density while its melting point is much higher. The optical properties of thiophene/*p*-phenylene co-oligomers have been extensively studied due
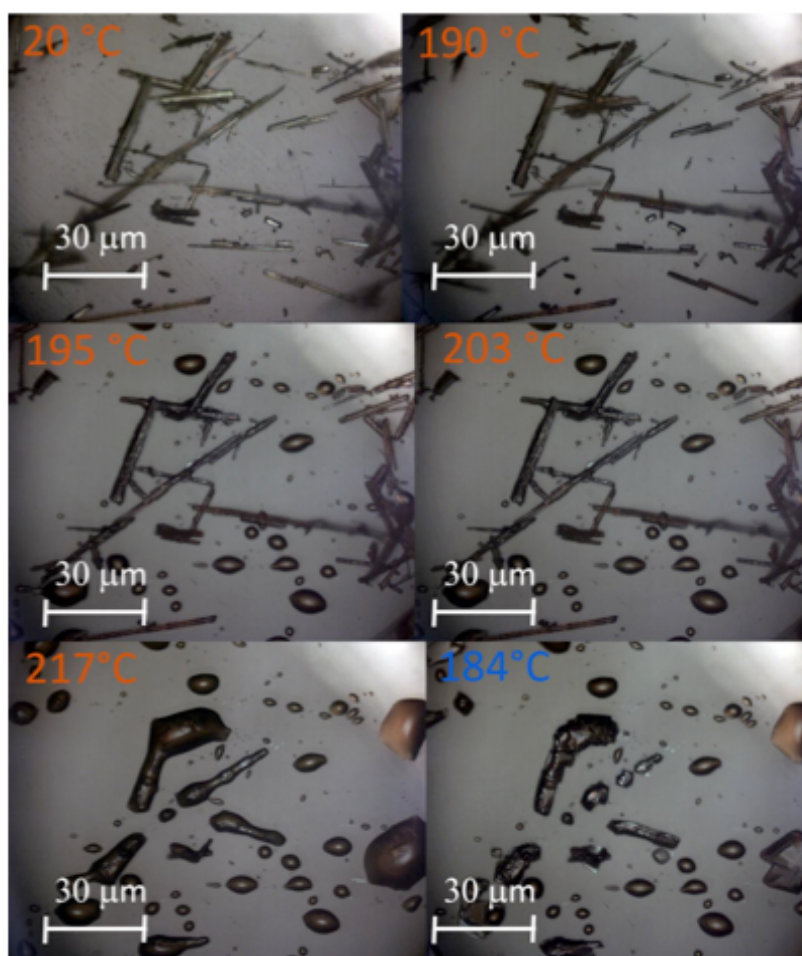
176

Figure 5.19. Monitoring of the structural transformation through optical microscopy equipped with a hot plate stage. Single crystals of phase-**I** were heated from r.t. at a constant heating rate (10 °C/min) up to 170 °C. During this heating interval, single crystals did not show any physical change and remained crystalline. Then, the heating rate was slowed to 1 °C/min up to 195 °C and kept for 20 minutes. At that temperature, smaller phase-**I** crystals melted while others retained their shape though losing single crystal features. Interestingly, from molten crystals of phase-**I** new crystals appeared and remained stable until 217 °C, fusion onset temperature of phase-**II**. Aggregates that remained solid through the first thermal event at 195°C also remained stable until the second fusion. This observation hints at the possibility of solid-solid transformation from phase-**I** to phase-**II**. Recrystallization of glassy aggregates could only be induced upon reheating from r.t.

177

to the interest in their emissive properties. These properties are sharply enhanced with respect to parent thiophene oligomers and this makes this class of materials promising for light amplification and for a variety of optoelectronic applications.[20] The two polymorphs of compound **3** provide an excellent opportunity to further investigate structure-properties relationship for these materials. Photoluminescence (PL) spectroscopy (Figure 5.20) shows interestingly a 19 nm bathochromic shift for the PL band as we move from phase-**I** to phase-**II**. A similar shift is observed for the onset of the excitation profiles (Figure 5.21). The measurements were taken by Dr. F. Villafiorita Monteleone and Dr. C. Botta at ISMAC-CNR.
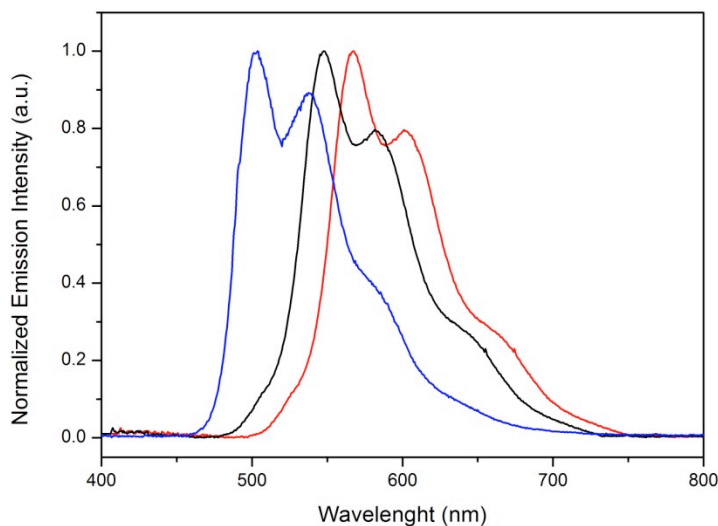

Figure 5.20. Photoluminescence spectra (λ_{exc}=420 nm) of **3** phase-**I** (black line), phase-**II** (red line) and THF solution (blue line).
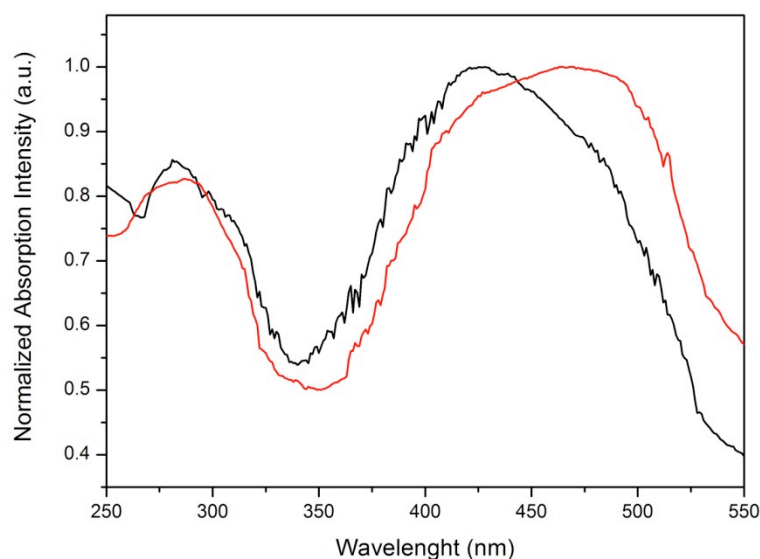
Figure 5.21. Excitation profiles of phase-**I** (black line) and phase-**II** (red line).

At the same time, quantum efficiency decreases from 18% for phase-**I** to 11% for phase-**II**, while amorphous films show a 4% PL value, confirming the high relevance of the crystalline packing.

As the two polymorphs show different photoluminescence properties and remarkably different structures (Table 5.6), they represent an ideal case to correlate structural information with emission behavior. Quantum mechanics (QM) calculations were used to support the study. Calculations and data interpretation were carried out by Prof. A. Famulari at the "G. Natta" Department of Politecnico di Milano.

In order to make sense of the apparently conflicting structural, thermal and emissive properties of the two polymorphs, the packing of **3** molecules in both polymorphs has been analyzed by solid state density functional (DFT) methods.[21] The analysis performed on the phase-**I** crystal structure yielded a sublimation energy of 40.0 kcal mol^{-1}. The relative contributions to the crystal packing energy are depicted as a

Table 5.6. Structural and PL properties for the two polymorphs of **3**.

	Density (g cm^{-3})	ΔE_{Subl} (kcal mol^{-1})[a]	Voids[b]	m.p. (°C)	PLQY	λ_{em} max (nm)
Phase-**I**	1.202	+0.6	3.4%	195	18%	548
Phase-**II**	1.196	0.0	0.0%	217	11%	567

[a] Obtained from solid state DFT calculations (details are reported later in the text).

[b] Voids were calculated with 1.2Å probe radius and 0.2 grid spacing on Mercury CSDS.

histogram (Figure 16b). A 63% contribution is due to the *tert*-butyl moieties that form C–H···π interactions between neighboring molecules along the stacking direction. DFT calculations suggest a slightly higher sublimation energy ($\Delta E_{II-I} \approx$ +0.6 kcal/mol) for the higher melting polymorph phase-**II** consistent with calorimetric data. *Tert*-butyl groups still majorly contribute to crystal packing but do not appear to be involved in any type of specific stabilizing interactions: this might explain the large thermal parameters found for the atoms of these substituents, likely characterized by substantial conformational freedom within the crystal lattice. The packing energy of phase-**II** involves comparable contributions of the aromatic backbone and *tert*-butyl groups: 50% and 40% respectively. This is consistent with the loss of alkyl C–H···π interactions and the arising of aromatic C–H···π interactions between β-hydrogens of thienylene moieties in phase-**II**.

To a first approximation the effect of molecular conformations and dimeric intermolecular interactions on the optical properties of two polymorphs can be at least partly understood with reference to HOMO-LUMO energy levels. These were calculated for both phases within the DFT framework used for solid state energy calculations, considering both isolated molecules and neighboring pairs. For phase-**I**, no significant variation is apparent comparing the isolated molecule to a stacked pair,

180

consistent with the equivalence of all molecules in this crystal form. On the other hand, for the isolated all-*trans* and *cis-trans-cis* conformers in phase-**II**, HOMO-LUMO gaps are higher than for molecules in phase-**I**, in disagreement with the bathochromic shift in the PL spectrum. This observation suggests a larger influence of intermolecular interactions in phase-**II**. In fact, a smaller gap results when looking at the dimer frontier orbitals in this phase. Interestingly, the DFT method used agrees quite nicely with the experimental PL red shift (0.077 eV) obtained comparing the gaps for phase-**I** and phase-**II** dimers ($|\Delta(Gap_{II}-Gap_I)|= 0.087$ eV). We stress that this consideration must be considered qualitative at best, since various unproven assumptions are needed for such a simple correlation to hold.[22] Another peculiar feature evidenced by calculations on the phase-**II** dimer is that the HOMO, can be visualized as residing on the all-*trans* molecule while the LUMO is on the *cis-trans-cis* conformer (Figure 5.22).
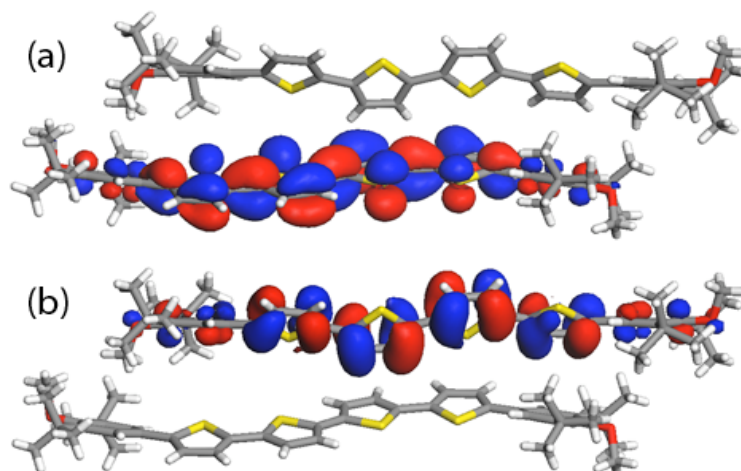

Figure 5.22. Calculated LUMO (a) and HOMO (b)orbitals for phase-**II** dimer.

This result suggests a dimer excited state with partial charge transfer character that could account for both the PL bathochromic shift and QY

181

reduction.[23] The same frontier orbitals are involved in the permitted optical transition of the dimer. For oligothiophenes[24] and thiophene/phenylene co-oligomers[25] the absorption and emission properties are generally correlated to more pronounced H-like features in the solid state.

These lead frequently to a non-emissive or weakly emissive 0–0 transition in the photoluminescence spectra of the crystals,[26] as also reported for odd-numbered oligothiophenes.[27] In this perspective the relatively high QY found especially for phase-**I** is unusual since H aggregates, characterized by strong aromatic intermolecular interactions, are known to quench light emission. In optically active materials showing H-aggregate structural features transition probabilities are governed by coupling of transition dipole moments (TDM) arranged in a stacked parallel fashion. By extracting 1-D clusters of molecules along the closer inter-aromatic intermolecular interactions direction (Figures 5.15 and 5.23), the relative arrangement of molecular long axes appears to be H-like, with a slight deviation found for phase-**II** (1.68° relative misorientation due to the presence of two independent molecules in the unit cell).

To confirm these qualitative considerations, calculations of excited states and TDMs have been carried out by using the semiempirical ZINDO method, which provides accurate results for the excited states of conjugated molecules.[28] TDMs' vectors lie within the thiophene plane for all molecules, deviating from the thiophene axis of 1.08°, 2.01° and 2.21° for the *trans*-molecule of phase-**I**, *trans* and *cis*-molecule of phase-**I** respectively. The effect of packing on the couplings amongst TDMs' vectors in phase-**I** is quite simple, due to the presence of only one
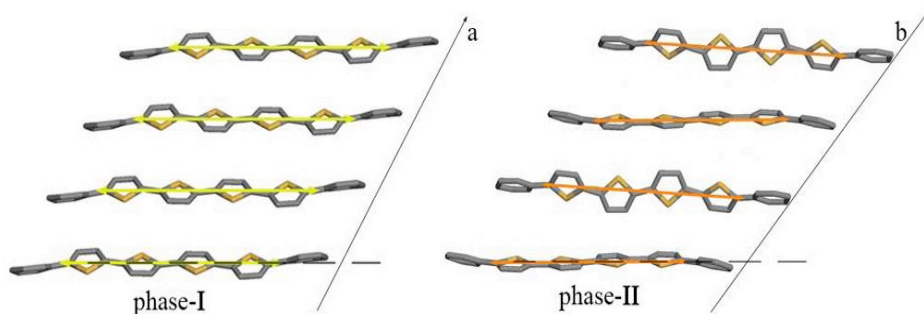
Figure 5.23. 1D clusters of closest neighboring molecules of phase-**I** (along the *a*-axis) and phase-**II** (along the *b*-axis), with superimposed yellow and orange arrows representing calculated transition dipole moments, arranged in parallel stacks, a feature of ideal H-aggregate model.

molecule per unit cell, i.e. all molecules, hence all TDMs, are stacked along the *a*-axis in a parallel fashion. For phase-**II** the situation is more complex, but since the misalignment between independent molecules and between TDMs and each molecule does not exceed 6° altogether, TDMs' vectors can be considered parallel within a sensible approximation. Indeed molecular stacks and therefore of TDMs' vectors can both be regarded as H-aggregates but surprisingly it is the one closer to the ideal H-model (the angle between the aromatic plane and the stacking axis is closer to 90° for phase-**I**) that shows the highest QY. Therefore the drop in PL and the red shift can only be explained by the relative quantification of intermolecular interactions and molecular conformation within the two crystal structures.

5.3 Conclusions and outlook

In conclusion, we presented a series of three thiophene/phenylene co-oligomers showing different optical properties, related to their molecular configurations and consequent solid-state arrangements. Furthermore, the

183

substituted quaterthiophene species, compound **3**, shows a remarkable structural polymorphism since it exists in two stable polymorphic forms, which can be selectively obtained. The results of solid-state DFT calculations, coupled with crystallographic data, not only confirm the relative stability of the two polymorphs but also help to understand and quantify intermolecular interactions between aromatic thienylene moieties. The *tert*-butyl groups act as spacers preventing effective inter-aromatic interactions between neighboring molecules and allow for relatively high PL in phase-**I**. The active contributions to crystal packing of *tert*-butyl substituents through C–H⋯π, effectively lock the relative position of molecules in phase-**I** to relatively high temperatures. On the other hand the presence of the two different backbone conformations of **3** in phase-**II** allows for tighter inter-aromatic packing, filling voids around aromatic moieties caused by the bulky substituents in phase-**I**. In this way the aromatic backbone interact more strongly, causing a drop in PL, to values which remain however much larger than in amorphous films. The structural data presented here provide new and deeper insight into the optical properties of **1**, **2** and **3**,[29] which are likely to address widely applicable principles. Our study highlights the role of non-aromatic side groups together with a stringent control over crystallization conditions to obtain well-defined molecular packing features of the aromatic backbone, which in turn may allow modulation of PL quantum yield.

5.4 Experimental

Materials

All chemicals were purchased from commercial suppliers and used without further purification. 3,5-di-*tert*-butyl-4-methoxyphenylboronic acid   and   5,5''''-dibromo-2,2':5',2'':5'',2'''-tetrathiophene   were

synthesized following literature procedures.[30,31] ^{1}H NMR and ESI-MS spectra were acquired as described in Chapters 3 and 4.

The thiophene/phenyl co-oligomers were synthesized according to the following procedure.

5,5'-Bis-(3,5-di-tert-butyl-4-methoxy)phenyl-2,2'bithiophene (**1**). 5,5''-Dibromo-2,2'-bithiophene (0.46 g, 1.42 mmol) and Pd(PPh$_3$)$_4$ (0.162 g, 0.14 mmol) were dissolved in argon degassed DME (50 ml). After stirring for 10 min, 3,5-di-tert-butyl-4-methoxyphenylboronic acid (0.73 g, 2.94 mmol) and solid NaHCO$_3$ (1.1 g, 13 mmol) were added, together with argon degassed H$_2$O (25 ml) and the resulting mixture was refluxed for 15 h. After cooling to room temperature, it was poured into water (30 ml) and extracted with diethyl ether (3 x 30 ml). Organics were combined, dried (Na$_2$SO$_4$), filtered and concentrated. Column chromatography on silica gel eluting with hexane/CH$_2$Cl$_2$ 8:2 afforded the pure product as a bright yellow solid (0.49 g, 57%). ^{1}H-NMR (400 MHz, CDCl$_3$, ppm): δ 7.48 (4H, s), 7.14 (4H, s), 3.72 (6H, s), 1.47 (36H, s). MS (ESI): m/z [M+] 602.6; calcd m/z [M+] 602.93.

5,5'-Bis-(3,5-dimethyl-4-methoxy)phenyl-2,2'bithiophene (**2**). The compound was synthesized following the same procedure described for **1** starting from 5,5''-dibromo-2,2'-bithiophene (0.42 g, 1.3 mmol), 3,5-dimethyl-4-methoxyphenylboronic acid (0.486 g, 2.7 mmol), Pd(PPh$_3$)$_4$ (0.15 g, 0.13 mmol) and NaHCO$_3$ (0.982 g, 11.7 mmol) in degassed DME/H$_2$O mixture (50 ml/25 ml). Purification through flash chromatography (silica gel, hexane:CH$_2$Cl$_2$ 7:3) gave **2** as a pale yellow crystalline solid (0.35 g, 62%). ^{1}H-NMR (400 MHz, CDCl$_3$, ppm): δ 7.18 (4H, s), 7.04 (4H, m), 3.67 (6H, s), 2.25 (12H, s). MS (ESI): m/z [M+] 434.8; calcd m/z [M+] 434.61.

5,5'-Bis-(3,5-di-tert-butyl-4-methoxy)phenyl-2,2':5',2'':5'',2'''-tetrathiophene (**3**) This compound was obtained with the same procedure described for **1** starting from 5,5''''-dibromo-2,2':5',2'':5'',2'''-tetrathiophene (0.85 g, 1.74 mmol), 3,5-di-tert-butyl-4-methoxyphenylboronic acid (1 g, 4 mmol), $Pd(PPh_3)_4$ (0.17 g, 0.15 mmol) and $NaHCO_3$ (1.34 g, 16 mmol) in degassed DME/H_2O mixture (150 ml/75 ml: solvent quantities were increased consistently because of the low solubility of the 5,5''-dibromo-2,2':5',2'':5'',2'''-tetrathiophene starting material). Column chromatography eluting with hexane:CH_2Cl_2 9:1 gave pure **3** as an orange powder

(1.33 g, 58%). ^{1}H-NMR (400 MHz, $CDCl_3$, ppm): δ 7.48 (4H, s), 7.13 (4H, s), 7.09 (4H, m), 3.73 (6H, s), 1.48 (36H, s). MS (ESI): *m/z* [M+] 767.7; calcd *m/z* [M+] 767.21.

Single crystals of **1**, **2** and **3** suitable for x-ray diffraction analysis were obtained as described in the text.

Experimental methods

UV-Visible absorbance spectra were recorded as described in Chapters 3 and 4 of this thesis. Diffuse reflectance measurements were obtained on the same instrument equipped with an integrating sphere reported in Chapter 2, dispersing the crystalline samples in a $BaSO_4$ matrix and placing them at the bottom of the sphere.

Photoluminescence (PL) spectra were recorded on a 270M SPEX spectrometer equipped with a N_2 cooled CCD (charge-coupled device) detector, and by exciting with a Xenon lamp connected to a Gemini monochromator for the wavelength selection. The spectra were corrected for the instrument response. The PL quantum yields (QY) on solid-state materials were obtained using a home-made integration sphere following the procedure already reported.[32] Photoluminescence excitation profiles

(PLE) of the different systems were obtained by integrating the emission spectra while sweeping the excitation wavelengths, and using Rhodamine B as reference to correct for the variations in the excitation intensity.

Diffraction data were recorded and reduced as reported in Chapter 4. The molecular diagrams were generated using Mercury.[33] The non-hydrogen atoms were refined anisotropically and hydrogen atoms positioned geometrically.

DSC measurements were performed on a DSC 8500 Perkin-Elmer apparatus working under N_2 flow (20 ml min^{-1}). Crystalline samples were loaded into unsealed standard aluminium pans, equilibrated at 0 °C, heated to 250 °C at a rate of 10 °C min-1 and then cooled down again to 0 °C at the same rate. The cycle was repeated to check the reversibility of the observed transitions. From DSC curves taken with high heating rates (50 °C min^{-1}) of samples with high crystallinity we were able to extract correct melting enthalpy for phase-**I**, causing an endothermic transition not followed by an exothermic peak. The total enthalpy of phase-**II** wasn't measurable since it wasn't possible to achieve complete crystallinity from the molten state. Since the volume per molecule in both phases doesn't vary more than 0.5%, it is safe to assume that melting entropies will be very similar for both phases. $\Delta S_{m\text{-}I} = \Delta S_{m\text{-}II}$

Hence using Gibbs Equation:

$\Delta H_{m\text{-}I}/T_{m\text{-}I} = \Delta H_{m\text{-}II}/T_{m\text{-}II}$ and $\Delta H_{m\text{-}II} = \Delta H_{m\text{-}I} + x$ where $x = \Delta E_{II\text{-}I}$ → $\Delta H_{m\text{-}I}/T_{m\text{-}I} = (\Delta H_{m\text{-}I} + x)/T_{m\text{-}II}$

$\Delta H_{m\text{-}I} = 52.3\ kJ/mol = 12.44\ kcal/mol;\ T_{m\text{-}I} = 465\ K;\ T_{m\text{-}II} = 488\ K$

$x = (T_{m\text{-}II} \cdot \Delta H_{m\text{-}I}/T_{m\text{-}I}) - \Delta H_{m\text{-}I} = +0.62\ kcal/mol$

Note: From DFT solid state calculations sublimation energies were calculated but considering Hess's law and assuming that the energy required to go from the molten state to the gas phase is always the same,

the comparison between measured melting enthalpies and calculated sublimation energies is substantially correct.

Optical micrographs under thermal gradient were acquired with a Olympus BX41 microscope equipped with a Linkam FTIR600 temperature controlled hot stage.

Theoretical methods

Voids analysis calculations for phase-**I** and phase-**II** were performed with Mercury.[34] Standard parameter was taken for the probe radius (1.2 Å) and 0.2 Å for grid spacing was used. Voids fractions are 3.4% and 0.0% for phase-**I** and phase-**II** respectively.

Solid state density functional (DFT) calculations have been performed under periodical boundary conditions. In particular the Perdew-Wang (PWC) functional[21] coupled with a double zeta quality basis set including polarization functions on all atoms (i.e., DNP) was used as implemented in the DMol3 software.[34] The sublimation energy was calculated assuming fixed experimental atomic coordinates and cell parameters as:

$$\Delta E = \frac{nE(molecule) - E(bulk)}{n}$$

We estimated the contributions of the individual parts of compound **3** to the overall sublimation energy (ΔE) by selective removal of different moieties. For phase-**I** the overall calculated sublimation energy is about 40 kcal/mol. The same calculation performed removing only the bulky *t*-butyl groups from the two phenyl moieties shows a 25 kcal/mol decrease in the sublimation energy, highlighting the importance of these groups in forming alkyl CH···π interactions between adjacent molecules within the **3** crystal lattice. Furthermore, the sublimation energy value obtained including only the aromatic framework, i.e. the phenyl-quaterthiophene-phenyl backbone, accounts for about one third of the overall sublimation

energy (12 kcal/mol). To summarize, although a non-negligible interaction among aromatic moieties is envisaged, CH···π interactions appear to give the largest contribution to the overall crystal packing energy. In the phase-**II** crystal structure intermolecular forces still feature CH···π type interactions but they involve aromatic hydrogens, which are of different nature. Analysis of contributions to crystal packing energy of phase-**II** shows comparable energies for the bulky substituent and the aromatic moiety (20 kcal/mol and 16 kcal/mol respectively).

Calculations of excited states and TDMs have been carried out by using the semiempirical ZINDO method. The GAUSSIAN09 suite of programs[35] was used and for the sake of completeness also time-dependent DFT calculations (TDB3LYP/6–31G**) have been considered. For time-dependent calculations B3LYP was chosen because it provides the best compromise for an accurate description of excited states. Both isolated molecules and dimers were assumed at the experimental geometries. Only X-H bonds were relaxed. Excitation energies, oscillator strength and TDMs calculated for allowed single excitations by ZINDO method are in agreement with that obtained at TD-B3LYP/6–31G** level.

TDMs normalized components along $\mu//$, μT and $\mu 0$ (Figure 5.24) for lowest energy permitted optical transitions allow to establish TDMs direction with respect to the molecules backbone in both phases. From Table 5.7 it is clear that the TDMs lie in the aromatic plane, specifically along the direction connecting the two terminal carbons of the thienylene moieties for the molecule of phase-**I** and the two molecules of phase-**II**.

Table 5.7. Normalized components of TDMs along the direction shown in Figure.

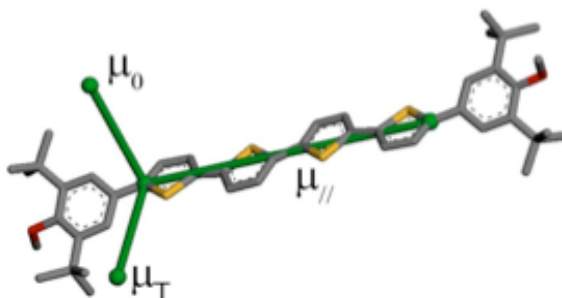|	$\mu//$	μT	$\mu 0$
Phase-**I** *trans*-molecule	-1.00244	-0.01643	0.029174
Phase-**II** *cis*-molecule	0.998732	-0.05141	0.004695
Phase-**II** *trans*-molecule	-0.99935	0.036831	-0.00322

Figure 5.24. Reference system used to estimate the direction of TDMs for allowed single excitations, here shown on the *trans*-molecule of phase-**I**.

References

[1] (a) Tang, C.W.; Van Slyke, S.A. *Appl. Phys. Lett.*, **1987**, *51*, 913. (b) Friend, R.H.; Gymer, R.W.; Holmes, A.B.; Burroughes, J.H.; Marks, R.N. *Nature*, **1999**, *397*, 121-123. (c) Lee, J.H.; Yuan, Y.Y.; Kang, Y.J.; Jia,, W.L.; Lu, Z.H.; Wang, S.N. *Adv. Funct. Mater.*, **2006**, *16*, 681-684. (d) Strassert, C.A.; Chien, C.; Lopez, M.D.G.; Kourkoulos, D.; Hertel, D.; Meerholz, K.; De Cola, L. *Angew. Chem. Int. Ed.*, **2011**, *50*, 946-949.

[2] (a) Zhang, C.; Zou, C.; Ya, Y.; Hao, R.; Sun, F.; Han, Z.; Zhao, Y.S.; Yao, J.N. *J. Am. Chem. Soc.*, **2011**, *133*, 7276-7279. (b) Gao, F.; Liao, Q.; Xu, Z.; Yue, Y.; Wang, Q.; Zhang, H.; Fu, H. *Angew, Chem, Int. Ed.*, **2010**, *49*, 732-735.

[3] (a) Zang, L.; Che, Y.; Moore, J.S. *Acc. Chem. Res.*, **2008**, *41*,1596-1598. (b) Che, Y.; Zang, L. *Chem. Commun.*, **2009**, 5106.

[4] (a) Tessler, N.; Medvedev, V.; Kazes, M.; Kan, S.; Banin, U. *Science*, **2002**, *295*, 1506-1510. (b) Kundu, K.; Knight, S.F.; Willett, N.; Lee, S.; Taylor, W.R.; Murthy, N. *Angew. Chem. Int. Ed.*, **2009**, *48*, 299-302.

[5] Chiang, C.L.; Tseng, S.M.; Chen, C.T.; Hsu, C.P.; Shu, C.F. *Adv. Funct. Mater.*, **2008**, *18*, 248-252. (b) Yan, D.P.; Lu, J.; Wei, M.; Qin, S.H.; Chen, L.; Zhang, S.T.; Evans, D.G.; Duan, X. *Adv. Funct. Mater.*, **2011**, *21*, 2497-2501.

[6] (a) Mutai, T.; Satou, H.; Araki, K. *Nat. Mater.*, **2005**, *4*, 685-687. (b) Sonoda, Y.; Goto, M.; Tsuzuki, S.; Tamaoki, N. *J. Phys. Chem. A*, **2007**, *111*, 13441-13445.

[7] (a) Beljonne, D.; Cornil, J.; Friend, R. H.; Jansen, R. A. J.; Bredas, J. L. *J. Am. Chem. Soc*, .**1996**, *118*, 6453. (b) Barbarella, G.; Favaretto, L.; Sotgiu, G.; Zambianchi, M.; Antolini,L.; Pudova, O.; Bongini, A. *J. Org. Chem.* **1998***, 63*, 5497.

[8] (a) Barbarella, G.; Favaretto, L.; Sotgiu, G.; Zambianchi, M.; Bongini, A.; Arbizzani, C.; Mastragostino, M.; Anni, M.; Gigli, G.; Cingolani, R. *J. Am. Chem. Soc.*, **2000**, *122*, 11971-11978. (b) Antolini, L.; Tedesco, E.; Barbarella, G.; Favaretto, L.; Sotgiu, G.; Zambianchi, M.; Casarini, D.; Gigli, G.; Cingolani, R. *J. Am. Chem. Soc.*, **2000**, *122*, 9006-9011.

[9] (a) Bernstein, J. *Polymorphism in Molecular Crystals*, Clarendon, Oxford, **2002**. (b) Matzger, A.J. *Cryst. Growth Des.*, **2008**, *8*, 2-7.

[10] (a) Sagara, Y.; Kato, T. *Nat. Chem.*, **2009**, *1*, 605. (b) Vargese, S.; Das, S. *J. Phys. Chem. Lett.*, **2011**, *2*, 863. (c) Yan, D.; Evans, D.G. *Mater. Horiz.*, **2014**, *1*, 46-57.

[11] (a) Zhang, H.; Zhang, Z.; Ye, K.; Zhang, J.; Wang, Y. *Adv. Mater.*, **2006**, *18*, 2369-2372. (b) Dou, C.; Han, L.; Zhao, S.; Zhang, H.; Wang, Y. *J. Phys. Chem. Lett.*, **2011**, *2*, 666. (c) Mauro, A.D.G.D.; Carotenuto, M.; Venditto, V.; Petraccone, V.; Scoponi, M.; Guerra, G. *Chem. Mater.*, **2007**, *19*, 6041-6044. (d) Sase, M.; Yamaguchi, S.; Sagara, Y.; Yoshikawa, I.; Mutai, T.; Araki, K. *J. Mater. Chem.*, **2011**, *21*, 8347-8351.

[12] Yan, D.P.; Lu, J.; Wei, M.; Ma, J.; Evans, D.G..; Duan, X. *Phys. Chem. Chem. Phys.*, **2012**, *14*, 9200-9204.

[13] Valeur, B. *Molecular Fluorescence: Principles and Applications*, Wiley-VCH Verlag GmbH, **2001**.

[14] Yoon, S.J.; Chung, J.W.; Gierschner, J.; Kim, K.S.; Choi, M.G.; Kim, D.; Park, S.Y. *J. Am. Chem. Soc.*, **2010**, *132*, 13675-13678.

[15] Tian, H.; Wang, J.; Shi, J.; Yan, D.; Wang, L.; Geng, Y.; Wang, F. *J. Mater. Chem.*, **2005**, *15*, 3026-3030.

[16] Fichou, D. *J. Mater. Chem.*, **2000**, *10*, 571-575.

[17] Barbarella, G.; Zambianchi, M.; Del Fresno I Marimon, M.; Antolini, L.; Bongini, A. *Adv. Mater.*, **1997**, *9*, 484-488.

[18] Mugurama, H.; Hotta, S. *J. Phys. Chem. B*, **2006**, *110*, 23075-23079.

191

[19] Dunitz, J. D.; Bernstein, J. *Acc. Chem. Res.*, **1995**, *28*, 193-196.

[20] (a) Nakatonani, H.; Adachi, C.; *Adv. Optical Mater.*, **2013**, *1*, 422-426. (b) Mizuno, H.; Haku, U.; Marutani, Y.; Ishizumi, A.; Yanagi, H.; Sasaki, F.; Hotta, S.; *Adv. Mater.*, **2012**, *24*, 5744-5748. (c) Yanagi, H.; Morikawa, T.; Hotta, S.; Yase, K.; *Adv. Mater.*, **2001**, *13*, 313-316.

[21] Perdew, J. P.; Wang, Y.; *Phys. Rev. B*, **1992**, *45*, 13244-13246.

[22] Main assumptions are: similar Stoke shifts for both phases, HOMO-LUMO transition allowed and no significant conformation rearrangement after photon absorption.

[23] Tedesco, E.; Della Sala, F.; Favaretto, L.; Barbarella, G.; Albesa-Jové, D.; Pisignano, D.; Gigli, G.; Cingolani, R.; Harris, K.D.M. *J. Am. Chem. Soc.*, **2003**, *125*, 12277-12281.

[24] Zhao, Z.; Spano, F. C.; *J. Phys. Chem. C*, **2007**, *111*, 6113-6118.

[25] Bando, K.; Nakamura, T.; Shimoi, Y.; Kobayashi, S.; Fujiwara, S.; Masumoto, Y.; Sasaki, F.; Hotta, S.; *Phys. Rev. B*, **2008**, *77*, 45205-45207.

[26] Bando, K.; Nakamura, T.; Kobayashi, S.; Masumoto, Y.; Sasaki, F.; Hotta, S.; *J. Appl. Phys*. **2006**, *99*, 13518-13521.

[27] Meinardi, F.; Blumstengel, S.; Cerminara, M.; Macchi, G.; Tubino, R.; *Phys. Rev. B*, **2005**, *72*, 35207-35210.

[28] (a) Mukamel, S.; Tretiak S.; *Chem. Rev.*, **2002**, *102*, 3171. (b) Ottonelli, M.; Musso, G.; Dellepiane, G.; *J. Phys. Chem. A*, **2008**, *112*, 3991. (c) Quarti, C.; Fazzi, D.; Tommasini, M.; *Chem. Phys. Lett.*, **2010**, *496*, 284-286.

[29] Canesi, E. V.; Dassa, G.; Botta, C.; Bianco, A.; Bertarelli, C.; Zerbi, G. *Open Chem. Phys. J.*, **2008**, *1*, 23-27.

[30] Kurata, H.; Takehara, Y.; Kim, S.; Sakai, K.; Matsumoto, K.; Kawase, T. and Oda, M. *Synlett.*, **2007**, *13*, 2053-2056.

[31] Bäuerle, P.; Würthner, F.; Götz, G. and Effenberger, F. *Synthesis*, **1993**, *11*, 1099-1103.

[32] Moreau, J.; Giovanella, U.; Bombenger, J-P.; Porzio, W.; Vohra, V.; Spadacini, L.; Di Silvestro, G.; Barba, L.; Arrighetti, G.; Destri, S.; Pasini, M.; Saba, M.; Quochi, F.; Mura, A.; Bongiovanni, G.; Fiorini, M.; Uslenghi, M.; Botta, C.; *Chem. Phys. Chem.*, **2009**, *10*, 647.

[33] Macrae, C. F.; Bruno, I. J.; Chisholm, J. A.; Edgington, P. R.; McCabe, P.; Pidcock, E.; Rodriguez-Monge, L.; Taylor, R.; van de Streek, J. and Wood, P. A. *J. Appl. Crystallogr.* **2008**, *41*, 466–470.

[34] Delley, B. ; *J. Chem. Phys*., **2000**, *113*, 7756-7759.

[35] Frisch *et al.* Gaussian 09, Revision A.1, Gaussian, Inc., Wallingford, CT, **2009**.

Postscript to this thesis

Conjugated organic materials appear as a promising alternative to the traditional inorganic semiconductors for a number of electronic and optoelectronic applications, such as field-effect transistors, solar cells, lasers, photodetectors and light emitting diodes, thanks to the peculiar optical and electrical properties strictly related to their chemical structure.[1] Organic devices can be ideally scaled down to molecular dimensions, moreover, they can be developed as low cost, flexible, large area systems. In this contest, the study of molecular design and the comprehension of structure-property relationships are essential for the development of more efficient devices and the structural versatility of the thiophene motifs provides tailor-made scaffolds for the synthesis of conjugated organic materials with tunable optic, electronic and redox features.

This thesis intends to demonstrate the effective strengthness of the "oligomer approach"[2] to face problems related to the employment of this important class of advanced materials in a few of the aforementioned applications. In addition to the direct use of conjugated oligomeric model compounds into solid-state devices, their study is also an essential prerequisite for understanding and developing photo and electroactive polymers.

The role of oligomers molecular configuration has emerged from the present study as a key factor in determining material's properties. Particularly Chapter 4 of this manuscript, while describing the use of a series of regioisomeric oligothiophenes as interlayers in hybrid nc-TiO$_2$/P3HT solar cells, details the effect of small variations in the molecular configuration of the oligomers on the final device performance. From Chapter 5 the issue emerges further, this time related

to a different series of thiophene based oligomers and to a different application, namely light emission. Moreover, from the same chapter a second relevant peculiarity of oligomeric compounds is highlighted, strictly dealing with their solid-state aggregation, that is the existence of different conformations for the same compound when in solid form (polymorphism), characterized in this case also by different optical properties.

Even if treating two separated subjects, with little mutual inherence, this thesis work underlines the general need for a stringent control over molecular configurations and solid state conformations of conjugated oligomeric materials, when dealing with their use in optoelectronic applications.

[1] (a) Cassoux, P. *Science*, **2001**, *291*, 263 (b) Bendikov, M.; Wudl, F.; Perepichka, D.F. *Chem. Rev.*, **2004**, *104*, 4891-4945.

[2] Mullen, K.; Wegner, G. *Electronic Materials: The Oligomer Approach*; Wiley: USA; 2008.

Aknowledgements

Brunella per l'aiuto con le misure GD-OES e il Dr. Santosh Kumar e Dr. Ing. Annamaria Petrozza (CNST-IIT@Polimi) per le misure di pump-probe. Per la realizzazione e caratterizzazione dei dispositivi ibridi descritti nei capitoli 3 e 4 ringrazio il Dr. Ing. Maddalena Binda e l'Ing. Simone Guarnera (CNST-IIT@POLIMI). Per l'aiuto nella preparazione dei derivati oligotiofenici riportati nel capitolo 4 ringrazio l'Ing. Mattia Dendena, che ha svolto il suo lavoro di tesi magistrale su questa tematica. Per la risoluzione delle strutture cristalline riportate ringrazio il Dr. Javier M. Rujas e il Dr. Emilio Parisini (CNST-IIT@Polimi) e il Prof. Stefano V. Meille (Dipartimento di Chimica Materiali e Ingegneria Chimica "G. Natta"). Per i calcoli teorici descritti riportati nella seconda parte dell'elaborato (capitolo 5) ringrazio il Prof. Antonino Famulari (Dipartimento "G. Natta"). Per le misure DSC riportate nel capitolo 3 ringrazio il Prof. Marta Rink e il Prof. Franceso Briatico (Dipartimento "G. Natta"), mentre per quelle riportate nel capitolo 5 ringrazio Tommaso Nicolini e ancora il Prof. Stefano V. Meille (Dipartimento "G. Natta"). Per il supporto nell'esecuzione delle misure di assorbimento, riflettanza e fotoluminescenza ringrazio il Dr. Luigi Brambilla (Dipartimento "G. Natta").

Ringrazio tutti gli studenti, dottorandi, post-doc e professori del gruppo di ricerca che ho avuto modo di conoscere in questi tre anni e con cui ho condiviso gli spazi del laboratorio e dell'ufficio, oltre che l'organizzazione delle attività di mantenimento generale degli spazi comuni: il Dr. Ing. Rossella Castagna, il Dr. Letizia Colella, il Dr. Ing. Giorgio Pariani, Lohit Karnam, l'Ing. Martino Quintavalla, l'Ing. Alessio Zanutta, l'Ing. Luigi Flaugnatti, l'Ing. Sara Ottoboni, Jeroen Van der Velden, il Prof. Andrea Bianco, il Prof. Matteo Tommasini e il Prof. Mirella Del Zoppo.

Ringrazio infine i miei genitori, Ivana e Angelo e mia nonna, Asia, per il continuo supporto e gli amici più cari, che ben sanno di esserlo.

Submitted paper

Structure-photoluminescence correlation for two crystalline polymorphs of a quaterthiophene with bulky substituents.

Journal:	*The Journal of Physical Chemistry Letters*
Manuscript ID:	Draft
Manuscript Type:	Letter
Date Submitted by the Author:	n/a
Complete List of Authors:	Nicolini, Tommaso; Politecnico Di Milano, Chimica, Materiali e Ingegneria Chimica "G. Natta" Famulari, Antonino; Politecnico di Milano, Chimica, Materiali e Ingegneria Chimica "G. Natta" Gatti, Teresa; Istituto Italiano di Tecnologia, Center for Nano Science and Technology@Polimi; Politecnico di Milano, Chimica, Materiali e Ingegneria Chimica Martí-Rujas, Javier; Istituto Italiano di Tecnologia, Center for Nano Science and Technology@Polimi Villafiorita-Monteleone, Francesca; Centro Nazionale di Ricerca (CNR), Istituto per lo Studio delle Macromolecole (ISMAC) Canesi, Eleonora; Istituto Italiano di Tecnologia, CNST@PoliMi Botta, Chiara; ISMAC-CNR, Parisini, Emilio; Istituto Italiano di Tecnologia, CNST@PoliMi Meille, Stefano; Politecnico di Milano, Chimica, Materiali e Ingegneria Chimica "G. Natta" Bertarelli, Chiara; Politecnico di Milano, Chemistry, Materials and Chemical Engineering

SCHOLARONE™
Manuscripts

199

Structure-photoluminescence correlation for two crystalline polymorphs of a quaterthiophene with bulky substituents.

Tommaso Nicolini[†], Antonino Famulari[†], Teresa Gatti[†,‡], Javier Martí-Rujas[‡], Francesca Villafiorita-Monteleone[θ], Eleonora V. Canesi[‡], Chiara Botta[θ], Emilio Parisini[‡], Stefano Valdo Meille*[·†], Chiara Bertarelli*[·†,‡]

[†]Dipartimento di Chimica, Materiali e Ingegneria Chimica, Politecnico di Milano, P.zza L. Da Vinci 32, 20133 Milano, Italy

[‡]Center for Nano Science and Technology@Polimi, Istituto Italiano di Tecnologia, Via Pascoli 70/3, 20133 Milano, Italy

[θ]Istituto per lo Studio delle Macromolecole (ISMAC), CNR, Via Bassini 15, 20133 Milano, Italy

Supporting Information Placeholder

ABSTRACT: Two crystal polymorphs of a bulky-group-substituted phenyl end-capped quaterthiophene are characterized by different molecular conformations and parallel *vs.* herringbone packing. Irrespective of their similar emissive spectra and common H-aggregate features, evidenced by crystal structure analysis and confirmed by solid-phase and excited-states first principles calculations, their luminescence is relatively high and, for one form, nearly double than for the other. Interaromatic packing energy contributions are established by quantum mechanical calculations and can be compared quantitatively, as the same species in different crystal environments is examined. They correlate inversely with the luminescence of the two phases, supporting the crucial role of the interaromatic packing for the luminescence properties of polyaromatic oligomers.

Amongst organic semiconducting materials, short conjugated oligomers have attracted a very broad interest due to their fine-tunable and normally well-defined structural features. Thiophene/phenylene co-oligomers are known for their remarkable optical properties and good charge mobility, which make them suitable candidates for electronics or optoelectronic applications.[1,2,3,4] Appropriate side groups on the conjugated backbone allow to modulate electronic properties and improve solubility paving the way to solution processing.[5] At the same time maintaining precise control over nanoscale molecular organization is crucial, as it can strongly affect physical properties. More specifically, the absorption and emission properties of aromatic compounds in the solid state are usually interpreted with reference to J- and H-aggregate models[6], the former showing generally higher photoluminescence. For crystalline oligothiophenes[7] and thiophene/phenylene co-oligomers[8,9,10,11] the absorption and emission properties present mainly H-features implying a nonemissive or weakly emissive 0–0 transition in the photoluminescence spectra[12], as reported for example for odd-numbered oligothiophenes.[13] H-aggregates are however enticing because of their stability and intrinsic structural anisotropy, giving easy access to important ASE and lasing effects. Efforts to obtain highly photoluminescent H-aggregates with oligothiophenes and other aromatic oligomers by the introduction of appropriate substituents[14] are hence ongoing.

Bulky substituents may be used to prevent strong aromatic interactions assumed to quench light emission. A notable case involves phenylene/vinylene oligomers[15] in which the introduction of methyls in the *meta* positions of terminal phenylenes preserves H-aggregation in crystals, albeit with loss of the herringbone motif, whereas light emission quantum yields are enhanced. In the mentioned instance, as in other cases where physical properties are modulated by chemical modifications of molecules, a quanti-

tative assessment of the role of packing and intermolecular interactions is prevented by the differences in molecular structure.

In this perspective, the ability of a given molecule to adopt different crystal structures offers a unique opportunity to modulate properties while preserving the possibility to carry out quantitative packing comparisons. Although often elusive, polymorphism in quaterthiophenes (4T) is not unusual: in some cases structural variations are minor, as for unsubstituted quaterthiophene, which may adopt two crystal forms with a very similar herringbone packing.[16] On the other hand in rarer instances, as for some α- and β-substituted 4T derivatives, conformational polymorphs have been found[17] and the formation of a particular phase is highly relevant to obtain reproducible optoelectronic responses.
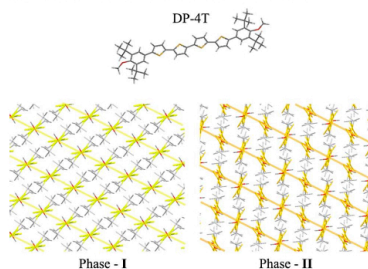
DP-4T

Figure 1. Crystal structures of phase-I and phase-II DP-4T shown along the direction of the 4T backbone. Thick yellow and orange lines evidence layers characterized by the most significant interaromatic intermolecular interactions.

Here we report the case of a 4T derivative (5,5'''-bis(3,5-di-*tert*-butyl-4-methoxyphenyl)-2,2':5',2'':5'',2'''-quaterthiophene (**DP-4T**)[18] showing two remarkably different, stable polymorphs that can be produced selectively (Figure 1). More specifically, phase-**I** is formed by standard solution crystallization techniques, whereas the second phase (phase-**II**) is obtained only by controlled thermal treatment. As the two polymorphs (see Table 1) show different photoluminescence (PL) properties, though with

Table 1. Structural and PL properties of DP-4T polymorphs.

	Density (Mg m^{-3})	E_{Subl} (kcal mol^{-1})[a]	Voids[b]	m.p. (°C)	PL-QY	PL max. (eV)
Phase-**I**	1.202	40.0	3.4%	195	18%	2.27
Phase-**II**	1.196	40.6	0.0%	217	11%	2.19

[a] Obtained from DFT solid state calculations (details are reported later in the text). [b] Voids calculated as percentage of the unit cell volume with a

200

1.2 Å probe radius and a 0.2 Å grid spacing on Mercury CSDS (Figure S2).

very similar spectral profiles, they represent an ideal case to correlate structural information and quantum mechanics (QM) calculations providing insight into their different emissive behavior.

From solution, **DP-4T** (phase-**I**) crystallizes in space group P-1 with half a molecule in the asymmetric unit and a single **DP-4T** molecule in the unit cell (see Table S1 and Figure 2). The quaterthiophene moiety is in an all-*trans* conformation and shows good planarity (r.m.s.d. = 0.08 Å) while the terminal phenyl rings form a 35° angle with respect to the mean thiophene plane. In phase-**I** crystals molecules arrange parallel in loose stacks (see Figures 1 and 2) deviating from the herringbone motif typically observed in most substituted and unsubstituted oligothiophenes. The steric requirements of *tert*-butyl substituents are plausibly a key factor leading to the phase-**I** molecular arrangement.
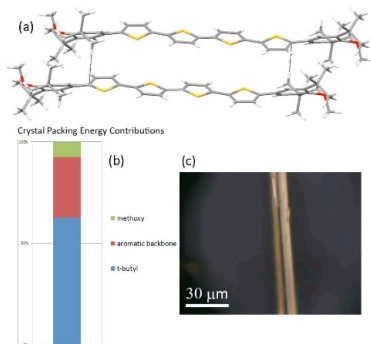

Figure 2. Crystal structure of phase-**I** (a) View of two DP-4T molecules showing short contacts stemming from alkyl C–H···π interactions (shown as black lines). (b) Crystal packing energy contributions of methoxy, aromatic backbone and *tert*-butyl moieties. (c) Needle-like crystal of phase-**I**

Attempts to grow single crystals of phase-**II** from solution, also adopting seeding methods, were unsuccessful,[19] always resulting in phase-**I** crystals. However phase-**II** crystals may be obtained quantitatively by appropriate thermal treatment of phase-**I**. Specifically, keeping single crystals of phase-**I** at 200 °C for 30 min results in the conversion into phase-**II** orange single crystals of sufficient size (> 50 μm) and quality for high resolution X-ray diffraction. Interestingly, the original needle shape of phase-**I** crystals (Figure 2c and 3c and S3 *in situ* optical micrographs) is retained also by polycrystalline phase-**II** material.

The space group of phase-**II** is also P-1 but the asymmetric unit is now defined by two independent half molecules (Table S1 and Figure 3a) and hence two different molecules are present in the unit cell. Since the midpoint of both molecules lies on crystallographic centres of inversion the central interthiophene bond is *trans* in both **DP-4T** molecules. In one case the tetrathiophene ring system is arranged in a *cis-trans-cis* planar conformation (out-of-plane r.m.s. = 0.06 Å) while the second molecule in phase-**II** maintains the all-*trans* conformation found in phase-**I**, however with a more pronounced distortion from planarity (r.m.s.d. = 0.19 Å). The phenyl rings in both phase-**II** conformers remain tilted at about 30° from the plane of the adjacent thiophenes. A further relevant feature of the phase-**II** structure is the

loss of the parallel stacking arrangement observed in phase-**I**, as the two independent molecules form a T-shaped dimer in which the *cis-trans-cis* conformer faces edge-on the all-*trans* molecule at an angle of 71°. The arrangement of the **DP-4T** molecules in phase-**II** is thus a herringbone-like packing (Figure 3a) and not the parallel stacking found in phase-**I**. As a consequence the slightly denser (+0.5%) phase-**I** allows for relatively large voids where the loose packing between tetrathiophene units occurs (Figure S2). There are no such voids in phase-**II**, which presents a lower density while its melting point is much higher (Table 1).
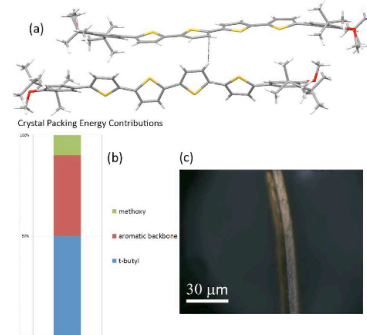

Figure 3. Crystal structure of phase-**II**. (a) View of two DP-4T molecules showing short contacts stemming from aromatic C–H···π interactions (shown as black lines). (b) Crystal packing energy contributions of methoxy, aromatic backbone and *tert*-butyl moieties. (c) Crystal of phase-**I** after transformation to phase-**II** polycrystalline aggregate.

In order to make sense of the apparently conflicting structural, thermal and emissive properties of the two polymorphs the packing of **DP-4T** molecules in both polymorphs has been analyzed by solid state–density functional (DFT) methods under periodical boundary conditions. In particular the Perdew-Wang (PWC) functional[20] coupled with a double zeta quality basis set including polarization functions on all atoms (i.e., DNP) was used as implemented in the DMol[3] software.[21] The same level of calculation employed here proved to be adequate for large supramolecular systems,[22,23,24,25] charged particle-containing systems[26,27,28,29] and crystalline phases of thiophene-based oligomers and polymers.[30] More specifically, in the latter case it was shown that calculated heats of sublimation are in good agreement with the experimental values. The analysis performed on the phase-**I** crystal structure yielded a sublimation energy of 40.0 kcal/mol. The relative contributions to the crystal packing energy (see Supporting Information for details) are depicted as a histogram (Figure 2b). A 63% contribution is due to the *tert*-butyl moieties that form C–H···π interactions between neighboring molecules along the stacking direction. DFT calculations suggest a slightly higher sublimation energy ($\Delta E_{II-I} \approx +0.6$ kcal/mol) for the higher melting polymorph phase-**II** consistent with calorimetric data (See Supporting Information). *Tert*-butyl groups still majorly contribute to crystal packing but do not appear to be involved in any type of specific stabilizing interactions: this might explain the large thermal parameters found for the atoms of these substituents, likely characterized by substantial conformational freedom within the crystal lattice. The packing energy of phase-**II** involves comparable contributions of the aromatic backbone and *tert*-butyl groups: 50% and 40% re-

201

spectively. This is consistent with the loss of alkyl C–H···π interactions and the development of aromatic C–H···π interactions between β-hydrogens of thienylene moieties in phase-**II**.

Photoluminescence (PL) spectra of single crystals of **DP-4T** polymorphs show interestingly a 0.077 eV bathochromic shift for the PL band as we move from phase-**I** to phase-**II**. A similar shift is observed for the onset of the excitation profiles (Figure S5). At the same time, quantum efficiency decreases from 18% for phase-**I** to 11% for phase-**II**, while amorphous films show a 4% PL value, confirming the high relevance of the crystalline packing.
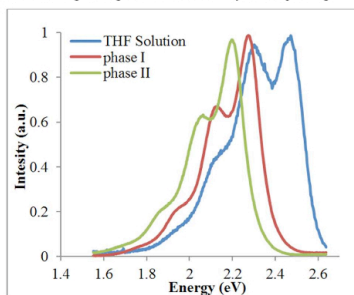

Figure 4. Photoluminescence spectra (λ_{exc}= 420 nm) of **DP-4T** in phase-**I**, phase-**II** crystals and in THF solution. Excitation profiles in Figure S5.

The effect of molecular conformations and dimeric intermolecular interactions on the optical properties of two polymorphs can be at least partly understood with reference to HOMO-LUMO energy levels. These were calculated for both phases within the DFT framework used for solid state energy calculations, considering both isolated molecules and neighboring pairs, to grossly take into account the impact of crystalline packing on electronic orbitals. For phase-**I**, no significant variation is apparent comparing the isolated molecule to a stacked pair, consistent with the equivalence of all molecules in this crystal form. On the other hand, for the isolated all-*trans* and *cis-trans-cis* conformers in phase-**II**, HOMO-LUMO gaps are higher than for molecules in phase-**I**, in disagreement with the bathochromic shift in the PL spectrum. This observation suggests a larger influence of intermolecular interactions in phase-**II**. In fact, a smaller gap results when looking at the dimer frontier orbitals in this phase. Interestingly, the DFT method used agrees quite nicely with the experimental PL red shift (0.077 eV) obtained comparing the gaps for phase-**I** and phase-**II** dimers ($|\Delta(Gap_{II}.Gap_I)|$= 0.087 eV). We stress that this consideration is qualitative at best, since various unproven assumptions are needed for such a simple correlation to hold.[31] Another peculiar feature evidenced by calculations on the phase-**II** dimer is that the HOMO can be visualized as residing on the all-*trans* molecule while the LUMO is on the *cis-trans-cis* conformer (see Figure 5). This result suggests a dimer excited state with partial charge transfer character that could account for both the PL bathochromic shift and QY reduction.[32]

To get a more detailed picture of allowed electronic transitions of DP-4T in both phases single excitations and the corresponding transition dipole moments (TDMs) need to be evaluated. TDMs for oligothiophenes stacked in a parallel fashion are expected to lie along the aromatic backbone implying H-like behavior. Indeed 1-D clusters of molecules along the closest interaromatic intermolecular interaction direction (see Figures 1 and 6), show apparent-

ly H-like mutual arrangements of the molecular long axes for both DP-4T phases. Only slight deviations are found for phase-**II** which shows some misorientation due to the presence of two independent molecules in the unit cell. In this perspective the nearly double QY found for phase-**I** needs some discussion, since unequivocally H-aggregates, characterized by strong π-π interactions, are known to quench light emission.
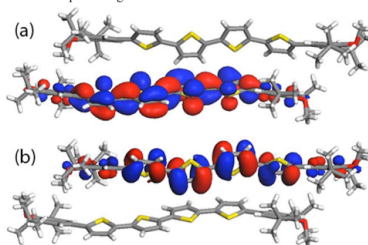

Figure 5. LUMO (a) and HOMO (b) orbitals for phase-**II DP-4T** dimer.

To confirm the previous qualitative considerations, calculations of excited states and TDMs have been carried out by using the semiempirical ZINDO method, which provides accurate results for the excited states of conjugated molecules.[33,34,35] The GAUSSIAN09 suite of programs[36] was used and for the sake of completeness also time-dependent DFT calculations (TD-B3LYP/6–31G**) have been considered (see details in Supporting Information). TDMs' vectors, associated with lowest energy excitations involving the HOMO and LUMO orbitals previously discussed, lie (see Table S2) within the thiophene plane for all molecules, with small deviations from the tetrathiophene main axis for all molecules of both polymorphs. The effect of packing on the couplings amongst TDMs' vectors in phase-**I** is quite simple, due to the presence of only one molecule per unit cell, i.e. all molecules, hence all TDMs, are stacked along the *a*-axis in a parallel fashion.
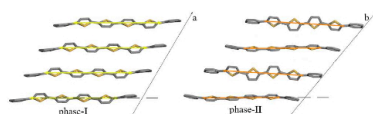

Figure 6. 1D clusters of closest neighboring molecules of phase-**I** (along the *a*-axis) and phase-**II** (along the *b*-axis), with superimposed yellow and orange arrows representing calculated transition dipole moments, arranged in parallel stacks, a feature of ideal H-aggregate model.

For phase-**II** the situation is more complex, but since the misalignment between independent molecules and between TDMs and each molecule does not exceed 6° altogether, TDMs' vectors can be considered parallel within a sensible approximation. Indeed molecular stacks and therefore TDMs' vectors can both be regarded as H-aggregates and somehow surprisingly it is the one closer to the ideal H-model (the angle between the aromatic plane and the stacking axis is closer to 90° for phase-**I**) that shows the highest QY. Therefore the drop in PL and the red shift in phase-**II DP-4T** must be explained by other properties among which intermolecular interactions within the two crystal structures are likely to be crucial.

1
2
3
4
5
6
7
8
9
10
11
12
13
14
15
16
17
18
19
20
21
22
23
24
25
26
27
28
29
30
31
32
33
34
35
36
37
38
39
40
41
42
43
44
45
46
47
48
49
50
51
52
53
54
55
56
57
58
59
60

[36] Frisch *et al.* Gaussian 09, Revision A.1, Gaussian, Inc., Wallingford, CT, **2009**.
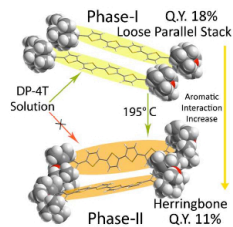
Reviewer(s)' Comments to Author:

Reviewer: 1

Recommendation: This paper is probably publishable, but major revision is needed.

Comments:

The authors present a combined structural, spectroscopic and computational study on two polymorphs of a substituted diphenyl-quaterthiophene. Such an investigation is indeed of crucial importance to disentangle intermolecular interactions from other

203

factors like substituent effects. However, the investigations presented hereafter do not give a satisfying answer to this. This is partly due to some misconceptions, but also due to missing photophysical data and proper quantum-chemical description as detailed below. A thorough revision has to be done before possible publication in JPCL.

(1) Crucial for the interpretation of solid state properties of conjugated organic molecules is a proper understanding of H-aggregates in the framework of Kasha's molecular exciton model: [A]

(i) H-aggregates are not necessarily characterized by strong pi-pi interactions as suggested by the authors (p. 2), but in general by a 'side-by-side' arrangement of the transition dipole moments (TDM) constituting the excitonic interaction. This holds not only in the original formulation with point dipoles by Kasha, [A] but also in the quantum-chemical (QC) corrected form as reviewed e.g. in Ref. [B]. Accordingly, H-aggregates can be realized both by a herringbone arrangement (where pi-pi interactions are rather weak to moderate) and by pi-stacks with strong pi-pi interactions. Such comparison was done earlier through electron-hole wavefunction plots. [C]

(ii) Importantly, Kasha's model tells something about the oscillator strength / TDM of the states resulting from the excitonic interaction, which directly relates to the rate constant of PL (kr), but not about the photoluminescence quantum yield (PL QY). This is because the latter not only depends on kr, but also on competing non-radiative rates (knr), which are not subject of the Kasha model.[B] Therefore, H-aggregates can be highly emissive in single crystals, where knr are small, as demonstrated in Ref. [D]. Thus, the statement of the authors on p. 2, that J-aggregates show generally higher PL than H-aggregates, is not necessarily correct as can be also seen from the extensive comparative studies in Ref. [B]. This however also means that structure-property relationships in the frame of the Kasha model cannot be established with the PL QYs, but only with kr. Thus, besides the PL QY presented in the paper, the authors have to record the PL lifetimes to extract kr.

(2) For the PL data, the authors should remark in the paper that single crystals (depending on the size) suffer from substantial reabsorption. This can be seen in the PL spectra of Fig. 4, but it will certainly also affect the measured PL QYs (also in an integrating sphere) as well as measured lifetimes. Thus, the PL QYs for the both phases are only comparable if the crystals are of comparable size.

The authors should comment on this.

(3) The authors should note that the spectral shifts of the PL spectra are not only due to excitonic interactions, but also to (anisotropic) polarizability effects, as e.g. detailed in Ref. [E]. QC calculations catch only the excitonic part but do not cope with the polarizability. Although the difference in polarizability for the two polymorphs is expected to be small, it could partly account for the observed differences between experiment and QC results. This should be taken into account in the discussion.

(4) There are several concerns about the QC calculations: (i) The comparison of the experimental band positions with simple HOMO-LUMO gaps does not comply with the state of the art. As the authors themselves remark later correctly this one-electron approach is oversimplified. In fact, it might even give a wrong qualitative trend. Thus, the comparison should be rather done with calculations of the S0->S1 energies as actually performed by the authors at the ZINDO and TD-DFT level but not discussed; detailed results of these calculations should be given in the ESI. (ii) The authors did only a partial geometry optimization, relying on the experimental C-C bond length and angles. This is very problematic, especially since the error of x-ray data is insufficient for the accuracy required by DFT calculations. The calculations thus have to be repeated, e.g. by just fixing the torsional angles, but allowing for a full geometrical relaxation of all other intramolecular parameters. Time-dependent calculations based on these geometries should allow for a more reliable comparison. Single point dimer calculations should then be done by replacing the molecules in the x-ray structure by these optimized ones. (iii) The authors should state if the dimer calculations were done in a supramolecular approach or transition dipole densities were used;[F] the latter avoids local polarizations, which again allows for a more accurate comparison if the intermolecular arrangement differs significantly as in the present case (i.e. herringbone vs. pi-stack). (iv) The calculations for the solid state are based on dimer calculations. This indeed allows extracting some trends; however, consideration of non-nearest neighbor interactions might change even the qualitative picture significantly, as detailed in Ref. [G]. This should be especially true in the present case, since Type I is a shifted pi-stack arrangement, whereas Type II is a herringbone arrangement. This has to be shortly discussed, since it might provide further arguments for the observed deviations from experiment.

It would also be helpful for the reader if more structural information for the dimer arrangement is presented in the paper, such as herringbone angles,[B] as well as

205

displacements along the long & short axes, resulting in so-called pitch & roll angles.[H]
Minor points:

p. 2: HOMO-LUMO gaps are rather "larger" than "higher"

p. 2: it should rather read "translationally non-equivalent molecules in the unit cell" than "two independent molecules in the unit cell"

p. 2: what means "sensible approximation" ? - did the author's wanted to say "simple" ?

[A] M. Kasha, H. R. Rawls, M. Ashraf El-Bayoumi, Pure Appl. Chem. 11 (1965) 371.

[B] J. Gierschner, S. Y. Park, J. Mater. Chem. C. 1 (2013) 5818.

[C] J. Gierschner, M. Ehni, H.-J. Egelhaaf, B. Milián Medina, D. Beljonne, H. Benmansour, G. C. Bazan, J. Chem. Phys. 123 (2005) 144914.

[D] J. Gierschner, L. Lüer, B. Milián-Medina, D. Oelkrug, H.-J. Egelhaaf, J. Phys. Chem. Lett. 4 (2013) 2686.

[E] Y.-S. Huang, J. Gierschner, J. P. Schmidtke, R. H. Friend, D. Beljonne, Phys. Rev. B. 84 (2011) 205311.

[F] B. P. Krueger, G. D. Scholes, G. R. Fleming, J. Phys. Chem. B 102 (1998) 5378.

[G] J. Gierschner, Y.-S. Huang, B. Van Averbeke, J. Cornil, R. H. Friend, D. Beljonne, J. Chem. Phys 130 (2009) 044105.

[H] M. D. Curtis, J. Cao, J. W. Kampf, J. Am. Chem. Soc. 126 (2004) 4318.

Additional Questions:

Urgency: High

Significance: High

Novelty: High

Scholarly Presentation: Moderate

Is the paper likely to interest a substantial number of physical chemists, not just specialists working in the authors' area of research?: Yes

Reviewer: 2

Recommendation: This paper is publishable subject to minor revisions noted. Further review is not needed.

Comments:

My only objection to this interesting paper is that the compound in question is not "a quaterthiophene with bulky substituents" but a thiophene/phenyl hexamer (a co-oligomer) with bulky substituents at the terminal positions.

In consequence, the title should be modified as well as some sentences in the text concerning "..substituted quaterthiophene…".

Additional Questions:

Urgency: High

Significance: High

Novelty: High

Scholarly Presentation: High

Is the paper likely to interest a substantial number of physical chemists, not just specialists working in the authors' area of research?: Yes

The manuscript is currently under revision ad will be resubmitted to the same Journal with the modifications indicated by reviewers.